Preparation of Supported Metal Catalysts by Atomic and Molecular Layer Deposition for Improved Catalytic Performance

by

Troy D. Gould

B.S., North Carolina State University, 2007

A thesis submitted to the

Faculty of the Graduate School of the

University of Colorado in partial fulfillment

of the requirement for the degree of

Doctor of Philosophy

Department of Chemical and Biological Engineering

2014

This thesis entitled:

Preparation of Supported Metal Catalysts by Atomic and Molecular Layer Deposition for Improved Catalytic Performance

written by Troy D. Gould

has been approved for the Department of Chemical and Biological Engineering

_____

J. Will Medlin, Ph.D.

_____

John L. Falconer, Ph.D.

Date_____

The final copy of this thesis has been examined by the signatories, and we find that both the content and the form meet acceptable presentation standards of scholarly work in the above mentioned discipline.

Abstract

Gould, Troy, D. (Ph.D. Chemical and Biological Engineering)

Preparation of Supported Metal Catalysts by Atomic and Molecular Layer Deposition for Improved Catalytic Performance

Thesis directed by professors John L. Falconer, J. Will Medlin, and Alan W. Weimer

Creating catalysts with enhanced selectivity and activity requires precise control over particle shape, composition, and size. Here we report the use of atomic layer deposition (ALD) to synthesize supported Ni, Pt, and Ni-Pt catalysts in the size regime (< 3 nm) where nanoscale properties can have a dramatic effect on reaction activity and selectivity.

This thesis presents the first ALD synthesis of non-noble metal nanoparticles by depositing Ni on Al_2O_3 with two half-reactions of $Ni(Cp)_2$ and H_2. By changing the number of ALD cycles, Ni weight loadings were varied from 4.7 wt% to 16.7 wt% and the average particle sizes ranged from 2.5 to 3.3 nm, which increased the selectivity for C_3H_6 hydrogenolysis by an order of magnitude over a much larger Ni/Al_2O_3 catalyst. Pt particles were deposited by varying the number of ALD cycles and the reaction chemistry (H_2 or O_2) to control the particle size from approximately 1 to 2 nm, which allowed lower-coordinated surface atoms to populate the particle surface. These Pt ALD catalysts demonstrated some of the highest oxidative dehydrogenation of propane selectivities (37%) of a Pt catalyst synthesized by a scalable technique.

Dry reforming of methane (DRM) is a reaction of interest due to the recent increased recovery of natural gas, but this reaction is hindered from industrial implementation because the Ni catalysts are plagued by deactivation from sintering and coking. This work utilized Ni ALD and NiPt ALD catalysts for the DRM reaction. These catalysts did not form destructive carbon whiskers and had enhanced reaction rates due to increased bimetallic interaction. To further

limit sintering, the Ni and NiPt ALD catalysts were coated with a porous alumina matrix by molecular layer deposition (MLD). The catalysts were evaluated for DRM at 973 K, and the MLD-coated Ni catalysts outperformed the uncoated Ni catalysts in either activity (with 5 MLD cycles) or stability (with 10 MLD cycles).

In summary, this thesis developed a new Ni nanoparticle ALD chemistry, explored possibilities for changing Pt ALD particle size, brought the two techniques together to create enhanced bimetallic catalysts, and stabilized the catalysts using MLD.

This thesis is dedicated to my wife Sarah for all of her love and support, and for joining me on the journey and adventure of graduate school in Boulder.

Acknowledgements

When I tell people I am tri-advised, they usually look at me like I'm crazy – but I think my graduate studies have been an interesting journey and an overall great experience, thanks to each one of my advisors and research groups. I'm thankful for having Will Medlin's guidance throughout my degree. Not only did Will give me space to be independent and learn from my own mistakes, but he also made sure that I was always headed in the right direction. I looked to Will not only for guidance scientifically, but Will served as a role model for how to be successful while maintaining a work-life balance. I'm thankful for John Falconer's rigorous and critical review of my research and writing. Thanks to John, I feel that I am a much better scientist than I was five years ago, or even a year ago. I'm also grateful for Alan Weimer's support and encouragement over the years, and his emphasis on teamwork, hence our research's group name: Team Weimer. Al always impressed me with how much passion he had for his research, his desire to make a difference, and his ability to make significant contributions to his areas of focus.

Another benefit of being tri-advised is being in three research groups. I am so grateful for the opportunities to learn from everyone, because whenever I had questions or problems there were always so many talented and helpful people to ask. Special thanks go out to Dave King and Jinhua(Helen) Li who were post-docs when I first started working in the Weimer lab; they really helped me get started on doing (and understanding) ALD. I also truly believe that I could not have done the work in this thesis without Hans Funke. Hans not only knows something about everything, but he is an adept problem solver, and would always find the time and a way to help me in building and fixing the equipment I used for most of my work.

The work presented in this thesis was made possible by contributions from a number of people. Most significant was the help from Alia Lubers and Matt Montemore. Alia aided in

understanding how to make the Ni ALD work many years ago, and Ni ALD was a very messy and difficult chemistry to master. Matt Montemore provided insight through his DFT calculations as to why the bimetallic catalysts I synthesized were performing so well. Alan Izar was also extremely helpful in teaching me how to do MLD coatings in his reactor. One of my undergraduate students, Jacob Carrier, also played a crucial role in logging many hours running reactions and temperature-programmed studies. The rest of the members of my research groups were also extremely helpful, and I am grateful for all of the discussions about our research and exposing me to many different research projects. Not only were my research members great scientists and colleagues, but they were also great friends.

I would also like to thank the staff in the Chemical and Biological Engineering department. Dragan Mejic made components for me during my first couple years that I used daily throughout my degree, and because of his excellent skill and design suggestions, the reactor system is still going strong and will continue to do so for many years. He also taught me many things, was always open for me to stop by and ask him questions, and helped me correct bad habbits (like stripping threads). Dana Hauschulz and Maria Toscano-Leary were extremely helpful with any electronic issues I had, and would drop whatever they were doing to help me. I have to thank Andrew Schmidt especially, because dealing with financial issues for a student who's funding is split three ways was complicated, but somehow he kept it all together, never complained, and was always helpful. Lastly I would like to thank Dominique de Vangel for being extremely helpful in guiding me through all of the rules, regulations, and timelines for our department, and doing so with a smile. I was also involved in recruiting as a graduate student representative, and working with Dom was not only a pleasure, but was also encouraging to learn how much he truly cares about us students.

These acknowledgements would be extremely lacking without the mention of the support from my family over the years. Their support helped get me through the tough times when equipment was broken or kept breaking. I am especially thankful for having my wife Sarah by my side throughout my graduate career because she was always supportive, helpful when I needed her (or when she knew I needed help), and was someone I could always run ideas past because she understood them. As a fellow PhD student from our department, she knew how large the workload was, and was patient with me during my long hours in lab.

I'd also like to thank my former professor and undergraduate research advisor, Dr. Juan Hinestroza (now at Cornell University). He introduced me to the concept of nanotechnology during my first semester at NCSU, and granted me the incredible opportunity to begin research during my freshman year. It was under his guidance, and through his belief in me that I developed my interest in nanotechnology, which is perhaps why this thesis has focused on the interface of nanotechnology and catalysis.

Lastly, this work would not have been possible without several funding sources. For three of my years, I was funded through the National Science Foundation Graduate Research Fellowship Program. I also received assistance for travel through the Department of Education's Graduate Assistantships in Areas of National Need (GAANN).

Table of Contents

List of Figures

List of Tables

List of Schemes

Chapter 1: Introduction

1.1 Overview

The goal of this thesis is to explore and understand enhanced nanoscale effects in catalysis by creating supported Ni, Pt, and NiPt catalysts with particle sizes below 3 nm using atomic layer deposition (ALD) as the synthesis technique. Specifically, the objectives of this thesis are to:

1) Develop and explore the catalytic advantages of synthesizing Ni nanoparticles by ALD for the hydrogenolysis of alkenes.
2) Explore the effect of varying Pt nanoparticle size on surface structure and selectivity for the oxidative dehydrogenation of propane.
3) Synthesize bimetallic Ni-Pt catalysts by ALD to improve dry reforming of methane activity and coking resistance.
4) Stabilize nanoparticles synthesized by ALD using porous coatings prepared with molecular layer deposition (MLD) to maximize the benefits of maintaining small particle size in harsh reforming conditions.

This introduction provides a broad background and motivation for studying the nanoscale catalytic enhancements found in this thesis. An overview of nanostructure effects on catalysis is provided, in addition to specific information about the correlation between particle size and catalytic activity for two of the reactions studied in this thesis. This introduction also provides information about the synthesis methodology used to create these nanoparticles (ALD) and modify the particles with stabilizing layers. Finally, detailed explanations of the specific objectives for this thesis are given.

1.2 Introduction to Heterogeneous Catalysis

A major milestone in the field of heterogeneous catalysis was the discovery of the Haber-Bosch process in 1905.[1, 2] This process converts N_2 and H_2 gas to ammonia at an industrial scale, allowing for production of fertilizer that contributed substantially to population growth, and is estimated to provide fertilizer that sustains approximately 1/3 of the population today.[1] Since that time, heterogeneous catalysis has spurred the development of several crucial industries, and is utilized in approximately 90% of the total production in the chemical industry.[2, 3] Discoveries of synthetic zeolite materials and the fluid catalytic cracking (FCC) process led to substantial development of the petrochemical industry for fuels and plastics production.[4] During the 20^{th} century, most advances in catalysis came through guess-and-check high throughput catalyst screening.[3, 5] While high-throughput screening identified many useful catalysts, the discovery of better catalysts has recently been driven by fundamental understanding of how catalysts work and how to design specific catalysts for specific reactions.

Advances in computational power have allowed for significant development of catalyst modeling for surfaces, and more recently, nanoparticles.[6-9] More sophisticated synthesis techniques have been developed to allow for spatial control over catalyst morphology and composition. Additionally, advanced experimental techniques have been developed to study catalysts at varying levels: fundamental studies in ultra-high vacuum (UHV) on single crystals,[10] advanced spectroscopic techniques for structure and composition of the catalysts,[11-14] *in-situ* monitoring of catalyst syntheses,[15, 16] and *in-operando* monitoring of catalytic materials during realistic reaction conditions.[6, 17] The collective knowledge gained from modeling and experimentation provide insight into fundamental broad-reaching principles in catalysis, such as the d-band theory for relating electronic structure to metal-adsorbate

interactions.[18, 19] More recently, researches have attempted to develop models, or investigate key parameters (such as CO and O binding energies) that will have predictive power for identifying the best catalyst for a given reaction.[20, 21] The prediction of ideal catalysts based on fundamental principles is called rational catalyst design, and is the future of metal catalyst discovery in terms of advancing catalyst activity and selectivity, in addition to designing catalysts for reactions that are currently extremely difficult to perform. [22-24]

Heterogeneous catalysis has grown to encompass a wide range of materials such as zeolites, metal oxides, transition metals, metal salts, organic materials, or a combination of any of these materials.[3] The most widely used form of heterogeneous catalysts are transition metals supported on metal oxides, which began significant development with the discovery of the Fischer-Tropsch (F-T) process in 1913.[2] A large proportion of supported metal catalysts used in fuel and chemical production are supported on Al_2O_3, SiO_2, ZrO_2, or carbon, and these supports often affect the catalytic behavior of the metals or the catalytic properties of a bi-functional metal/metal oxide catalyst.[3] The work in this thesis used Al_2O_3 supports only, and focused on Ni and Pt transition metal catalysts. These two metals catalyze many reactions industrially, but exist at the opposite ends of the price spectrum, with current December 2013 market prices of Ni around $0.43 per troy-ounce and Pt priced around $1400 U.S. dollars per troy-ounce.[25] Although Pt is the superior catalyst for many reactions, economic incentives to offset the catalyst cost motivate the need for greater selectivity (to reduce costs of purification and separation), or greater activity and stability (to reduce the amount of Pt required). Many catalysts, especially those with the highest cost, are supported as nanoparticles with diameters less than 10 nm. These small sizes increase the surface to volume ratio of the catalysts, thereby maximizing the amount of active surface area exposed to reaction conditions and wasting less of

these precious metals on the interior. Catalysts also have other advantages when their particles are smaller than 5 nm.[6, 26, 27] When catalyst nanoparticles become sufficiently small, the fraction of atoms on (111) terraces diminishes, and other lower-coordinated atoms start to become the dominant type of surface atom.[28, 29] Changing the coordination and type of catalytic site can have dramatic effects on catalytic activity and selectivity. Depending on the type of reaction, decreasing the particle size can shut down a reaction completely, have no change in catalytic behavior with particle size, or enhance catalytic properties.[26, 27, 30]

1.3 Advantages of nanostructure control in transition metal heterogeneous catalysis

Heterogeneous catalysis was once considered a "black art" due to uncertainties of how catalysts worked at the fundamental level. However, with the advance of more fundamental techniques such as ultra-high vacuum (UHV) single crystal studies or density functional theory (DFT) computations, a more rational approach to understanding and designing catalysts tailored to specific reactions has been widely successful.[8, 10, 17, 19, 31, 32] The catalysis field has been advancing towards precise control of nanometer and sub-nanometer features in catalytic materials. These advances were made possible by new synthesis methods, better analytical techniques to probe ultra-small features, and by the greater understanding of fundamental catalytic principles at the nanoscale through theoretical investigations.[6, 17, 33]

Metal nanoparticles can exhibit catalytic properties that differ greatly from bulk materials due to geometric and electronic effects that arise when the particles become smaller than 10 nm.[26, 30] Additionally, a clear advantage in catalyst activity and utilization is achieved with nanoparticles because as the size decreases, the fraction of surface atoms increases. More interestingly, selectivity and/or activity increase for some reactions when the particle diameters drop below 10 nm, or even further as the diameters approach 2 nm.[26, 27]

When catalyst behavior changes with particle diameter, the reaction is known as structure sensitive. The different types of structure sensitivity are outlined in Figure 1, where a reaction's turnover frequency (TOF), defined as moles reacted per site per time, can increase, decrease, or pass through a maximum with decreasing particle size. The differences in catalytic behavior are due to the type of site on which the reaction occurs. Different catalytic sites (such as step edges, corners, etc.) change in population as particle size decreases. For example, if a catalytic reaction requires terrace sites to proceed (such as selective hydrogenation of cinnamaldehyde to cinnamyl alcohol)[34, 35], as the catalyst particle size becomes smaller, the number of terrace sites diminishes and disappears and so would the catalytic activity. The change in surface concentration of different coordination numbers with particle size are shown for a cubo-octahedron particle geometry in Figure 1.2. Additionally, ensemble size effects play a role as catalyst size decreases. Ensemble size effects means that certain reactions require a specific number of sites to bind all of the necessary molecules in the proper configurations for the reaction to proceed. For example, if the reactant needs 5 atoms on a terrace to stabilize a transition state, when the catalyst particles become too small, the ensemble of atoms required for this reaction disappears.

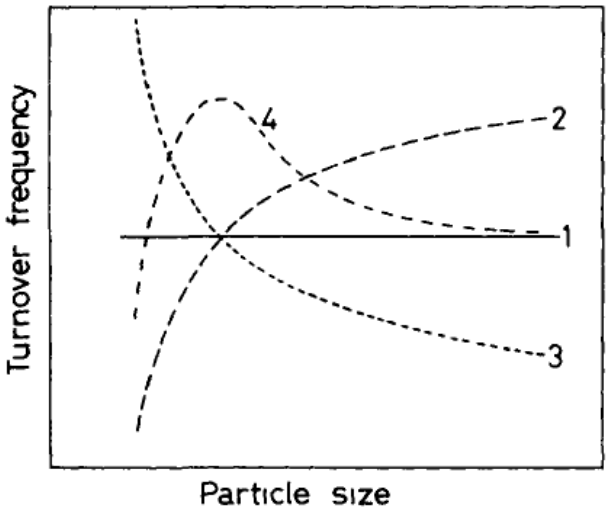

Figure 1.1. The four structure sensitivities for catalytic reactions as a function of particle size. [30]

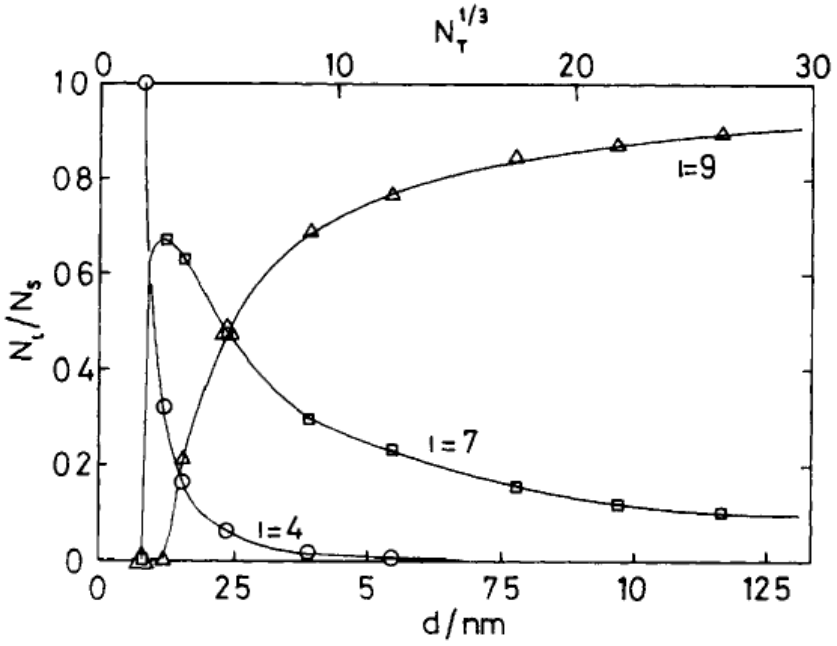

Figure 1.2. Fraction of atoms on the surface with a given atom coordination number, I, at different particle sizes, d, (or total number of atoms (NT)1/3) for the ideal uniform cubo-octahedron particle shape.[30] [28]

Changes in coordination number have such large effects on TOF because of electronic structure effects, geometric effects, and the interaction of these factors with the type of bond being reacted. Activation of a σ-bond, such as with CH_4 activation, can occur on a single atom. As the coordination number of an atom decreases, the localization of the valence electrons on the atom's surface increases (shifting the d-band center upwards), and the degree of orbital overlap with that of the reactant also increases. These two factors aid in dissociating the σ-bond even though the transition state structure does not change. Other reactions such as hydrogenolysis require molecules to interact with multiple sites (such as those found on step edges) to stabilize transition states and cleave bonds by activating the π-bond.

1.4 Dry reforming of methane on Ni-based catalysts

The recent enhancements in natural gas recovery have drawn much attention to methane steam reforming (MSR) and dry reforming of methane (DRM) with CO_2 to produce H_2 or syngas for fuel production. These reforming reactions and their heat of reaction (ΔH_{298}) are listed below:

Methane steam reforming:

$$CH_4 + H_2O \rightarrow CO + 3H_2 \qquad \Delta H_{298} = 206 \text{ kJ/mol}$$

Dry reforming of methane:

$$CO_2 + CH_4 \rightarrow 2CO + 2H_2 \qquad \Delta H_{298} = 247 \text{ kJ/mol}$$

Both reactions are highly endothermic, and are typically run industrially from 773 K up to 1073 K in tubular reformers. A side reaction, the reverse water gas shift, can also occur during DRM conditions to create water and CO. Methane steam reforming is mainly used to produce hydrogen since the H_2:CO ratio in the product stream is typically 3:1 or higher.[36-38] Currently, up to 95% of the U.S. production of H_2 is done through MSR.[39] The mixture of H_2

and CO gases, otherwise known as syngas (or synthesis gas), is used to make a variety of longer chain molecules. The classic and most historic example of this is the Fischer-Tropsch (FT) process that can create fuel-grade molecules from syngas. Depending on the desired product and the associated reaction chemistry, different ratios of H_2:CO are required as a feed stream. These ratios are almost always less than 3:1, and typically are 2:1 (for low-temperature FT), or 1:1 (for higher alcohol synthesis), or for methanol and DME syntheses the ratio of $(H_2 - CO_2)$:$(CO + CO_2)$ is approximately 2.[36] To bring down the ratio of H_2:CO, the stream is often put through reverse water gas-shift reactions to deplete H_2 and increase CO. Dry reforming has potential for dealing with this issue since the H_2:CO ratio is typically less than one. Not only does DRM use CO_2 instead of H_2O, but the resultant product stream can be blended with a stream from MSR to achieve a desired H_2:CO ratio for chemical synthesis.

Nickel is the primary catalyst used for these reforming reactions, but Ni catalysts are plagued by deactivation due to sintering and coking.[36, 40, 41] Sintering decreases the rate of reaction, but coking can eventually form enough carbon to shut the reaction down completely or totally clog reactors.[36] Examples of the types of carbon that can be deposited are shown below in Figure 1.3; whisker carbon is the most destructive form for industrial methane reforming. These carbon whiskers can lift the Ni particles off the support, and by continuously growing more carbon from the rear of the particle, the nanotubes can build up large pressure drops in the reactor, crush the catalyst particles against the walls of reformers, and decrease heat transfer from tubular reformers.

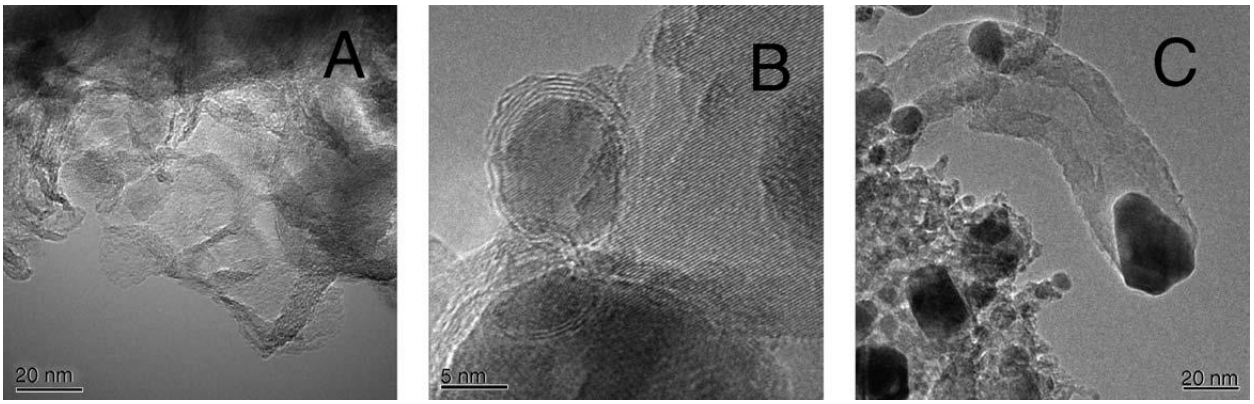

Figure 1.3. Three types of carbon deposition on Ni catalysts: (A) pyrolytic carbon, (B) encapsulating carbon, (C) whisker/nanotube carbon.[40]

Methane reforming can be run at higher temperatures (1073 to 1173 K) to thermodynamically limit the amount of carbon formed.[42] Not only are these temperatures extremely energy intensive and costly, but they also cause problems with decreased activity due to the formation of nickel-aluminates and excessive surface area loss due to sintering. For these reasons, much research has been conducted on finding ways to limit carbon deposition without using these high temperatures. One of the methods most pertinent to this thesis is to use small particles that destabilize carbon nucleation. A DFT study on graphite formation from decomposed CH_4 indicated that carbon preferentially nucleates on Ni(211) step edges as opposed to terrace sites.[7] However, the study also calculated that a critical size step edge greater than 2.5 nm was needed to anchor and form a stable carbon cluster on which more carbon can grow. This work aims to utilize 3-nm Ni particles to increase activity due to higher surface area and enhance coking resistance due to sufficiently small step edges.

Other attempts at increasing the stability and activity for DRM involve adding Pt to the Ni catalysts. Incorporating Pt can break up Ni ensembles, inducing the same effect of limiting Ni particle size. Additionally, Pt can increase the Ni reducibility (or keep Ni from losing activity

due to oxidation).[43-45] The limiting step for DRM reactions is the initial dissociative adsorption of CH_4, and Pt clusters are more reactive for C-H bond activation than Ni.[46] Several examples of adding Pt to Ni catalyst have shown improved activity and stability at temperatures of 773 to 1073 K.[43, 44, 47]

1.5 Oxidative dehydrogenation of propane over Pt catalysts

Another example of a reaction that could have large economic impacts with catalytic improvements in selectivity is the oxidative dehydrogenation (ODH) of alkanes to alkenes.[48] Oxidative dehydrogenation of propane (ODHP) to propylene is of particular interest. One of propylene's major uses is as the precursor for polypropylene, which is driving the global propylene demand to increase by more than 20 billion kg by 2017.[49] Steam crackers or fluid catalytic cracker (FCC) units are typically used to produce propylene, but catalytic dehydration is also used to a smaller extent. These processes are highly endothermic, produce larger fractions of ethylene than propylene, and require regeneration of the catalysts due to coking. Using O_2 to oxidatively dehydrogenate propane can ameliorate these issues by combusting carbon deposits and by dropping the necessary reaction temperatures below 773 K. Some of the main ODHP catalysts investigated are vanadia-based materials, but these catalysts cannot achieve high enough yields to warrant the industry abandoning more economical steam cracker and FCC processes.[50] These vanadia catalysts can achieve higher propylene yields than Pt catalysts; however, during propylene production, ethylene is also produced in significant amounts (50% of olefin production).[50]

Oxidative dehydrogenation on Pt is known as a structure sensitive reaction that increases turnover frequency as the catalyst particle size becomes smaller. Vajda *et al* showed through theoretical studies that clusters with surface coordination numbers of 4 have a lower barrier for

breaking a C-H bond than for breaking a C-C bond to form CO or CO_2, which is opposite behavior from higher-coordinated atoms. Larger Pt catalysts (composed of mainly (111) surfaces) or Pt(111) single crystals show essentially no selectivity to propylene and instead proceed through a combustion pathway. For example, in an ODHP study on Pt/monoliths by Silberova *et al.*, these catalysts only achieved a selectivity of 5% and a TOF of 0.01 s^{-1} at 673 K.[51] However, size-selected Pt clusters of 8 to 10 atoms have been shown to achieve propylene selectivities greater than 60%.[52] This work aims to use ALD to synthesize ~1 nm Pt nanoparticles that can approach the high ODHP selectivities reported for Vajda's small clusters.

1.6 Atomic layer deposition of metal nanoparticles

Atomic layer deposition is a two-step analog to chemical vapor deposition; it deposits conformal thin films on surfaces by two self-limiting reactions, *i.e.*, half-reactions. The self-limiting behavior allows for complete monolayers to be grown, theoretically one atomic layer at a time. One of the original, and most studied, examples of ALD is aluminum oxide deposition via trimethyl-aluminum and water.[53, 54] Alumina ALD has been demonstrated on a variety of metal oxides, metals, and polymers, as shown in Figure 1.4.[54-57] Most of the transition metals have been deposited by ALD as metal oxides or nitrides, but a more recent deposition method deposits elemental or metallic particles through island growth mechanisms.[53] Over a decade has lapsed since Aaltonen *et al.* used hundreds of cycles of $Me(Me_3Cp)Pt$ and O_2 to deposit Pt films via ALD.[58] Since that time, much research has focused on creating Pt nanoparticles by ALD with lower numbers of cycles on metal oxide supports such as Al_2O_3, SiO_2, TiO_2, and $SrTiO_3$.[15, 16, 59] Ruthenium, Pd, RuPt, and PdPt bimetallic catalysts were also deposited on metal oxide supports using ALD in recent years.[60-62]

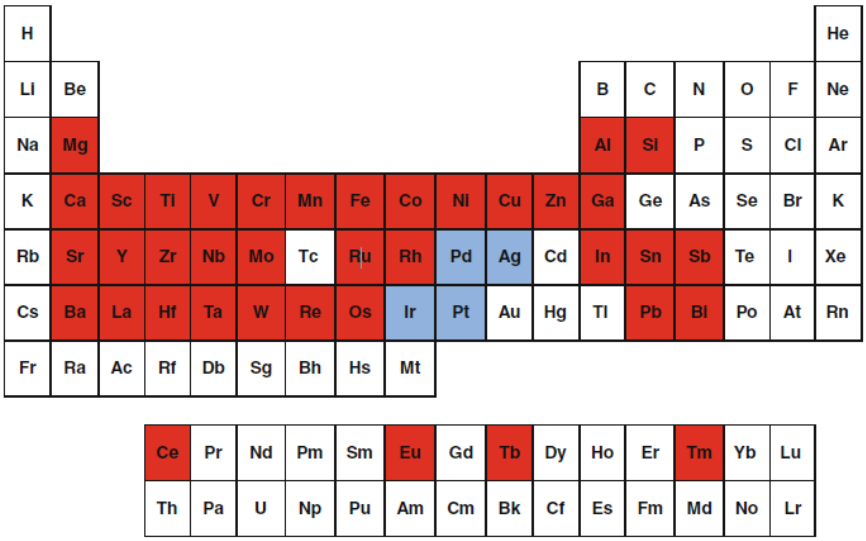

Figure 1.4. Demonstrated metal oxide chemistries shown in red, and metal ALD demonstrated in blue.[63] (this representation is missing (Cu, Co, Fe),[64] Ni,[64, 65] and Ru[61] from the demonstrated metal ALD elements.)

Platinum ALD is perhaps the most studied form of particle ALD because of the attractive properties of the Pt nanoparticles, and the ease at which the Pt ALD can be performed with the $Me_3Pt(MeCp)$ precursor. This wide usage of Pt ALD has led to several studies elucidating the Pt ALD reaction mechanism. Work by the Kessels group, through *in situ* FTIR monitoring of gas-phase products during ALD, showed that the initial reaction step involves the Pt precursor reacting with surface hydroxyl groups to form CH_4.[16, 66] The second half-reaction, involving O_2, combusts the remaining ligands to leave behind the Pt nanoparticles. The first half reaction, dosing the Pt precursor is [16]:

$$2(MeCp)PtMe_3(g) + 3\ O(ads) \rightarrow 2(MeCp)PtMe_2(ads) + CH_4(g) + CO_2(g) + H_2O(g)$$

The second half-reaction, using O_2 as the precursor is [16]:

$$2(MeCp)PtMe_2(ads) + 24\ O_2(g) \rightarrow 2\ Pt(s) + 3\ O(ads) + 16\ CO_2(g) + 13\ H_2O(g)$$

This Pt ALD mechanism was verified and expanded upon by Setthapun *et al.* by *in-situ* monitoring of Pt ALD with EXAFS and XANES.[15] Schematics of their proposed ALD

mechanisms are shown in Figure 1.5 and Figure 1.6. They found that during the second half-reaction, the O_2 forms Pt-O species that become reaction sites for subsequent ALD cycles. Although the reaction above is useful, and the schemes below in Figure 1.5 and Figure 1.6 are helpful for understanding the reactions taking place during ALD, these studies fail to address the issue of particle formation. The ALD may take place on an individual site as depicted in Figure 1.5, but the resultant material is not an individual atom of Pt and is instead a coalescence of many atoms. With the exception of their one study of Pt ALD with H_2,[15] all other metal nanoparticle ALD use the second half-cycle reagent of O_2 or formalin to deposit the nanoparticles.[16, 59-62, 66] Before the success of Ni ALD with H_2 shown in this work,[65] only noble metal nanoparticles were deposited via ALD.

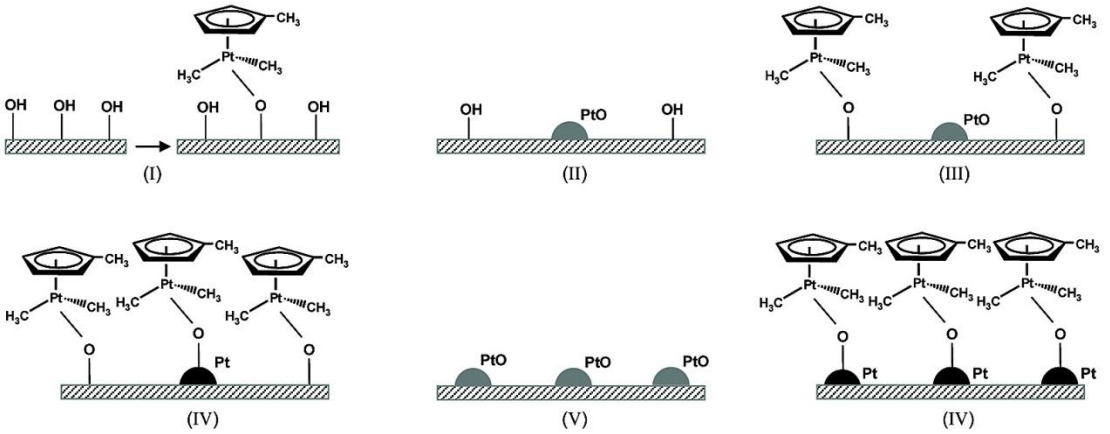

Figure 1.5. Reaction mechanism for Pt ALD with O_2 on γ-alumina. I: 1st Pt dose. II: 1st O_2 dose. III. 2nd Pt dose. IV: End of 2nd Pt dose. V: 2nd O_2 dose. VI: 3rd Pt dose.[15]

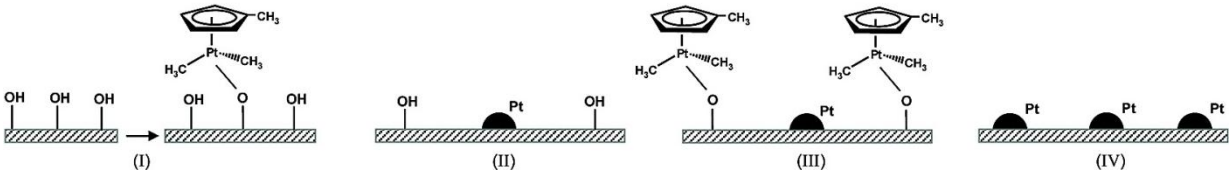

Figure 1.6.Reaction mechanism for Pt ALD with H_2 on γ-alumina. I: 1st Pt dose. II: 1st H_2 dose. III. 2nd Pt dose. IV: 2nd H_2 dose.[15]

As previously mentioned, precious metals such as Pt and Pd are often deposited at high dispersions to minimize raw materials costs. These catalysts also exhibit enhanced catalytic activity for certain reactions when they are ultra-small (< 2 nm).[62, 67] Palladium and Pt ALD naturally produce small particles, but several efforts have been made to decrease the particle size even further. Some studies have intentionally blocked or removed sites for Pd ALD, or attempted low temperature deposition to slow diffusion.[67, 68] Several studies have used DFT to probe how Pt and Pd atoms adsorb and diffuse and nucleate on TiO_2 and Al_2O_3 supports.[69-71] These studies found that hydroxyl groups on the alumina surface can decrease the adsorption energy of these metal atoms, and the OH groups also increase the diffusion barrier for migration across the support surface.[70, 71]

1.7 Catalyst Stabilization by ALD and Molecular Layer Deposition

Although many of the nanoparticle catalysts discussed in this thesis have extraordinary catalytic performance in their native, as-synthesized state, a major barrier to implementation of these technologies is sintering of the catalysts. Catalyst nanoparticles sinter through two primary mechanisms depicted in Figure 1.7: 1) particle coalescence, whereby entire catalyst particles migrate across the surface, and 2) Ostwald ripening, where larger catalyst particles grow to become more stable at the expense of atom loss from smaller catalyst particles.[41, 72, 73] Sintering becomes more of an issue as particle size decreases, since one of the driving forces for particle growth is minimization of surface energy of the particle, and this surface energy is highest on smaller particles.[3, 69]

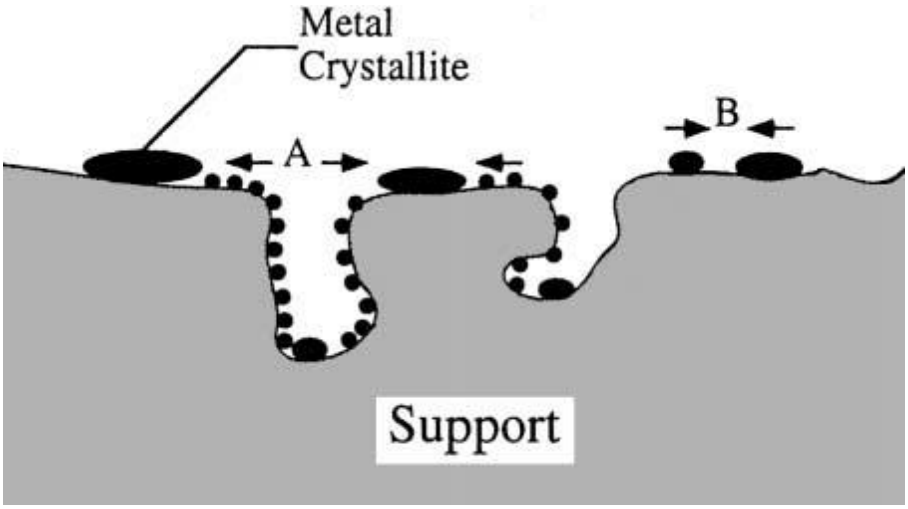

Figure 1.7. Conceptual figure for sintering mechanisms: A) Ostwald Ripening includes atomistic loss (represented by the small black spheres above) and re-adsorption from small particles to larger ones, and B) particle coalescence, which involves two entire crystallites moving together to form one particle.[73]

Although many stabilization techniques are used in the literature and industry, the scope of this background information will focus on a few promising alumina-ALD and molecular layer deposition (MLD) stabilization techniques. The first of these investigations used 40 cycles of alumina ALD to completely cover Pd catalyst particles with an 8-nm-thick film, then exposed the Pd particles by thermally cracking the alumina layer at 1073 K in O_2 to form 2-nm pores down to the Pd particle surface.[74] The main advantage of this layer was the covering of certain active sites that nucleated carbon growth. The particles were also stabilized by this technique, but they were much larger (7 nm) and thus less susceptible to sintering than the catalysts investigated for this thesis.

Instead of forming a complete over-coating, the same authors also used fewer numbers of cycles to deposit an incomplete alumina layer on the Pd nanoparticles. Through CO DRIFTS, they determined that the alumina ALD nucleated on the step and corner sites of the Pd particles, while leaving the terraces open for reaction. This porous coating slightly prevented the particles from sintering during reaction conditions, and significantly prevented sintering compared to an

uncoated catalyst under Ar for 6 h at 773 K. A third ALD-based technique is called ABC ALD chemistry, where instead of two half-reactions, a third reaction is used in between the regular two half-reactions. This third reaction does not interfere with the species stabilized by ligands from the first reaction, and can instead be used to build up material around the catalyst particles to stabilize them. Lu *et al.* found that these "walls" created around Pd-ALD catalysts stabilized the particles during synthesis to 1 nm in diameter or less; however, no substantial evidence was presented to show that these structures prevent sintering at high temperatures or reaction conditions.

Molecular layer deposition is another stabilization technique similar to ALD's self-limiting, controllable properties, but instead of depositing atomic layers of metal oxides, MLD deposits metal-organic polymer layers composed of molecules (not atoms) from each complete cycle. Once the desired number of cycles are deposited, the MLD layer is calcined (or water-etched) to remove the polymeric components, leaving behind a porous alumina layer. The simplest form of MLD involves two half-reactions, much like ALD, and the work demonstrated by the Weimer group focused on aluminum alkoxide (*i.e.*, alucone) MLD.[75, 76] This reaction typically uses TMA and ethylene glycol as the two reagents to create the polymeric hybrid film, which when calcined produced a porous inorganic layer with 0.6-nm diameter pores. Liang *et al.* used these MLD layers to stabilize Pt-ALD particles on SiO_2 by depositing 10, 20, 30, and 40 MLD layers.[76] Active metal surface area was partially covered by the MLD layers, but was similar for the 20, 30, and 40-cycle samples at room temperature and 673 K. When they held the catalysts at 873 K to cause sintering, the MLD-modified catalysts had similar active metal surface areas. When the catalysts were sintered at 1073 K, the sample with the thickest MLD layer (40 MLD cycles) had the smallest amount of sintering (11% active surface area loss)

compared to the 34% loss for the 30-cycle sample or the 69% loss for the 10-cycle sample. A schematic depicting this coating is shown in Figure 1.8.

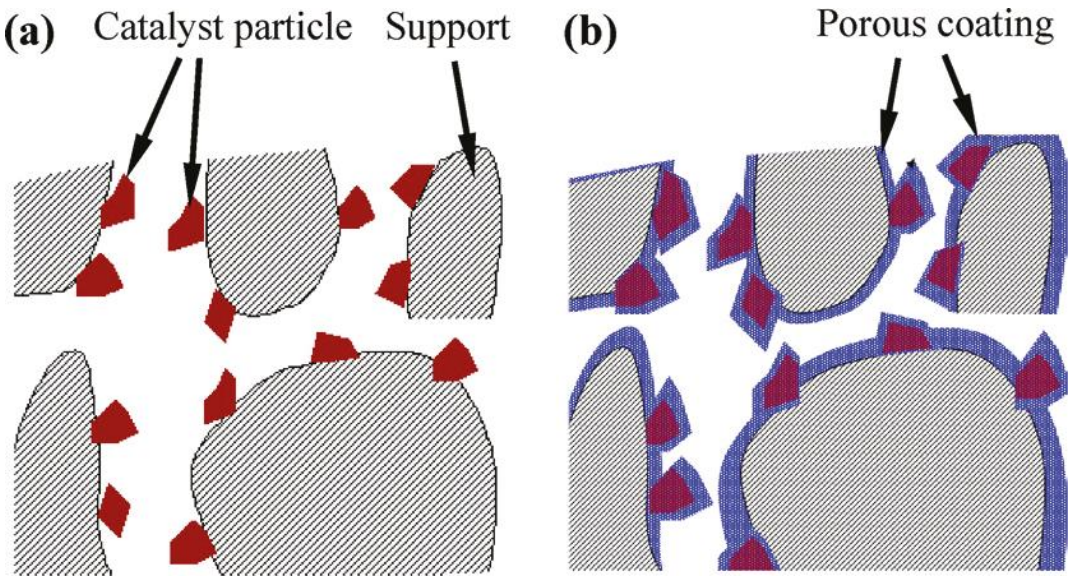

Figure 1.8 Schematic of supported Pt catalyst nanopartilces: (a) uncoated, as deposited by ALD, (b) Pt particles coated by hybrid polymer-inorganic MLD, then calcined to form stabilizing porous alumina layer.[75]

The catalytic activity for CO oxidation on these Pt catalysts was decreased by the addition of MLD layers. This decrease in activity was attributed to mass transfer limitations from the 0.6-nm pores. A new type of alucone MLD using three components (ABC MLD) was reported by Yoon *et al.* and still had self-limiting conformal film growth like AB MLD.[77] In this approach, the three reagents are TMA, ethyl amine (EA), and maleic anhydride (MA). Each component undergoes a self-limiting reaction, as shown in Figure 1.9,[77] to form a longer polymeric chain than the AB alkoxide MLD.

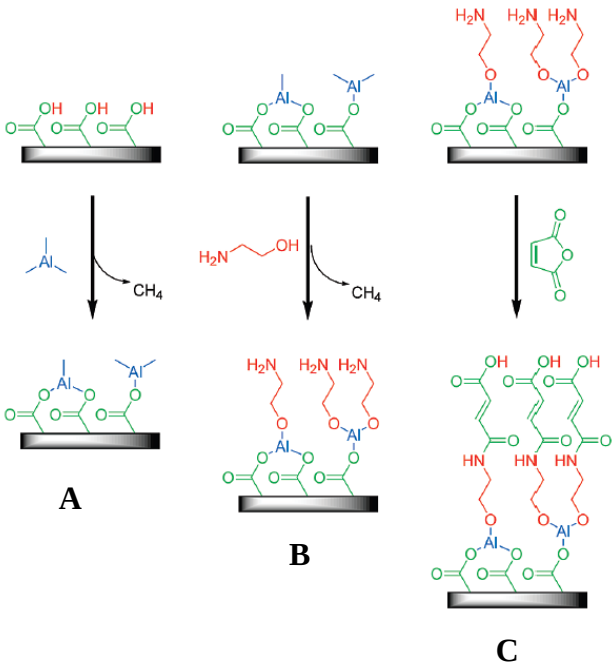

Figure 1.9: ABC alucone MLD reaction scheme. A: TMA reacts on the OH groups of the support or the previous MLD layer in the "A" dose; B: EA reacts with methyl groups from the first step; C: MA reacts with the amine groups from the second step to form a metal-organic polymer layer, and regenerates OH functionality for additional ABC cycles.[77]

Liang *et al.* showed that after removal of the organic portion of these layers, the pores are 0.8-nm diameter.[75] These pores should mitigate mass-transfer issues for reactions of small molecules, but the ABC MLD layers were not previously tested for sintering prevention or on any catalyst system to gauge the effect of the MLD layer on activity.

1.8 Thesis Objectives

This thesis aims to demonstrate and understand the advantages of synthesizing nanostructured supported catalysts via atomic layer deposition (ALD). The catalytic systems under investigation are Al_2O_3-supported Ni, Pt, and NiPt bimetallic catalysts synthesized mainly by H_2 ALD. The catalysts synthesized in this work are among the smallest supported nanoparticles ever reported, and are in the size range where nanoscale effects can drastically change reaction activity and selectivity.[26-28, 30] Increased reaction selectivity can arise from specific sites (such as step edges or other lower-coordinated atoms) on the catalyst surface, and increased catalytic activity can come from higher fractional exposure of metal atoms on the nanoparticle surface.

This work has successfully synthesized Ni nanoparticles by ALD, and demonstrated that these particles are sufficiently small to exhibit catalytic enhancements based on the nanoscale features of the metal. As an extension of Ni nanoparticle ALD with H_2, we hypothesized that using H_2 as the second half-cycle reagent alters the Pt ALD mechanism and particle size compared to traditional Pt ALD with O_2. By combining the two metal ALD chemistries, nanoscale bimetallic catalysts were created and showed enhanced activity and coking resistance during DRM. Additionally, we hypothesized that nanoscale effects can be enhanced and maintained in harsh industrially-relevant conditions by modifying the Ni nanoparticles with Pt ALD and further with a stabilizing alumina MLD layer. This thesis aims to explore the synthesis, modification, and performance of these ALD catalysts through four specific objectives:

1 Synthesize supported Ni nanoparticles by ALD to enhance hydrogenolysis selectivity.

This work demonstrates the first non-noble metal ALD of nanoparticles by depositing Ni with $NiCp_2$ and H_2 reagents. The particle size and Ni weight loading deposited varied with the number of ALD cycles performed, and the Ni ALD was able to achieve relatively small particles for such high weight loadings. The small Ni particles had an increased number of step-edges on their surfaces, which correlated with increased hydrogenolysis selectivity and activity.

2 Investigate the effects of varying Pt ALD second half-reaction chemistries on the ALD mechanism, nanoparticle size, nanoscale features, and ODHP selectivity.

In contrast to Ni ALD, Pt nanoparticles can be synthesized via ALD using either O_2 or H_2 as the secondary reagent. This work aims to understand some of the mechanistic differences associated with the two reaction chemistries of Pt ALD by monitoring the support OH concentration via *in situ* IR during the ALD process. Additionally, the differences in nanoparticle size as a function of chemistry and number of cycles were analyzed. The surface structures of the catalysts were probed through CO adsorption and analysis by TPD or CO DRIFTS. The catalysts were evaluated for selectivity of propane oxidative dehydrogenation (ODH), which is known to take place on low coordination number (CN = 4) Pt atoms.[52] These Pt ALD particles are among some of the smallest ever synthesized with a feasibly scalable technique and bridge the gap of controlled molecular-beam deposited clusters and actual supported Pt clusters.

3 Modify Ni ALD particles with Pt ALD to enhance both activity and stability during dry reforming of methane.

This study aims to evaluate Ni ALD and NiPt catalysts for DRM activity. Ni ALD monometallic catalysts have high surface areas per gram of metal, and are sufficiently small to

limit the deactivation of the catalyst due to coking. Long term stability of these catalysts and the degree of coke build-up compared to normal incipient wetness Ni catalysts was investigated. Bimetallic catalysts were created by coating the Ni ALD catalysts with Pt ALD to improve DRM performance. The Pt addition enhanced both activity and coking resistance of the Ni nanoparticles.

4 Modify Ni and NiPt ALD particles with stabilizing Al_2O_3 MLD layers to enhance activity and resistance to coking by reducing sintering during dry reforming of methane.

This work focused on demonstrating the potential of MLD to minimize sintering, thereby retaining the nanoscale advantages of these catalyst nanoparticles. The catalysts were intentionally tested under extremely harsh conditions (DRM at 973 K) to show the maximum benefit of the MLD layers under conditions that readily sinter and deactivate catalysts. Porous alumina stabilizing layers were added to the Ni and NiPt ALD catalysts by depositing alucone ABC MLD, then calcining the layers to form porous alumina. Stability studies, catalyst characterization techniques such as chemisorption, TEM, and coke formation measurements were performed. The effectiveness of these stabilizing layers on reducing sintering and maintaining high DRM rates was found to vary with the number of MLD cycles, but the sintering was reduced in all cases. The MLD layers on the Ni catalysts were more effective at maintaining a high DRM rate than the NiPt catalysts.

1.9 References

[1] D.W. Wolfe, Tales from the underground: a natural history of subterranean life, Basic Books, 2001.
[2] J.N. Armor, Catalysis Today 163 (2011) 3-9.
[3] C.N. Satterfield, Heterogeneous catalysis in practice, McGraw-Hill New York, 1980.
[4] J. Weitkamp, Solid State Ionics 131 (2000) 175-188.
[5] R.P.H. Gasser, G. Ehrlich, Physics Today 40 (1987) 128.
[6] G.A. Somorjai, H. Frei, J.Y. Park, Journal of the American Chemical Society 131 (2009) 16589-16605.
[7] H. Bengaard, J.K. Nørskov, J. Sehested, B.S. Clausen, L.P. Nielsen, A.M. Molenbroek, J.R. Rostrup-Nielsen, Journal of Catalysis 209 (2002) 365-384.
[8] S. Alayoglu, A.U. Nilekar, M. Mavrikakis, B. Eichhorn, Nat Mater 7 (2008) 333-338.
[9] M. Mavrikakis, P. Stoltze, J.K. Nørskov, Catalysis Letters 64 (2000) 101-106.
[10] M.T. Schaal, M.P. Hyman, M. Rangan, S. Ma, C.T. Williams, J.R. Monnier, J.W. Medlin, Surface Science 603 (2009) 690-696.
[11] B.K. Teo, EXAFS: basic principles and data analysis, Springer-Verlag Berlin, 1986.
[12] D. Koningsberger, R. Prins, (1987).
[13] B.J. Kip, F.B.M. Duivenvoorden, D.C. Koningsberger, R. Prins, Journal of Catalysis 105 (1987) 26-38.
[14] J.F. Watts, J. Wolstenholme, An Introduction to Surface Analysis by XPS and AES, by John F. Watts, John Wolstenholme, pp. 224. ISBN 0-470-84713-1. Wiley-VCH, May 2003. 1 (2003).
[15] W. Setthapun, W.D. Williams, S.M. Kim, H. Feng, J.W. Elam, F.A. Rabuffetti, K.R. Poeppelmeier, P.C. Stair, E.A. Stach, F.H. Ribeiro, J.T. Miller, C.L. Marshall, The Journal of Physical Chemistry C 114 (2010) 9758-9771.
[16] W. Kessels, H. Knoops, S. Dielissen, A. Mackus, M. van de Sanden, Applied Physics Letters 95 (2009) 013114-013114-013113.
[17] G.A. Somorjai, R.L. York, D. Butcher, J.Y. Park, Physical Chemistry Chemical Physics 9 (2007) 3500-3513.
[18] B. Hammer, J.K. Nørskov, H.K. Bruce C. Gates, Theoretical surface science and catalysis - calculations and concepts, in: Advances in Catalysis, Academic Press, 2000, pp. 71-129.
[19] J.K. Nørskov, T. Bligaard, A. Logadottir, S. Bahn, L.B. Hansen, M. Bollinger, H. Bengaard, B. Hammer, Z. Sljivancanin, M. Mavrikakis, Y. Xu, S. Dahl, C.J.H. Jacobsen, Journal of Catalysis 209 (2002) 275-278.
[20] M.M. Montemore, J.W. Medlin, The Journal of Physical Chemistry C 117 (2013) 20078-20088.
[21] G. Jones, J.G. Jakobsen, S.S. Shim, J. Kleis, M.P. Andersson, J. Rossmeisl, F. Abild-Pedersen, T. Bligaard, S. Helveg, B. Hinnemann, J.R. Rostrup-Nielsen, I. Chorkendorff, J. Sehested, J.K. Nørskov, Journal of Catalysis 259 (2008) 147-160.
[22] J. Greeley, M. Mavrikakis, Nature materials 3 (2004) 810-815.
[23] G.A. Somorjai, Y. Li, Introduction to surface chemistry and catalysis, John Wiley & Sons, 2010.
[24] I. Chorkendorff, J.W. Niemantsverdriet, Concepts of modern catalysis and kinetics, Wiley. com, 2006.
[25] Current Metal Prices, in, Prospecting and Mining Journal, 2013.
[26] G.C. Bond, Surface Science 156, Part 2 (1985) 966-981.

[27] R.A. Van Santen, Accounts of Chemical Research 42 (2008) 57-66.
[28] R.V. Hardeveld, F. Hartog, Advances in Catalysis 22 (1972) 75-110.
[29] R. Van Hardeveld, A. Van Montfoort, Surface Science 4 (1966) 396-430.
[30] G.C. Bond, Chemical Society Reviews 20 (1991) 441-475.
[31] F. Abild-Pedersen, J. Greeley, J. Nørskov, Catalysis Letters 105 (2005) 9-13.
[32] F. Studt, F. Abild-Pedersen, T. Bligaard, R.Z. Sørensen, C.H. Christensen, J.K. Nørskov, Science 320 (2008) 1320-1322.
[33] Y. Li, G.A. Somorjai, Nano Letters 10 (2010) 2289-2295.
[34] K.R. Kahsar, D.K. Schwartz, J.W. Medlin, Journal of the American Chemical Society (2013).
[35] P. Gallezot, D. Richard, Catalysis Reviews 40 (1998) 81-126.
[36] J.R. Rostrup-Nielsen, J. Sehested, J.K. Nørskov, Hydrogen and synthesis gas by steam- and C02 reforming, in: Advances in Catalysis, Academic Press, 2002, pp. 65-139.
[37] S. Wang, G.Q. Lu, G.J. Millar, Energy & Fuels 10 (1996) 896-904.
[38] J.H. Edwards, A.M. Maitra, Fuel Processing Technology 42 (1995) 269-289.
[39] Natural Gas Reforming, in: U.S.D.o. Energy (Ed.), U.S. Department of Energy, 2013.
[40] J. Sehested, Catalysis Today 111 (2006) 103-110.
[41] J. Sehested, Journal of Catalysis 217 (2003) 417-426.
[42] M. Gharibi, F.T. Zangeneh, F. Yaripour, S. Sahebdelfar, Applied Catalysis A: General 443-444 (2012) 8-26.
[43] M. García-Diéguez, I.S. Pieta, M.C. Herrera, M.A. Larrubia, L.J. Alemany, Applied Catalysis A: General 377 (2010) 191-199.
[44] M. García-Diéguez, E. Finocchio, M.Á. Larrubia, L.J. Alemany, G. Busca, Journal of Catalysis 274 (2010) 11-20.
[45] S.R. de Miguel, I.M.J. Vilella, S.P. Maina, D.S. José-Alonso, M.C. Román-Martínez, M.J. Illán-Gómez, Applied Catalysis A: General (2012).
[46] D. Li, Y. Nakagawa, K. Tomishige, Applied Catalysis A: General 408 (2011) 1-24.
[47] B. Pawelec, S. Damyanova, K. Arishtirova, J.L.G. Fierro, L. Petrov, Applied Catalysis A: General 323 (2007) 188-201.
[48] E.L. Hu, S.M. Davis, R. Davis, E. Scher, Applications: Catalysis by Nanostructured Materials: Nanotechnology Research Directions for Societal Needs in 2020, in, Springer Netherlands, 2011, pp. 445-466.
[49] Ceresana, Market Study: Propylene (UC-1705), in, Ceresana, 2011.
[50] F. Cavani, N. Ballarini, A. Cericola, Catalysis Today 127 (2007) 113-131.
[51] B. Silberova, M. Fathi, A. Holmen, Applied Catalysis A: General 276 (2004) 17-28.
[52] S. Vajda, M.J. Pellin, J.P. Greeley, C.L. Marshall, L.A. Curtiss, G.A. Ballentine, J.W. Elam, S. Catillon-Mucherie, P.C. Redfern, F. Mehmood, P. Zapol, Nat Mater 8 (2009) 213-216.
[53] S.M. George, Polymer 1550 (2012) 125.
[54] R.L. Puurunen, Journal of applied physics 97 (2005) 121301-121301-121352.
[55] D.M. King, J.A. Spencer Ii, X. Liang, L.F. Hakim, A.W. Weimer, Surface and Coatings Technology 201 (2007) 9163-9171.
[56] J. Elam, D. Routkevitch, P. Mardilovich, S. George, Chemistry of Materials 15 (2003) 3507-3517.
[57] D.M. King, X. Liang, A.W. Weimer, Powder Technology 221 (2012) 13-25.
[58] T. Aaltonen, M. Ritala, T. Sajavaara, J. Keinonen, M. Leskela¨, Chemistry of Materials 15 (2003) 1924-1928.

[59] J. Li, X. Liang, D.M. King, Y.-B. Jiang, A.W. Weimer, Applied Catalysis B: Environmental 97 (2010) 220-226.
[60] X. Liang, L. Lyon, Y.-B. Jiang, A. Weimer, Journal of Nanoparticle Research 14 (2012) 1-12.
[61] S.T. Christensen, H. Feng, J.L. Libera, N. Guo, J.T. Miller, P.C. Stair, J.W. Elam, Nano Letters 10 (2010) 3047-3051.
[62] Y. Lei, B. Liu, J. Lu, R.J. Lobo-Lapidus, T. Wu, H. Feng, X. Xia, A.U. Mane, J.A. Libera, J.P. Greeley, J.T. Miller, J.W. Elam, Chemistry of Materials 24 (2012) 3525-3533.
[63] P. Stair, Topics in Catalysis 55 (2012) 93-98.
[64] B.S. Lim, A. Rahtu, R.G. Gordon, Nat Mater 2 (2003) 749-754.
[65] T.D. Gould, A.M. Lubers, B.T. Neltner, J.V. Carrier, A.W. Weimer, J.L. Falconer, J. Will Medlin, Journal of Catalysis 303 (2013) 9-15.
[66] A.J.M. Mackus, N. Leick, L. Baker, W.M.M. Kessels, Chemistry of Materials 24 (2012) 1752-1761.
[67] H. Feng, J.A. Libera, P.C. Stair, J.T. Miller, J.W. Elam, ACS Catalysis 1 (2011) 665-673.
[68] J. Lu, P.C. Stair, Angewandte Chemie International Edition 49 (2010) 2547-2551.
[69] Y. Zhou, C.L. Muhich, B.T. Neltner, A.W. Weimer, C.B. Musgrave, The Journal of Physical Chemistry C 116 (2012) 12114-12123.
[70] N. Aaron Deskins, D. Mei, M. Dupuis, Surface Science 603 (2009) 2793-2807.
[71] M. Corral Valero, P. Raybaud, P. Sautet, The Journal of Physical Chemistry B 110 (2006) 1759-1767.
[72] C.H. Bartholomew, Applied Catalysis A: General 107 (1993) 1-57.
[73] C.H. Bartholomew, Applied Catalysis A: General 212 (2001) 17-60.
[74] J. Lu, B. Fu, M.C. Kung, G. Xiao, J.W. Elam, H.H. Kung, P.C. Stair, Science 335 (2012) 1205-1208.
[75] X. Liang, B. W Evanko, A. Izar, D. M King, Y.-B. Jiang, A.W. Weimer, Microporous and Mesoporous Materials (2012).
[76] X. Liang, J. Li, M. Yu, C.N. McMurray, J.L. Falconer, A.W. Weimer, ACS Catalysis 1 (2011) 1162-1165.
[77] B. Yoon, D. Seghete, A.S. Cavanagh, S.M. George, Chemistry of Materials 21 (2009) 5365-5374.

Chapter 2: Synthesis of Supported Ni Catalysts by Atomic Layer Deposition

As accepted by *Journal of Catalysis* (July 2013)

2.1 Abstract

Nickel nanoparticles grown on an Al_2O_3 support by atomic layer deposition (ALD) had higher selectivity for propylene hydrogenolysis. The Ni was deposited in a fluidized bed reactor with bis(cyclopentyldienyl)Ni and H_2 reactants. Varying the number of ALD cycles varied the Ni loading between 4.7 - 16.8 wt% and the average Ni particle diameters between 2.4 - 3.3 nm. The number of surface sites per gram of Ni, determined from CO TPD, was at least five times higher on ALD-prepared catalysts than typical Ni/Al_2O_3 catalysts prepared by incipient wetness impregnation. The fraction of CO desorbed from steps and kinks on the ALD-prepared catalysts was at least three times higher. Correspondingly, the selectivity for propylene hydrogenolysis, instead of hydrogenation, was above 10% on an ALD-prepared catalyst but below 0.4% on the incipient wetness catalyst. Preparing catalysts by ALD appeared to increase the step and kink site density and thus increase hydrogenolysis selectivity.

2.2 Introduction

To meet the demand for high performance catalysts in the petroleum and biofuels industries, efforts have increased to rationally design and synthesize catalysts that enhance selectivity, activity, and/or robustness.[1-3] Catalytic performance can be enhanced by designing catalysts based on theory of highly idealized structures, including fundamental ultra high vacuum (UHV) studies of single crystals,[4-7] and DFT modeling of nanoclusters with nanoscale and bimetallic features.[8-10] For example, Hang *et al.* used DFT and STEM to elucidate how step edges on a Ni(211) surface enhance ethylene hydrogenolysis compared to a Ni(111) surface.[10, 11] Designing catalysts with nanoscale features can improve activity and

selectivity by increasing uncoordinated surface sites and defects.[11-13] Not only do nanostructured catalysts have high activity per gram of metal because they have higher dispersions, but the inherent nanoscale features can also allow catalysts to have different turnover frequencies or selectivities than bulk materials.[12, 14-16] In the case of structure sensitive reactions such as hydrogenolysis, enhancements in selectivity can arise from both electronic effects and ensemble size effects as the metal particles become smaller.[17, 18]

Although understanding the catalytic properties of nanoparticles has improved, a gap still exists between studies on model systems and synthesizing nanoscale heterogeneous catalysts with enhanced performance. In many nanotechnology applications, one large barrier to implementation is converting the technology to a large-scale, reliable process.[12] Most nanoparticle synthesis techniques that can achieve supported catalyst particles with diameters of 2 to 3 nm involve solution-based particle growth, often with hazardous solvents, reducing agents, or capping agents. Additional steps necessary to deposit the particles are photodegradation, polyol deposition, or multi-step processes of impregnation, exchange or anchoring the particles to the support, followed by calcination and reduction.[19-21] This issue of scalability can be addressed by utilizing atomic layer deposition (ALD) as a gas-phase technique in a fluidized bed reactor (FBR) to synthesize high-performance nanoparticle catalysts directly on the support.[22] Atomic layer deposition is similar to chemical vapor deposition, except that the two reactants are dosed in two "half reactions" or "half cycles" to allow for a site specific reaction with the first reactant, followed by a second reaction to achieve the desired material deposition.[23]

Deposition of noble metal nanoparticles of Pt, Ru and Pd on several metal oxide supports by ALD has been demonstrated by using a variety of cyclopentyldienyl-based metal precursors for Pt and Ru and a hexafluoroacetylacetonate precursor for Pd.[24-27] Depositing noble metals

with less than 10 ALD cycles produces clusters with diameters less than 2 nm and high dispersions (0.40 – 0.90).[24-26] The ALD process yields exceptionally small nanoparticles that can be stabilized by modification with other materials such as porous alumina ALD over-layers to prevent coking or sintering.[28, 29] During metal ALD, oxygen is typically used as the reagent of the second half reaction for Pt, Ru, and most other ALD cycles that use cyclopentadienyl organometallic precursors. Atomic layer deposition with O_2 leads to nanoparticle deposition of the noble metals,[30] but for other transition metals such as Co, Fe, and Ni, only metal oxide films deposit using O_2 or ozone as the second precursor.[31-34] Metallic films have been synthesized using O_2 as the second precursor with Ni organometallic precursors, but only by reducing the deposited metal oxide film with H_2 or H radicals.[23] Reducing agents as the second reactant have only been demonstrated with noble metals and copper, or to create thick metallic films.[35, 36]

In the present work, we demonstrate how ALD provides a scalable avenue for producing supported Ni nanoparticles of specific sizes with nanostructures necessary for higher hydrogenolysis selectivities and activities. Varying the number of ALD cycles deposited nanoparticles with different physical and chemical properties. The mass and size of particles deposited were measured via inductively coupled plasma mass spectroscopy (ICP-MS) and transmission electron microscopy (TEM). Temperature-programmed desorption (TPD) of CO was performed to validate active site calculations based on particle size and to elucidate any differences in CO desorption modes between the catalysts. Propylene hydrogenation and hydrogenolysis rates were measured to evaluate activity and selectivity advantages of preparing catalyst nanoparticles via ALD.

2.3 Materials and Methods

2.3.1 Nickel ALD Catalyst Preparation

Nickel was deposited on alumina particles by first reacting bis(cyclopentadienyl)nickel ($NiCp_2$) in a N_2 carrier gas with alumina, and then reacting 20% H_2 (balance Ar) with the organometallic molecules bound to the surface. The solid $NiCp_2$ precursor was loaded into a stainless steel vessel, which was purged with N_2 and then held at 365 K to control the precursor vapor pressure.

Varying numbers of cycles were used on separate batches of the support, which was either a porous alumina powder (Albemarle MARTOXID AN/I) or a non-porous alumina powder with nanospheres less than 50 nm in diameter (Aldrich 544833 gamma alumina, ~40m^2/g BET surface area). Thermogravimetric analysis, similar to the method proposed by Rigney et al.[37], was used to estimate the OH surface density of the gamma alumina nanospheres on a Netzsch STA 449 F1 Jupiter thermogravimetric analyzer. The alumina sample was heated at a ramp rate of 10 K/min from room temperature to 1273 K in a flow of 100 sccm Ar in order to remove both adsorbed water and surface hydroxyl groups. The weight loss after 673 K was attributed to OH removal via water desorption. This temperature cutoff was determined by an inflection in the derivative of weight loss and because liquid water is known to be mostly removed by heating at 673 K.[38]

All ALD reactions were monitored *in situ* by mass spectrometry (Stanford Research Systems QMS 200) and took place at 573 K at approximately 0.1 Pa in a vertical fluidized bed reactor system, which is described in detail elsewhere.[22] The support was degassed overnight in the reactor under a N_2 flow of 5 sccm, and all carrier gas and reagent gas streams were set to 5 sccm, resulting in a bed space velocity of 0.73 h^{-1}. Mass spectrometry scans from 1-200 m/z

revealed species correlated to the ALD reaction as 28 (N_2), 44 (CO_2), 40 (C_3 fragment), 66 (cyclopentadiene, Cp), 187 and 188 ($NiCp_2$) for the first half reaction, and 66 (C_5H_6), 2 (H_2), and 16 (CH_4) for the second half reaction. Breakthrough of $NiCp_2$ occurred for all cycles with dose times ranging from 5 min to 2 h for up to 1 g of support. The ALD-synthesized catalysts were compared to a Ni catalyst (8 wt% Ni) prepared by incipient wetness (IW). The catalyst was prepared by dissolving $Ni(NO_3)_2 \cdot 6H_2O$ in deionized water, adding the 0.67 g $Ni(NO_3)_2$ / L solution to the porous Al_2O_3 support (Saint Gobian SA 63158 with a pore volume of 0.64 g/cm^3), drying the catalyst at 383 K for 2 h, then increasing the temperature at approximately 10 K/min to 823 K and calcining at 823 K for 6 h. The catalyst was then reduced for 3 h at 623 K in pure H_2.

2.3.2 Catalyst Characterization

Nickel, aluminum, and impurity silicon content were measured using inductively coupled plasma mass spectroscopy (ICP-MS). The catalysts were digested in a HF/aqua regia solution for at least 24 h before analysis. Transmission electron microscopy (TEM) images of the catalyst particles were obtained using a Philips CM-100 microscope. Powder samples were embedded in epoxy, cured at 333 K for two days, and cross sectioned using a Leica UC6 Ultramicrotome to thicknesses of 50-70 nm. High resolution transmission electron microscopy (HRTEM) images were obtained using a JEOL 2010 FEG (Field Emission Gun) Analytical Electron Microscope at the MIT SEF (shared experimental facility), using the Orius CCD. Samples were prepared for the HRTEM using epoxy-embedded cross-sections or by dropping powders suspended in isopropanol onto holey carbon grids and wicking away the excess liquid to deposit the particles on the grid. Due to the difficulty in distinguishing the smaller and less densely populated particles of 1 and 5 ALD cycles, Al_2O_3 nanospheres were used to facilitate imaging the Ni

particles, whereas the 15 ALD cycle sample was imaged on a porous Al_2O_3 substrate. Nickel particle diameters were measured via NIST ImageJ software with the HRTEM and TEM images.

2.3.3 Reactor Studies/ CO TPD

A differential reactor composed of a 6.35-mm ID quartz tube in a temperature-controlled furnace was used to measure reaction kinetics and carry out temperature-programmed desorption (TPD). Reactor feed and effluent were analyzed on a SRS-RGA200 mass spectrometer. All catalysts were reduced at 573 K in 20% H_2 (balance Ar) for 2 h before exposure to reaction conditions. Hydrogenation and hydrogenolysis were monitored at temperatures from 323 K to 573 K at flows of 10/40/50 sccm of $C_3H_6/H_2/Ar$. Less than 10 mg of catalyst powder was mixed with inert zirconia to a total bed weight of 500 mg. Propylene was used as a probe molecule to screen for hydrogenation and hydrogenolysis rates. Turnover frequencies (TOF) were calculated using the rate of product formation (after reaching steady state values) and the number of metal surface sites determined by CO TPD.

For TPD, 100-300 mg of catalyst were loaded into the quartz tube and then reduced in 20% H_2 for 2 h at 573 K, purged with Ar, and cooled for 2 h to room temperature. Carbon monoxide was adsorbed to saturation from a stream of 20% CO (balance Ar) at room temperature at a flow rate of 100 sccm for 10 min. The temperature was increased from room temperature to 798 K at approximately 100 K/min in a sweep gas of 25 to 50 sccm Ar.

2.4 Results and Discussion

2.4.1 Preparation of Ni Metal Nanoparticles via ALD with H_2

The Ni nanoparticles were deposited on alumina while effluent gas from the FBR was monitored via mass spectrometry. Figure 2.10a shows in situ mass spectrometry signals for the

first ALD half-reaction, and Scheme 2.1 shows a surface reaction mechanism consistent with experimental observations. Immediately following the introduction of the precursor, the signal for the Cp ring m/z=66 increased, indicating cleavage of the ring during the deposition reaction. A fraction of the organic ligands from the Cp groups were also oxidized to CO_2, likely because of contaminant O_2 in the reactor streams or O_2 adsorbed on previously deposited metal within the reactor. We propose that the O-H bond of a surface hydroxyl group was replaced by an O-Ni bond when the $NiCp_2$ precursor reacted with the surface OH groups, much like the replacement of the O-H bond with a O-Pt bond, detected by in-situ XAFS of Pt ALD.[39] As discussed below, this first reaction step also left species bound to the Ni atoms in the form of Cp groups and possibly other carbonaceous fragments, which are similar to those determined from *in situ* gasphase infra-red analysis and detected by x-ray adsorption techniques during the first step of Pt ALD.[30, 39]

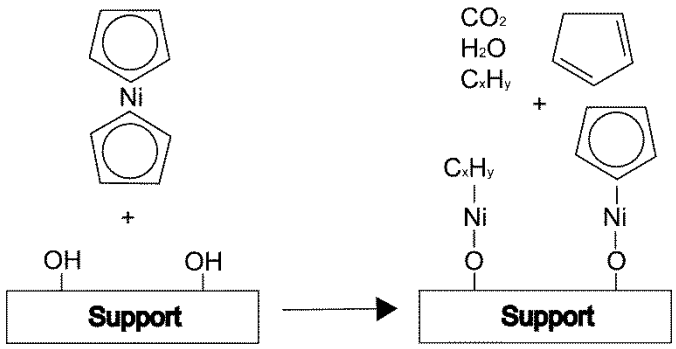

Scheme 2.1. Reaction scheme for first ALD half reaction in which the $NiCp_2$ precursor reacts with surface OH.

The intact $NiCp_2$ precursor appeared in the reactor effluent after 5 min, indicating that the available surface sites were beginning to saturate. The Cp ring signal decreased simultaneously, but at a slower rate because the Cp ring adsorbed and desorbed throughout the reactor and the lines to the mass spectrometer. The slower rate of removal of the Cp ring was indicated by the

Cp ring mass signal decreasing at a slower rate than the $NiCp_2$ mass signal after the N_2 purge was initiated, taking up to 20 min to be removed from the system as shown in Figure 2.10a. The slow decrease in the Cp ring signal was most likely due to Cp ring re-adsorption throughout the system and a fraction of the Cp rings thermally decomposing during the purge: similar to the organic group decomposition that was previously reported during the N_2 purge step of Pt ALD at 573 K.[39] The reactor was purged with N_2 to prevent chemical vapor deposition by the gas-phase reaction of H_2 with the residual $NiCp_2$ precursor.

In the second step of the reaction, H_2 was used to hydrogenate the organic ligands bound to the Ni, as shown in Scheme 2.2. Figure 2.10b indicates that the second step produced detectable amounts of a Cp ring and methane as the two main products, and H_2 broke through the powder bed approximately one minute after the dose. The detection of the Cp ring and CH_4 in the second half reaction indicates that Cp and C_xH_y species were present on the surface after the first half reaction, as indicated in Schemes 2.1 and 2.2. This reaction pathway differs from the typical ALD combustion pathway that occurs when O_2 is used as the second reactant.[27, 30] Hydrogen has been used as the second reactant for Pt ALD,[39] but not for Ni ALD.

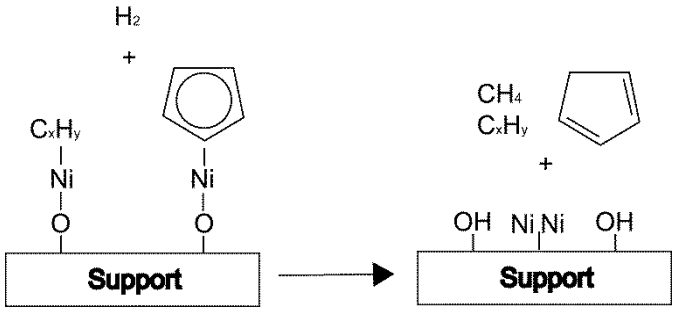

Scheme 2.2. Reaction scheme for second ALD half reaction in which H_2 reacts with surface species.

The H_2 hydrogenated the organic ligands, reduced the Ni to metallic Ni because the environment was H_2-rich at 573 K, and regenerated surface O-H. Upon removal of the Cp ligand

and reduction of the Ni-O bond, the Ni atoms presumably became mobile on the surface and agglomerated to form Ni nanoparticles, which are shown in the TEM images in Figures 2.2 and 2.3. This atom mobility and agglomeration is similar to the particle formation mechanism proposed for Pt ALD with $Me_3MeCpPt$ and H_2.[39] After the particles formed and the reactor was purged with N_2 again, the regenerated OH sites reacted in the next ALD cycle.

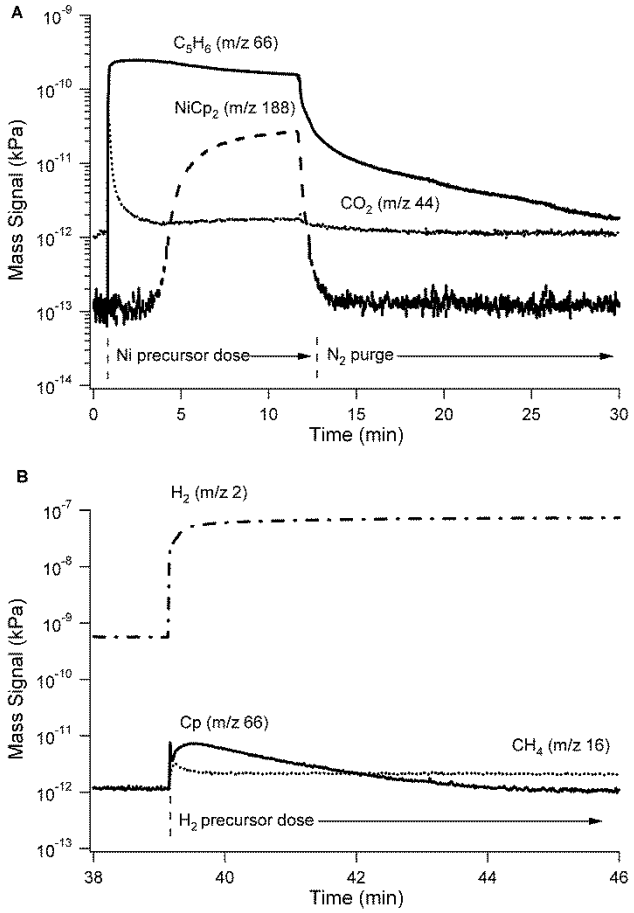

Figure 2.10 A) In-situ mass spectra of the first half-cycle $NiCp_2$ dose B) Second half reaction with H_2 gas (20% in Ar) dosed as the precursor

2.4.2. Catalyst Characterization

The weight percent of Ni for each sample is shown in Table 2.1. One ALD cycle formed a catalyst with 4.7 wt% Ni. The theoretical Ni loading for one cycle was calculated using Equation 2.1, which assumes one Ni atom bound to each hydroxyl on the Al_2O_3 surface:

$$L_{theoretical} = \frac{100 * MW_{Ni} * \rho_{OH} * SA_{Al2O3}}{A} \qquad (2.1)$$

where L is the theoretical weight loading of Ni for one ALD cycle, MW is the molecular weight of Ni, ρ_{OH} is the OH density on the Al_2O_3 surface, SA_{Al2O3} is the specific surface area of the Al_2O_3, and A is Avogadro's number. The hydroxyl surface density of the alumina nanospheres estimated by thermogravimetric analysis, was 12.6 OH/nm^2, which is similar to the value of 14 +/- 0.5 reported by an extensive IR-deuterium exchange study by Baumgarten *et al.*. [40] Using 12.6 OH/nm^2 and a measured BET surface area of 37.7 m^2/g in Equation 1 yield a theoretical weight loading of 4.63 wt%. Since this value is nearly identical to the measured weight loading, most of the OH groups likely reacted with $NiCp_2$ molecules during the first ALD cycle.[41] Subsequent ALD cycles had a lower growth rate per cycle, most likely because reactive hydroxyl sites were depleted on the support.

After each ALD cycle, the newly-deposited Ni atoms coalesced into approximately 3-nm particle sizes or diffused to existing particles. Although some of the initial surface sites were regenerated for subsequent ALD cycles, the deposited nanoparticles physically blocked a significant portion of the original sites. The percentage of Al_2O_3 surface area covered by Ni particles was estimated at approximately 18% for the 1-cycle sample by using the average particle diameter and weight loading to determine the cross-sectional area of all the particles deposited. In addition to Ni depositing at a lower rate per cycle, Figure 2.2 shows that the average particle size obtained from TEM images did not increase much as the number of ALD cycles increased on both the porous and nanosphere supports.

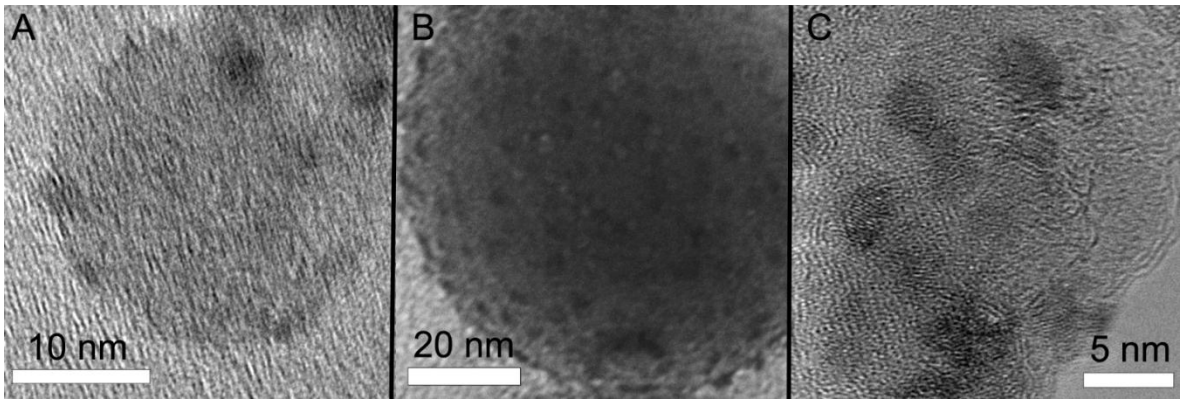

Figure 2.2. TEM and HRTEM images of Ni/Al_2O_3 catalysts prepared by 1 (A), 5 (B), and 15 (C) ALD cycles

The nanoparticles in the center of the HRTEM images appeared spherical, which would imply a particle height-to-diameter ratio of 1. The images near the nanosphere support edges, however, show that the particles were disc-like, with a height-to-diameter ratio of approximately 0.5. The surface area per gram of a disc-like particle is higher than that of a sphere of the same diameter, and the surface area can be adjusted with a shape correction factor α that is dependent on the height-to-diameter ratio of the particles.[42] Calculations that incorporated particle morphology (e.g., active surface area in Equation 2.2) were adjusted by a shape correction factor of 1.20.[42] A HRTEM scan of the porous Al_2O_3 support with Ni deposited by 15 ALD cycles (Fig. 3) showed that Ni deposited throughout the support. The average ALD nanoparticle sizes (2.4 – 3.3 nm) were comparable to the smallest alumina-supported Ni nanoparticles previously reported (2.9 nm for 2.3% Ni weight loading),[43] but the weight loadings of the ALD particles were 2 to 8 times higher. To our knowledge, these are the smallest Ni particles on alumina supports for Ni weight loadings of 4.7-16.5%.

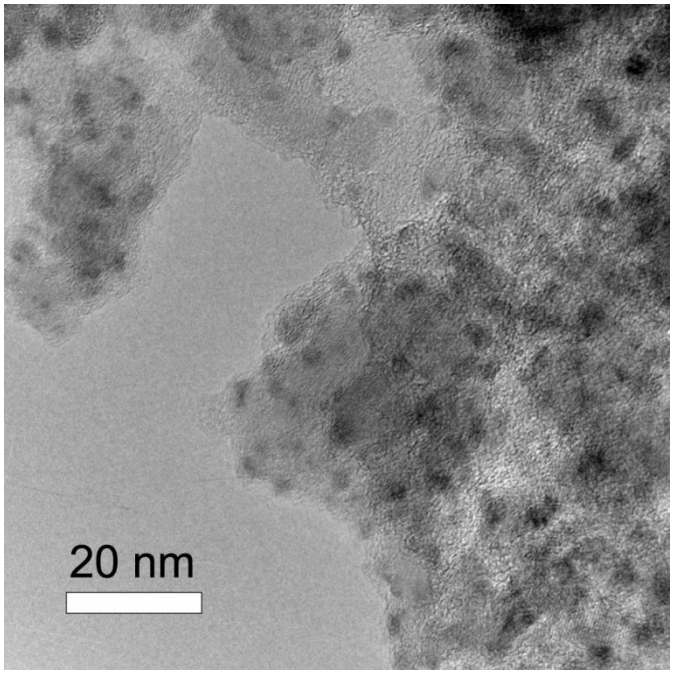

Figure 2.3 HRTEM image of Ni metal nanoparticles (dark spots on image ~ 3 nm in diameter) deposited via ALD using $NiCp_2$ and H_2 as the two precursors.

The active metal surface area (ASA) and dispersion of the ALD catalysts were calculated by using the measured particle size in Equations 2.2 and 2.3:

$$\text{ASA } [\text{m}^2/\text{g}] = \frac{L*f*\alpha}{100*\text{d}*\text{Z}} \qquad (2.2)$$

$$\text{Dispersion } = \frac{\text{ASA}*\text{FW}}{\text{N}*\text{A}*\text{L}} \qquad (2.3)$$

where d is the average crystallite diameter measured by TEM, L is the weight fraction metal loading, the quantity f/d is the surface area/volume ratio (for a sphere, the shape factor f=6), α is the shape correction factor to adjust for greater surface areas due to non-spherical particles (α=1.2), Z is the density of the metal, N is Avogadro's number, A is the metal surface area per atom (for Ni, A = 6.494$Å^2$/atom), and FW is the formula weight of Ni. Dispersion, ASA, and particle size values for the incipient wetness catalyst were calculated by using the number of surface sites determined from CO TPD and the weight loading in Equations 2.2 and 2.3. For each ALD catalyst, the calculated ASA shown in Table 2.1 was greater than the highest values

reported for alumina-supported Ni catalyst particles prepared by incipient wetness, impregnation or hydrazine reduction.[43-45]

Table 2.1. Catalyst characterization

Sample	Al_2O_3 Support	Ni Weight %	Particle size (TEM)[c] [nm]	Calculated Dispersion [%]	Calculated ASA [$m^2 \cdot g_{cat}^{-1}$]	Surface sites (CO TPD) [$\mu mol \cdot g_{cat}^{-1}$]
1 cycle Ni ALD	nanospheres	4.7	2.4 +/- 0.1	51 +/- 3	16 +/- 1	263
5 cycle Ni ALD	nanospheres	7.6	3.0 +/- 0.1	41 +/- 1	21 +/- 1	325
15 cycles Ni ALD	porous	16.7	3.3 +/- 0.1	37 +/- 1	41 +/- 1	446
incipient wetness [a]	porous	8.2	15	6.5	3.5	69
impregnation [b]	nanofibrous	10.2	-	3.6	2.4	93

[a] Particle size, dispersion, and ASA were calculated using the number of active sites determined from CO TPD in conjunction with Equations 2 – 3.
[b] Values are from ref. 44 and were measured via ICP-MS, chemisorption, and CO TPD
[c] Standard error shown for particle size. Particle size error was propagated through ASA and dispersion calculations.

The number of surface metal sites, listed in Table 2.1, was determined by integrating the amount of CO, CO_2, and CH_4 desorbed in the CO TPD. Calculating dispersion (or fractional exposure) via adsorbed CO can be misleading for nanoparticles with a large fraction of defects. Nickel can adsorb CO in different stoichiometries (varying between 0.55-3 CO molecules adsorbed per Ni atom).[46] For example, assuming an adsorption stoichiometry of one for the CO desorbed from the one-cycle ALD sample yields a dispersion of 0.33, which corresponds to a particle size of 3.7 nm. Assuming an adsorption stoichiometry of 0.55 yields a dispersion of 0.60 and a calculated particle size of 2.0 nm. The measured particle diameter from TEM lies in between these two values at 2.4 nm, so we reported the total amount of CO adsorbed without assuming an adsorption stoichiometry. The surface sites measured for the incipient wetness catalyst were in agreement with previously reported CO TPD integration values for a 10 wt% Ni/Al_2O_3 catalyst (prepared by impregnation), yielding 93 μmol/g.[44] The number of surface sites per gram of catalyst was five to ten times higher for the ALD catalysts than the 8 wt%

incipient wetness catalyst or similar impregnation catalysts.[44] The number of surface sites on the 7.57 wt% ALD catalyst was approximately five times higher than the 8 wt% incipient wetness catalyst. Even though the two catalysts are of similar weight loading, the particles deposited via ALD had a much higher fraction of Ni surface atoms.

Perhaps more significant than the increase in dispersion, CO TPD showed that desorption was different on the ALD catalysts, as shown in Figure 2.. Carbon monoxide desorbs from Ni catalysts in three peaks: 1) α_1 below 423 K corresponding to single-site adsorption and desorption of molecular CO, 2) β_1 at 423 – 623 K corresponding to associative desorption of C and O, and 3) β_2 from 623 - 723 K corresponding to associative desorption from step edge and kink sites.[44, 47-49] The ALD catalysts exhibited all three desorption regimes, but CO primarily desorbed in the β_1 and β_2 modes, as shown in Figure 2.. The likelihood of forming $Ni(CO)_4$ was relatively low since no low-temperature (< 348 K) CO peaks were detected. Previous CO TPD studies on Ni indicate that $Ni(CO)_4$ decomposes into CO around 323 - 348 K.[49] The ALD catalysts all had proportionally larger β_2 CO peaks than the incipient wetness catalyst. As expected, the peak areas were larger on a per gram basis because the higher dispersions and weight loadings provided much more surface area for CO to adsorb. Moreover, the ratio of β_2 to α_1 or β_1 peak areas increased with the number of ALD cycles, indicating the concentration of step or kink sites on the ALD catalyst surface increased as the number of cycles increased. Although this increase in step or kink site concentration seems counter-intuitive since coordination number decreases with particle size, the concentration of reactive steps has previously been shown to proceed through a maximum as particle size increases.[50, 51]

During CO TPD, CO_2 and CH_4 also formed, and the CO_2 desorption modes were primarily β_1 and β_2, with a small amount of α_1 desorption. Additionally, much more CO_2

desorbed in the β_2 mode for the ALD catalysts compared to both the 8 wt% incipient wetness catalyst and other previously reported supported Ni catalysts that primarily desorb CO_2 at 473 – 573 K.[44, 48] This CO_2 can result from: 1) the Boudard reaction: $2CO \rightarrow CO_2 + C_{surface}$ or 2) the water gas shift (WGS) reaction: $2CO + 2OH_{surface} \rightarrow 2CO_2 + H_2$, which uses surface OH of the alumina support. Tanksale and Lee suggested that CO_2 mainly forms by the WGS reaction on supported Ni, but the Boudard reaction also takes place and leaves trace amounts of C on the catalyst.[44, 49] The incipient wetness catalyst desorbed 81% of the products as CO_2, whereas only about 30% of the products desorbed as CO_2 for the ALD catalysts. The smaller percentage of CO_2 indicates that the OH groups necessary for the WGS formation of CO_2 were not as prevalent on the ALD catalysts, likely due to the Ni nanoparticles covering approximately 18 - 25% of the original alumina surface area (compared to 1% coverage for the incipient wetness catalyst).

Methane also formed during CO TPD at the same temperature as the β_2 CO_2 and H_2 desorption (see supplemental information), as shown in Fig. 4; surface carbon from the Boudard reaction was most likely methanated by H_2 from the WGS reaction. Much more CH_4 formed on the ALD catalysts hypothetically because more surface carbon formed from the Boudard reaction. This result agrees with DFT studies that indicate step edges in general are more favorable to cleave the π bonds of CO through dissociative adsorption,[3, 50] and Ni(211) step edges are more energetically favorable than Ni(111) sites to cleave C-C bonds and stabilize carbon atoms.[10, 52] The fraction of all gas desorbed in the β_2 regime on the ALD catalysts was approximately 0.75, which was three times higher than the fraction of β_2 desorption from the incipient wetness catalyst.

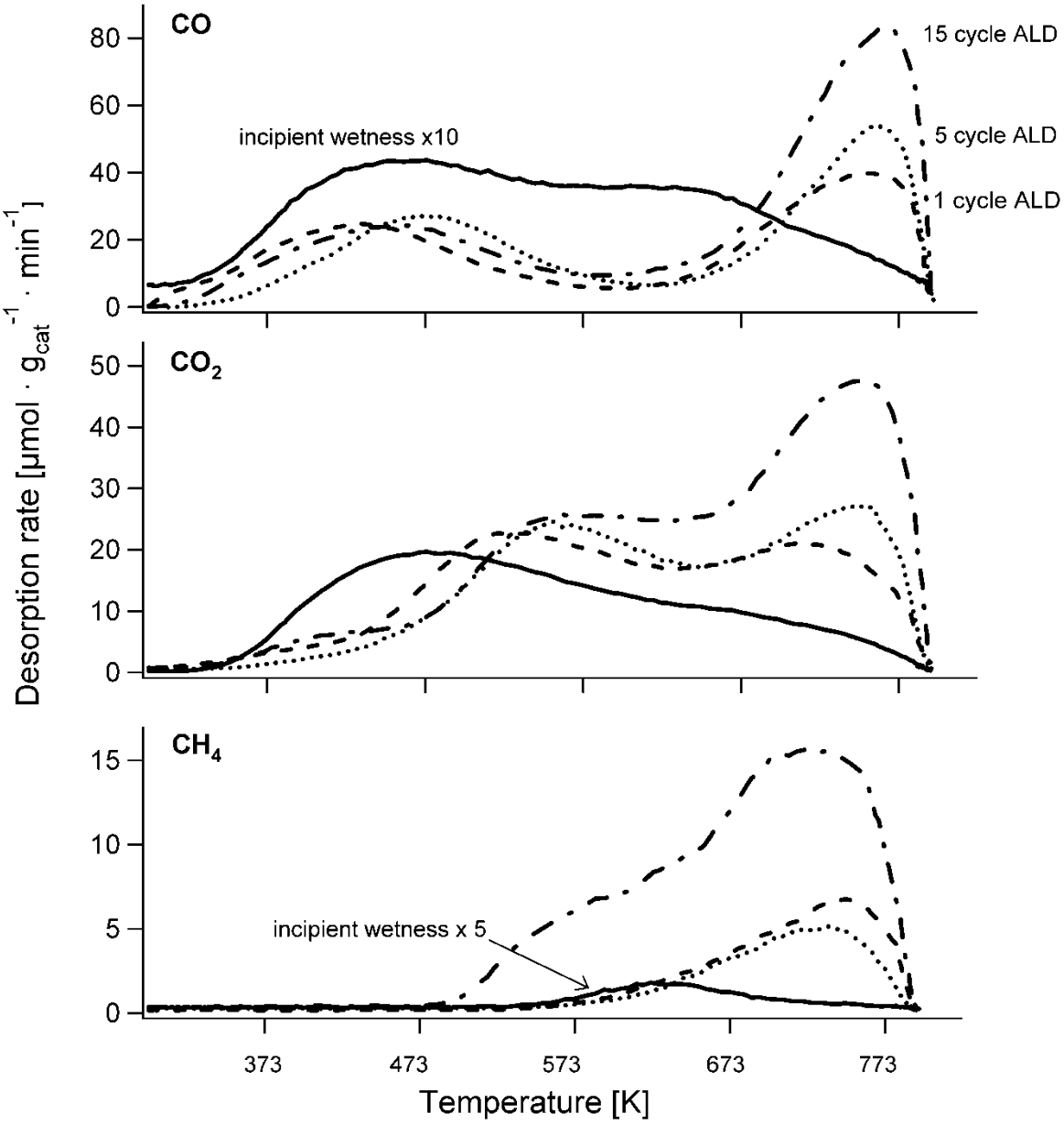

Figure 2.4. Carbon monoxide, CO_2, and CH_4 TPD spectra for CO adsorption on ALD and IW Ni/Al_2O_3 catalysts

2.4.3. Catalytic Performance

The four catalysts had similar hydrogenation TOFs (the TOF for the one-cycle ALD catalyst was slightly higher), but in contrast to the incipient wetness catalyst, the ALD catalysts also exhibited significant hydrogenolysis activity, as shown in Table 2.2. Turnover frequencies of both reactions did not vary for conversions from 10% to 70%, which were obtained by varying the amount of catalyst in the reactor. The hydrogenolysis rate had a maximum around 498 K for the 1- and 5-cycle ALD catalysts, but the 15-cycle ALD catalyst had a maximum at 523 K. At 523 K, the selectivity to hydrogenolysis was 10.6%; the maximum hydrogenolysis TOF was 0.39 s^{-1} and the hydrogenation TOF decreased to 3.3 s^{-1}. Hydrogenolysis was not due to a series reaction of hydrogenation followed by hydrogenolysis, because no hydrogenolysis products were detected on the 15-cycle catalyst under similar reaction conditions when propane was used as a feed. Changing the number of ALD cycles from 5 to 15 increased the hydrogenolysis rates by a factor of 5 at 498 K, and increased the hydrogenolysis rate by a factor of at least 9 at 523 K. Hydrogenolysis TOFs of the incipient wetness catalyst were similar to the ethane hydrogenolysis TOFs of approximately 5 x 10^{-3} s^{-1} at 498 K and 1.5 x 10^{-2} s^{-1} at 523 K reported by Goodman for Ni(100) single crystals.[53] The ALD catalysts' hydrogenolysis rates were similar to those reported by Coulter et al. on model Ni catalysts deposited on SiO_2 single crystals, with ethane hydrogenolysis TOFs reaching a maximum of 0.15 s^{-1} at 550 K for a particle size of 2.5 nm, then decreasing as the particles became larger or smaller.[54] The decrease in hydrogenolysis rate for the particles smaller than 3.3 nm is likely due to a combined effect of a decrease in ensembles of sufficient size for the hydrogenolysis reaction and a decrease in step edge concentration.[18, 55]

Table 2.2. Propylene hydrogenation and hydrogenolysis turnover frequencies (TOF) at 498 K and hydrogenolysis selectivity. Standard errors of reaction TOF are shown.

Sample	C_3H_6 Hydrogenation TOF [s^{-1}]	C_3H_6 Hydrogenolysis TOF [s^{-1}]	Selectivity [%]
1 cycle Ni ALD	7.1 +/- 0.8	0.04 +/- 0.002	0.6
5 cycle Ni ALD	4.6 +/- 0.1	0.03 +/- 0.01	0.7
15 cycle Ni ALD	4.2 +/- 0.3	0.20 +/- 0.06	4.4
8 wt% Ni IW	3.2 +/- 1.1	0.01 +/- 0.01	0.3

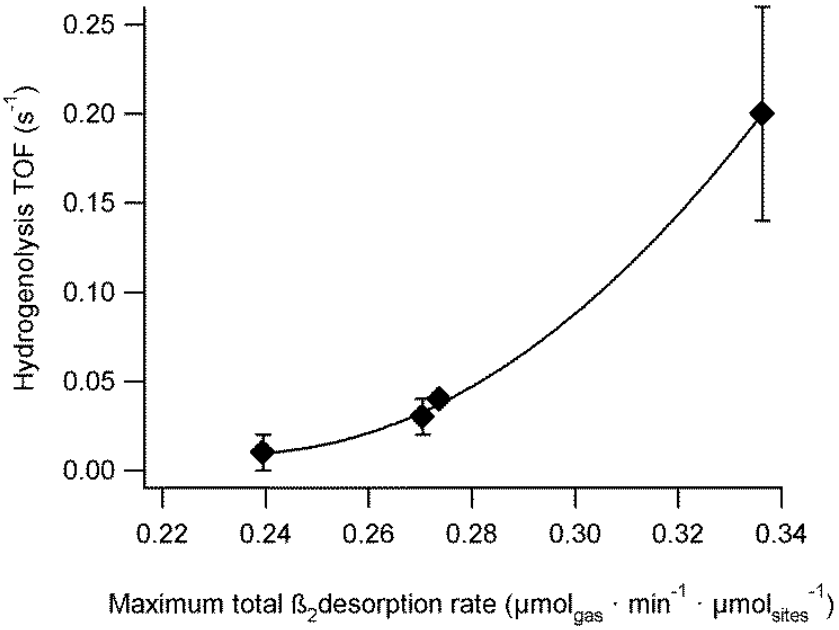

Figure 2.5. Hydrogenolysis TOF versus maximum β_2 desorption rate (normalized by number of surface sites). The line is a quadratic fit.

The surface structure and desorption behavior from CO TPD directly correlated with hydrogenolysis rates. The ability of the ALD catalysts to cleave the C-O bond and stabilize the carbon for hydrogen addition was a characteristic that was paralleled in the reactor studies in the cleavage of carbon bonds for propylene hydrogenolysis. The 15-cycle catalyst, which had the highest hydrogenolysis rate, desorbed the most CO and CO_2 in the β_2 desorption mode. The hydrogenolysis rate of the different catalysts increased with the total (CO, CO_2 and CH_4) β_2 maximum desorption rate determined from CO TPD (normalized by number of surface sites), as

shown in Figure 2.. A larger β_2 peak indicated more step edge or kink sites on the catalyst, which are more favorable for hydrogenolysis.[10] The 15-cycle ALD catalyst also desorbed the largest amount of CH_4, indicating the carbon and hydrogen formed CH_4 on the more prevalent step edges and kinks. Although the increase in particle size is minimal between the 1-cycle and the 15-cycle catalysts, the amount and coordination number of active sites can vary drastically when particle size changes only 0.5 nm in the 2- 5 nm size regime.[13, 56] Hydrogenolysis is identified as a structure sensitive reaction that can exhibit a maximum instead of continually increasing reaction rate as particle size decreases.[18, 50, 55, 57] This maximum arises from 1) the inability of step edges to exist on particles smaller than 2 nm and the decrease in sufficiently large ensembles as the particles become smaller, and 2) replacing step edges with higher-coordinated terraces as particles become sufficiently large.[17, 18, 50, 55]

2.5. Conclusions

Atomic layer deposition formed Ni nanoparticles on Al_2O_3 supports when H_2 and $NiCp_2$ were used as precursors. As the number of ALD cycles increased, the particle size and number of particles increased, but the mass of Ni deposited per cycle decreased. The dispersion of the ALD catalysts was higher than the incipient wetness catalyst used for comparison and similar to the highest values reported for supported Ni catalysts.

Carbon monoxide TPD indicated different desorption mode distributions for ALD catalysts (compared to incipient wetness catalyst), suggesting that the surface structures of the ALD nanoparticles are different from the larger incipient wetness Ni particles. The difference in surface structure, known to be more favorable for hydrogenolysis, resulted in hydrogenolysis at 498 K for the three ALD catalysts and 11% hydrogenolysis selectivity for the 15 cycle ALD catalyst at 523 K, whereas the incipient wetness catalyst had minimal hydrogenolysis selectivity.

The carbon double bond most likely cleaved on step edges and kinks, which TPD indicated were more prevalent for the catalysts with the highest hydrogenolysis activity. The ability to vary particle size and nanostructure by changing the number of ALD cycles allows for facile preparation of supported nanoscale catalysts. Not only does ALD address many of the challenges associated with commercializing nanoscale catalyst synthesis, but utilization of ALD for catalyst fabrication may also aid other applications where specific particle sizes or structures are required for activity or selectivity.

Acknowledgments

The work was supported through the National Science Foundation Graduate Research Fellowship Program and NSF Grant CBET 1067800. The authors thank Fred Luizer in the University of Colorado's Laboratory of Environmental and Geological Studies (LEGS) for conducting ICP-MS analysis. The authors also thank the MIT Shared Experimental Facility for the use of their HRTEM, and the MCDB Bio3d Electron Microscopy center for the use of TEM microscopes and sample preparation equipment. Kelly Anderson and Jake Carrier were also extremely helpful in running the reactors for ALD synthesis, TPD experiments, and catalytic studies.

2.6. References

[1] M. Neurock, Journal of Catalysis 216 (2003) 73-88.
[2] J.K. Nørskov, T. Bligaard, A. Logadottir, S. Bahn, L.B. Hansen, M. Bollinger, H. Bengaard, B. Hammer, Z. Sljivancanin, M. Mavrikakis, Y. Xu, S. Dahl, C.J.H. Jacobsen, Journal of Catalysis 209 (2002) 275-278.
[3] B. Hammer, J.K. Nørskov, H.K. Bruce C. Gates, Theoretical surface science and catalysis - calculations and concepts, in: Advances in Catalysis, Academic Press, 2000, pp. 71-129.
[4] M.T. Schaal, A.C. Pickerell, C.T. Williams, J.R. Monnier, Journal of Catalysis 254 (2008) 131-143.
[5] A.S. Loh, S.W. Davis, J.W. Medlin, Journal of the American Chemical Society 130 (2008) 5507-5514.
[6] M.T. Schaal, M.P. Hyman, M. Rangan, S. Ma, C.T. Williams, J.R. Monnier, J.W. Medlin, Surface Science 603 (2009) 690-696.

[7] E. Nikolla, J. Schwank, S. Linic, Journal of the American Chemical Society 131 (2009) 2747-2754.
[8] S.H. Alfons M. Molenbroek, Henrik Topsoe, Bjerne S. Clausen, Topics in Catalysis 52 (2009) 1303-1311.
[9] S. Alayoglu, A.U. Nilekar, M. Mavrikakis, B. Eichhorn, Nat Mater 7 (2008) 333-338.
[10] R.T. Vang, K. Honkala, S. Dahl, E.K. Vestergaard, J. Schnadt, E. Lægsgaard, B.S. Clausen, J.K. Nørskov, F. Besenbacher, Surface Science 600 (2006) 66-77.
[11] F. Abild-Pedersen, J. Greeley, J. Nørskov, Catalysis Letters 105 (2005) 9-13.
[12] Y. Li, G.A. Somorjai, Nano Letters 10 (2010) 2289-2295.
[13] R.V. Hardeveld, F. Hartog, Advances in Catalysis 22 (1972) 75-110.
[14] E.L. Hu, S.M. Davis, R. Davis, E. Scher, Applications: Catalysis by Nanostructured Materials: Nanotechnology Research Directions for Societal Needs in 2020, in, Springer Netherlands, 2011, pp. 445-466.
[15] M. Haruta, Catalysis Today 36 (1997) 153-166.
[16] A.T. Bell, Science 299 (2003) 1688-1691.
[17] J.M. Dartigues, A. Chambellan, F.G. Gault, Journal of the American Chemical Society 98 (1976) 856-857.
[18] G.C. Bond, Surface Science 156, Part 2 (1985) 966-981.
[19] J.D. Aiken Iii, R.G. Finke, Journal of Molecular Catalysis A: Chemical 145 (1999) 1-44.
[20] M. Gharibi, F.T. Zangeneh, F. Yaripour, S. Sahebdelfar, Applied Catalysis A: General 443-444 (2012) 8-26.
[21] F. Bozon-Verduraz, F. Fiévet, J.-Y. Piquemal, R. Brayner, K. El Kabouss, Y. Soumare, G. Viau, G. Shafeev, Brazilian Journal of Physics 39 (2009) 134-140.
[22] D.M. King, J.A. Spencer Ii, X. Liang, L.F. Hakim, A.W. Weimer, Surface and Coatings Technology 201 (2007) 9163-9171.
[23] S.M. George, Polymer 1550 (2012) 125.
[24] Y. Lei, B. Liu, J. Lu, R.J. Lobo-Lapidus, T. Wu, H. Feng, X. Xia, A.U. Mane, J.A. Libera, J.P. Greeley, J.T. Miller, J.W. Elam, Chemistry of Materials 24 (2012) 3525-3533.
[25] X. Liang, L. Lyon, Y.-B. Jiang, A. Weimer, Journal of Nanoparticle Research 14 (2012) 1-12.
[26] J. Li, X. Liang, D.M. King, Y.-B. Jiang, A.W. Weimer, Applied Catalysis B: Environmental 97 (2010) 220-226.
[27] S.T. Christensen, H. Feng, J.L. Libera, N. Guo, J.T. Miller, P.C. Stair, J.W. Elam, Nano Letters 10 (2010) 3047-3051.
[28] X. Liang, J. Li, M. Yu, C.N. McMurray, J.L. Falconer, A.W. Weimer, ACS Catalysis 1 (2011) 1162-1165.
[29] J. Lu, B. Fu, M.C. Kung, G. Xiao, J.W. Elam, H.H. Kung, P.C. Stair, Science 335 (2012) 1205-1208.
[30] W. Kessels, H. Knoops, S. Dielissen, A. Mackus, M. van de Sanden, Applied Physics Letters 95 (2009) 013114-013114-013113.
[31] J. Bachmann, A. Zolotaryov, O. Albrecht, S. Goetze, A. Berger, D. Hesse, D. Novikov, K. Nielsch, Chemical Vapor Deposition 17 (2011) 177-180.
[32] H.L. Lu, G. Scarel, C. Wiemer, M. Perego, S. Spiga, M. Fanciulli, G. Pavia, Journal of The Electrochemical Society 155 (2008) H807-H811.
[33] J.R. Scheffe, M.D. Allendorf, E.N. Coker, B.W. Jacobs, A.H. McDaniel, A.W. Weimer, Chemistry of Materials 23 (2011) 2030-2038.

[34] J.R. Scheffe, A. Francés, D.M. King, X. Liang, B.A. Branch, A.S. Cavanagh, S.M. George, A.W. Weimer, Thin Solid Films 517 (2009) 1874-1879.
[35] G.A. Ten Eyck, S. Pimanpang, H. Bakhru, T.M. Lu, G.C. Wang, Chemical Vapor Deposition 12 (2006) 290-294.
[36] B.S. Lim, A. Rahtu, R.G. Gordon, Nat Mater 2 (2003) 749-754.
[37] M.P. Rigney, E.F. Funkenbusch, P.W. Carr, Journal of Chromatography A 499 (1990) 291-304.
[38] J.B. Peri, R.B. Hannan, The Journal of Physical Chemistry 64 (1960) 1526-1530.
[39] W. Setthapun, W.D. Williams, S.M. Kim, H. Feng, J.W. Elam, F.A. Rabuffetti, K.R. Poeppelmeier, P.C. Stair, E.A. Stach, F.H. Ribeiro, J.T. Miller, C.L. Marshall, The Journal of Physical Chemistry C 114 (2010) 9758-9771.
[40] E. Baumgarten, R. Wagner, C. Lentes-Wagner, Fresenius' Zeitschrift für analytische Chemie 334 (1989) 246-251.
[41] Y. Chen, L. Zhang, Catalysis Letters 12 (1992) 51-62.
[42] W. Qi, M. Wang, Q. Liu, Journal of Materials Science 40 (2005) 2737-2739.
[43] D. Duprez, M.C. DeMicheli, P. Marecot, J. Barbier, O.A. Ferretti, E.N. Ponzi, Journal of Catalysis 124 (1990) 324-335.
[44] A. Tanksale, J.N. Beltramini, J.A. Dumesic, G.Q. Lu, Journal of Catalysis 258 (2008) 366-377.
[45] A.G. Boudjahem, S. Monteverdi, M. Mercy, M.M. Bettahar, Journal of Catalysis 221 (2004) 325-334.
[46] C.H. Bartholomew, R.B. Pannell, Journal of Catalysis 65 (1980) 390-401.
[47] W. Erley, H. Wagner, Surface Science 74 (1978) 333-341.
[48] J. Zieliński, Journal of Molecular Catalysis 79 (1993) 187-198.
[49] P.I. Lee, J.A. Schwarz, J.C. Heydweiller, Chemical Engineering Science 40 (1985) 509-519.
[50] R.A. Van Santen, Accounts of Chemical Research 42 (2008) 57-66.
[51] M. Mavrikakis, P. Stoltze, J.K. Nørskov, Catalysis Letters 64 (2000) 101-106.
[52] H. Bengaard, J.K. Nørskov, J. Sehested, B.S. Clausen, L.P. Nielsen, A.M. Molenbroek, J.R. Rostrup-Nielsen, Journal of Catalysis 209 (2002) 365-384.
[53] D.W. Goodman, Surface Science 123 (1982) L679-L685.
[54] K. Coulter, X. Xu, D.W. Goodman, The Journal of Physical Chemistry 98 (1994) 1245-1249.
[55] G.A. Martin, Journal of Catalysis 60 (1979) 345-355.
[56] O.L. Pérez, D. Romeu, M.J. Yacamán, Applications of Surface Science 13 (1982) 402-413.
[57] G.C. Bond, Chemical Society Reviews 20 (1991) 441-475.

2.7 Chapter 2 Appendix – Additional HRTEM images of Ni ALD particles

After the initial Ni ALD work was finished, we began collaborating with the Precision Imaging Facility (PIF) at NIST in Boulder to image some of the particles that were inherently difficult to image on traditional TEMs found on CU's campus. Their work is featured in subsequent chapters, but they also managed to image some of the Ni ALD particles from this chapter. They were given some of our bimetallic samples (featured in Chapter 4) that were prepared by depositing Pt ALD on the same 1-cycle Ni ALD catalysts supported on non-porous alumina spheres from Chapter 2. In some regions they found (through EDX) that there was no Pt, and only Ni particles. Included in this appendix are two of the HRTEM images of these Ni particles, indicated by the ~2.5 nm particles exhibiting lattice fringes in Figures 2.A1 and 2.A2.

Analysis of the lattice fringes by ImageJ (by doing a line measurement over the lattice and dividing by the total number of lattices to get the d-spacing) yielded values for the lattice constant a = 0.362 nm, which is close to Ni (111) 0.352 nm, but likely encompassed errors from where exactly the line was drawn across the fringes in ImageJ. When this method was applied by Ann Chiaramonti at NIST, she got a value for a = 0.356 nm. Alternatively, they also did a fast Fourier transform (FFT) on the images, which yielded a d-spacing of .2 nm that corresponds to a lattice parameter for Ni(111) of a = 0.346 nm.

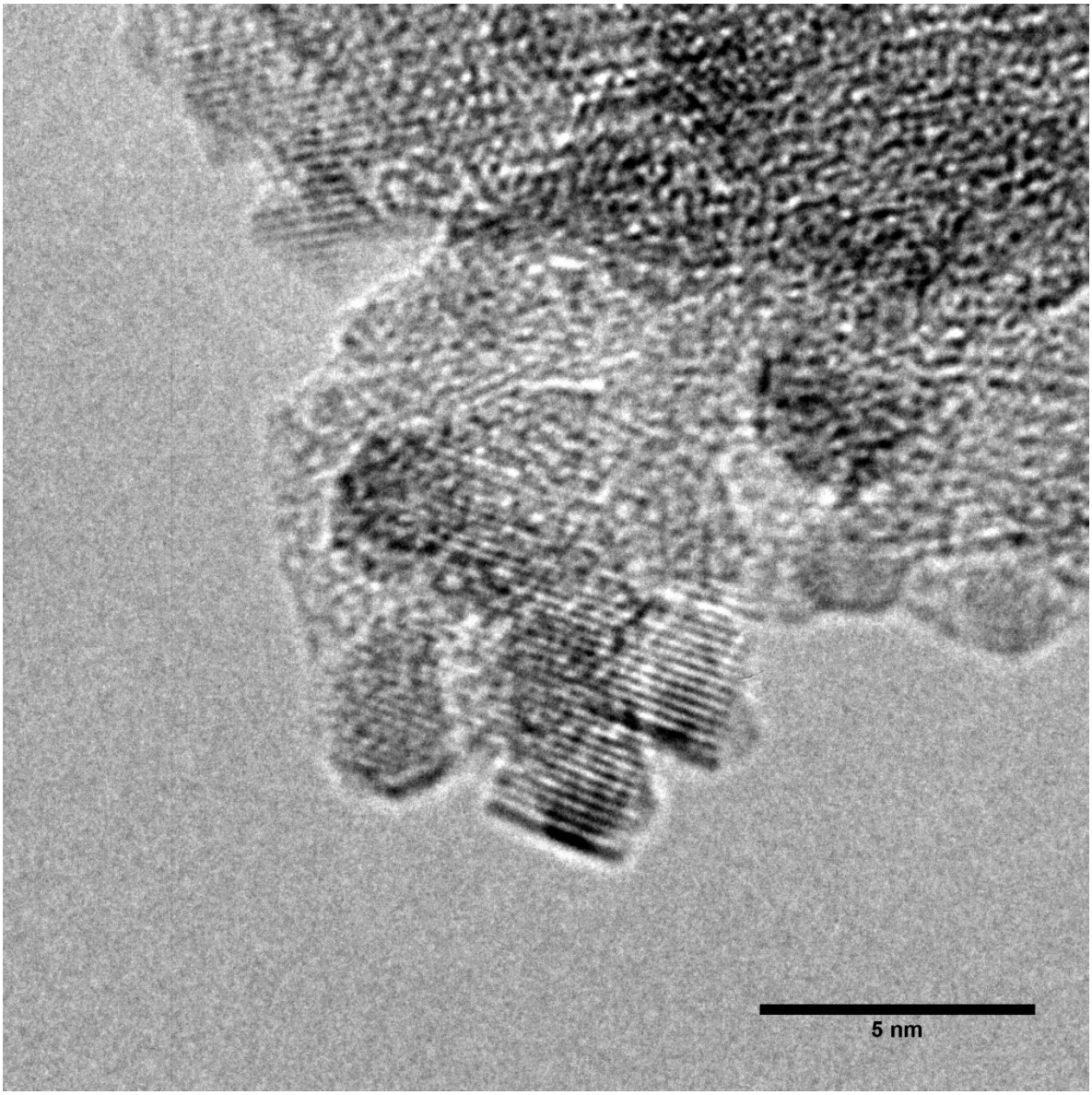

Figure 2.A1. Nickel ALD catalyst particles imaged by NISTs HRTEM at 500,000x magnification.

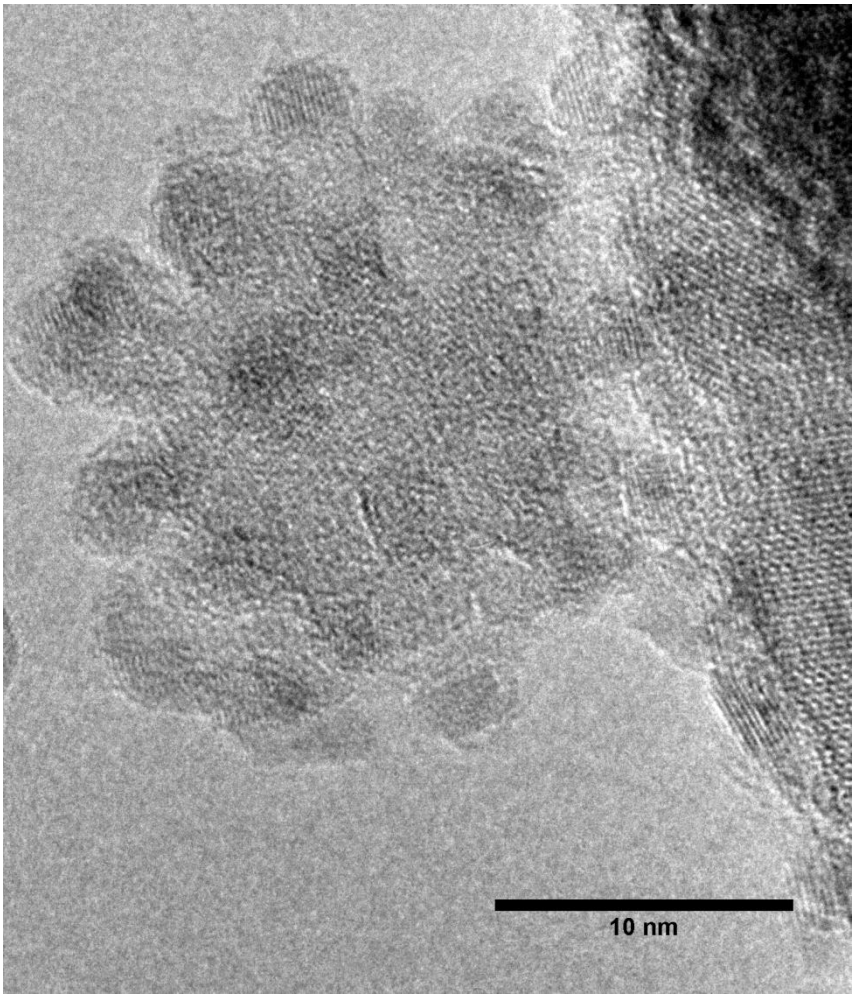

Figure 2.A2. Nickel ALD particles imaged by NIST's HRTEM at 250,000x magnification.

Chapter 3: Controlling nanoscale properties of supported platinum catalysts through atomic layer deposition

3.1 Abstract

Platinum nanoparticles were grown on alumina by atomic layer deposition using either H_2 or O_2 as the second half-reaction precursor. Particle diameters could be tuned between ~1 and 2 nm by using different chemistries and by changing the number of ALD cycles. Temperature-programmed desorption (TPD) of CO and diffuse reflectance infrared Fourier transform spectroscopy (DRIFTS) for adsorbed CO were used to characterize site distributions on the nanoparticles. As expected, smaller nanoparticles had sites with lower coordination numbers. The two chemistries had different deposition mechanisms, most likely due to differences in reaction sites of either existing Pt particles or the surface hydroxyl groups, which were monitored via *in-situ* FTIR during Pt ALD. The catalysts were evaluated for oxidative dehydrogenation of propane to propylene. The smallest particles (synthesized by 1 cycle of Pt ALD with H_2) had a C_3H_6 selectivity of 37% at 14% conversion, whereas the selectivity was less than 1% for larger (3.6 nm) commercial Pt particles at 9% conversion.

3.2 Introduction

The catalysis field has been advancing towards precise control of nanometer and sub-nanometer features in catalytic materials. These advances were made possible by new synthesis methods, better analytical techniques to probe ultra-small features, and greater understanding of fundamental catalytic principles at the nanoscale through theoretical investigations.[1-3] One example of a highly sought-after reaction is oxidative dehydrogenation (ODH) of alkanes to alkenes, which can benefit from advances in nanostructured catalysts.[4] Oxidative

dehydrogenation of propane (ODHP) to propylene is of particular interest. The global demand for propylene is expected to increase by more than 20 billion kg by 2017, with global sales currently exceeding $90 billion US.[5] Propylene is primarily produced in steam crackers, with a smaller fraction produced in fluid catalytic cracking (FCC) units, and an even smaller fraction produced by catalytic dehydration.[6] The cracking processes are highly endothermic, require regeneration of the catalysts due to coking, and produce larger fractions of ethylene than propylene.[7] Oxidative dehydrogenation, in contrast, can be operated at temperatures below 773 K and is exothermal instead of the highly endothermic catalytic non-oxidative dehydrogenation that must typically be run at temperatures above 1073 K.[7] Currently, ODHP catalysts do not have high enough yields to cause propylene manufacturers to adopt ODHP as a viable alternative over traditional cracking technologies.

Oxidative dehydrogenation is known as a Type III structure sensitive reaction; i.e., the turnover frequency increases as the particle size decreases.[8, 9] Vajda *et al.* used DFT to elucidate why this reaction became more favorable on Pt clusters of 4 to 8 atoms.[9] Clusters of this size have atoms with a coordination number (CN) of3 to 4, and their study showed that these atoms have a lower barrier for breaking a C-H bond than for breaking a C-C bond to form CO or CO_2. Supported Pt catalysts with larger crystallite sizes and Pt (111) surfaces have shown minimal selectivity to propylene and instead catalyze combustion, favoring C-C bond breaking over C-H bond breaking.[10] However, size-selected Pt clusters of 8 to 10 atoms have achieved propylene selectivities greater than 60%, but those catalysts were highly idealized and prepared with a non-scalable technique requiring a continuous cluster beam as the Pt source.[9]

Atomic layer deposition has been used in the last decade because of its ability in some applications to prepare relatively-small Pt nanoclusters without succumbing to the disadvantages

of liquid-phase synthesis techniques. Although liquid-phase catalyst preparation can achieve more precise control over size and shape[11, 12], the solvents are often hazardous, and the synthesis requires further steps to purify the product, cleave organic capping agents, and deposit the separately-prepared particles on a support.[11, 13, 14] Aaltonen *et al*. pioneered the use of trimethyl(methylcyclopentadienyl)platinum ($Me_3(MeCp)Pt$) and O_2 to deposit Pt films using hundreds of Pt ALD cycles.[15] Since that time, this oxidative ALD process has been used to deposit Pt nanoparticles using a range of number of cycles and on various metal oxide supports.[16-19] *In-situ* FTIR of gas-phase ALD products and EXAFTS/XANES techniques have been used to gain a better understanding of the ALD mechanism.[19, 20] The generally-accepted mechanism for Pt ALD, once a sufficient amount of Pt is deposited, is as follows for the O_2 chemistry[20]:

The first half reaction, dosing the Pt precursor:

$$2(MeCp)PtMe_3(g) + 3\ O(ads) \rightarrow 2(MeCp)PtMe_2(ads) + CH_4(g) + CO_2(g) + H_2O(g)$$

The second half-reaction, using O_2:

$$2(MeCp)PtMe_2(ads) + 24\ O_2(g) \rightarrow 2\ Pt(s) + 3\ O(ads) + 16\ CO_2(g) + 13\ H_2O(g)$$

These reaction mechanisms are valid once Pt particles or layers are already deposited. However, in the first few cycles, the active sites for deposition on metal oxides are OH groups. As the number of ALD cycles increases, the Pt coverage increases until the active sites for deposition are exclusively Pt-O.[19] Alternatively, H_2 can be used as the second half-reaction precursor instead of O_2 to hydrogenate the organic groups of the Pt precursor. No Pt-O species are formed when H_2-based ALD is used, and the active sites are the OH groups on the surface of the metal oxide.[19]

The focus on creating ultra-small Pt nanoparticles or nanoclusters has encouraged several theoretical studies that investigated the mechanisms of single Pt and Pd adatom behavior on metal oxide support surfaces. Diffusion via site-to-site transitions have been studied on gamma alumina for both Pt and Pd atoms through DFT.[21, 22] Interestingly, hydroxyl groups adsorbed on Al_2O_3 decrease the adsorption strength of Pt and Pd atoms on the support, but drastically increase the diffusion barriers of metal atoms on these surfaces. For Pd atom diffusion, Valero *et al.* showed that a hydroxylated surface caused the low-energy diffusion trajectory barrier to increase by as much as 74 kJ/mol.[22] These OH groups may play a significant role in the Pt ALD mechanism since they are proposed as the active site during H_2 ALD but not during most steps of O_2 ALD.[19]

In the present study, the effect of the second half-reaction chemistry on particle size was investigated with one or five ALD cycles. Changing the number of cycles and reaction chemistry varied particle size between 1 and 2.5 nm. The difference between H_2 and O_2 ALD during the deposition of Pt on alumina was investigated by *in-situ* FTIR characterization of the surface hydroxyl groups. The surface structures of these catalysts were characterized by CO TPD and CO DRIFTs, with an emphasis on characterizing low-coordinated atoms. Finally, these catalysts were evaluated for activity and selectivity for ODHP.

3.3 Experimental Methods

3.3.1 ALD synthesis

Platinum particles were synthesized on alumina supports by ALD using either a stainless steel fluidized bed reactor (FBR) [23, 24] (for 2-g batches) or a quartz tube FBR (6-mm inner diameter) with a quartz glass frit of 40-μm pore size that supported the powder bed for smaller batches. The alumina powder was fluidized in the quartz reactor at approximately 0.25-Pa

pressure with He carrier gas flow rates of 5 to 20 sccm. The alumina was then dried for 2 h under vacuum at 393 K before Pt was deposited by ALD in the quartz FBR. Both porous alumina (Albermarle MARTOXID AN/I gamma alumina) and nonporous nanosphere alumina (Aldrich 544833 gamma alumina) were used as supports. Platinum was deposited at 448 K, which is much lower than the 573 K temperature typically used for Pt ALD with $Me_3(MeCp)Pt$ and O_2.[17, 19, 25] In this work, either H_2 or O_2 was used as the second reagent for Pt ALD.

3.3.2 Catalyst Characterization

The catalysts were characterized by TPD in a quartz tube reactor (6.35-mm inner diameter) at ramp rates of 20 K/min, and the reactor effluent was analyzed with an SRS RGA 200 mass spectrometer. For CO TPD, the catalysts were reduced for 2 h at 523 K, purged with inert, flashed to 923 K to desorb residual H_2 and H_2O, cooled to room temperature, dosed with CO (100 sccm 20% CO in Ar) for 10 min, and then purged with Ar before ramping the temperature.

Particle size estimates were obtained using Image J software to analyze images from an FEI Tecnai 12 - Spirit Biotwin TEM and a Phillips CM-100 TEM. For even higher resolution imaging, bright field images were taken by high-resolution TEM and dark field images were taken by high angle annular dark field scanning tunneling electron microscopy (HAADF STEM) at NIST's Precision Imaging Facility (PIF) on a JEOL ARM200F microscope with a Shottky field emission gun. Samples were electrostatically adhered to copper grids with a lacey carbon over-layer (Ted-Pella 01895 Lacey Carbon Film grids) to avoid effects of solvents from dropcasting. Samples prepared for imaging purposes were synthesized on the nonporous nanosphere alumina so that the metal catalyst particles were on the surface of the spheres and visible by TEM. The weight loadings of each sample were determined by inductively coupled

plasma mass spectroscopy (ICP-MS). The number of active sites was measured with a Quantachrome AS-1 Autosorb. The catalysts were reduced at 523 K in pure H_2 for 2 h before measuring the H_2 uptake.

A Nicolet 6700 FTIR spectrometer was used to measure spectra at 4 cm^{-1} resolution by transmission IR for *in-situ* ALD experiments and diffuse reflectance infrared Fourier transform spectroscopy (DRIFTS) for CO adsorption experiments. For the *in*-situ ALD measurements, alumina nanopowder was mixed in a 1:2 ratio with KBr and pressed into a tungsten grid with a hydraulic press at 2000 kg pressure. The sample was loaded into a vacuum chamber with IR-transparent CaF_2 windows; this chamber is described in more detail elsewhere.[26] A thermocouple was placed within 2 mm of the tungsten grid to monitor the temperature of the grid. The chamber was evacuated and heated to approximately 400 K and scanned before the first Pt ALD dose. The Pt, O_2, and H_2 static doses were done for 30 min each; longer dose durations showed no discernable differences. Between each dose the chamber was evacuated for at least 30 min to remove residual precursor molecules. A blank grid loaded with KBr was coated by 3 cycles of Pt ALD, and the KBr turned black, just as in the experiments with alumina, but with the KBr-only sample, no distinctive IR features were observed at any point during the deposition. The KBr's contribution to the observed FTIR spectra was negligible because the surface area of the KBr was 0.23 m^2/g compared to 35 m^2/g for the alumina support.

The CO DRIFTS experiments were performed on a bed of catalyst powder using a closed cell attachment (Harrick). Each sample was oxidized for 2 h at 573 K then reduced at 473 K for 2 h to ensure metallic Pt. The catalysts were then loaded into the chamber and degassed under vacuum for several hours to desorb water from the alumina supports. Carbon monoxide was dosed at room temperature at sequentially higher CO pressures until no further changes in IR

spectra were detected. For the temperature-ramp DRIFTS study, the sample was initially saturated with CO (at a CO pressure of ~185 kPa), and then the chamber was evacuated and held under vacuum for all CO DRIFTS measurements. The sample was heated from room temperature to 600 K under vacuum in approximately 50 K increments, allowing at least 1 h equilibration time before the spectra was measured for a given temperature.

3.3.3 Catalyst Evaluation

The Pt catalysts were evaluated for their activity and selectivity for ODHP. Prior to exposure to reaction conditions, the catalysts were oxidized at 600 K for 10 min in a 20% O_2 stream at 100 sccm. Then they were reduced in 100 sccm of 20% H_2 for 1 h at 523 K. For most catalytic testing, approximately 100 mg of catalyst was used, resulting in a nearly constant space velocity of 28 s^{-1}, and full consumption of the O_2. Reactants flowed through the same packed-bed, quartz tube reactor described above for the TPD studies, and the reactor effluent was measured by a SRI GC 8610c with a Haysep-D packed column. Flow rates for ODHP selectivity studies were 12 sccm C_3H_8, 6 sccm O_2, and 182 sccm Ar. A 5 wt% commercial Pt/Al_2O_3 catalyst (Sigma) was tested for ODHP activity as a basis of comparison to larger, more Pt(111)-terminated Pt particles. Turnover frequencies (TOF) were also measured by running the reaction at less than full O_2 conversion (~50 – 75% conversion) by using less catalyst (typically 2 mg or less), and diluting the catalyst bed with the same alumina to 100 mg total bed weight. The same concentration of reactants was used to determine TOFs.

3.4 Results and Discussion

3.4.1 Effect of second precursor and number of cycles on particle size

For one Pt ALD cycle at 448 K on the alumina supports, the Pt particles were smaller when H_2 rather than O_2 was used as the second reagent. Images and size distributions are shown in Figure 3.1. Even though the first Pt ALD half-cycle on alumina is exactly the same, using H_2 in the second half cycle produced an average Pt cluster size (measured by TEM) of 1.1 +/- 0.2 nm, whereas using O_2 produced 1.4 +/- 0.2 nm clusters. The difference in average particle size was statistically significant according to a two sample t-test at $\alpha = 0.05$. These particle sizes are similar to those measured by EXAFS by Setthapun *et al.* for 1-cycle Pt ALD on spherical alumina with O_2 and H_2, although they used deposition temperatures of 573 K for the O_2 reaction and 473 K for the H_2 reaction. Each catalyst had essentially the same weight loading of approximately 1.0 wt% (+/- 0.2 %) because the first ALD half-cycle, which deposits the platinum precursor, was the same for the two preparations. The number of active sites per gram of metal measured by chemisorption was larger for the H_2-synthesized particles than O_2-synthesized particles. The average particle sizes calculated from chemisorption, listed in Table 1, were smaller than those obtained from TEM, which may not be able to detect sub-nm particles. Additionally, Pt atoms can adsorb more than one H per active site when the average CN of the cluster drops below 6.[27]

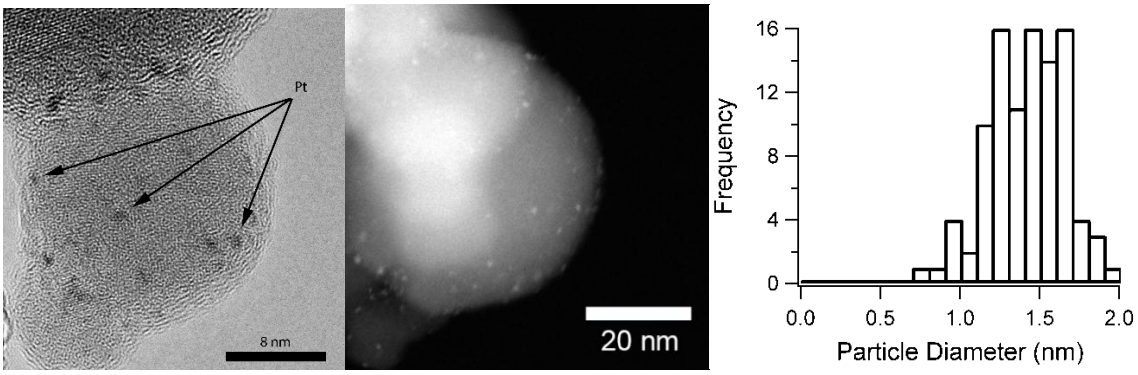

Figure 3.1A. From left to right, HRTEM, HAADF STEM, and size distribution of Pt nanoparticles synthesized by one cycle of Pt ALD with O_2 on spherical nano-alumina support.

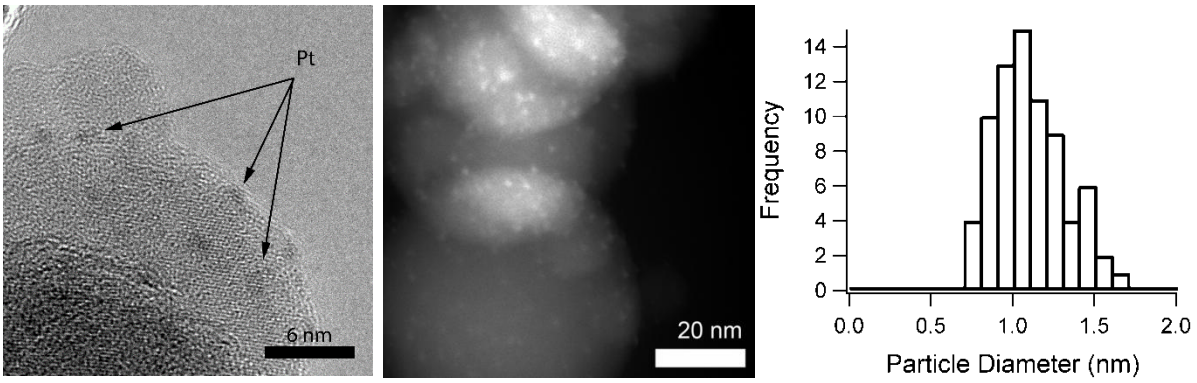

Figure 3.1B. From left to right: HRTEM, HAADF STEM, and size distribution of 1-cycle Pt ALD nanoparticles synthesized with H_2 on spherical nano-alumina support.

We also prepared catalysts with higher Pt weight loading using five ALD cycles. As shown in Figure 3.2, using H_2 as the second precursor again resulted in smaller particle sizes (1.7 +/- 0.4 nm) compared to using O_2 (2.4 +/- 0.5 nm).

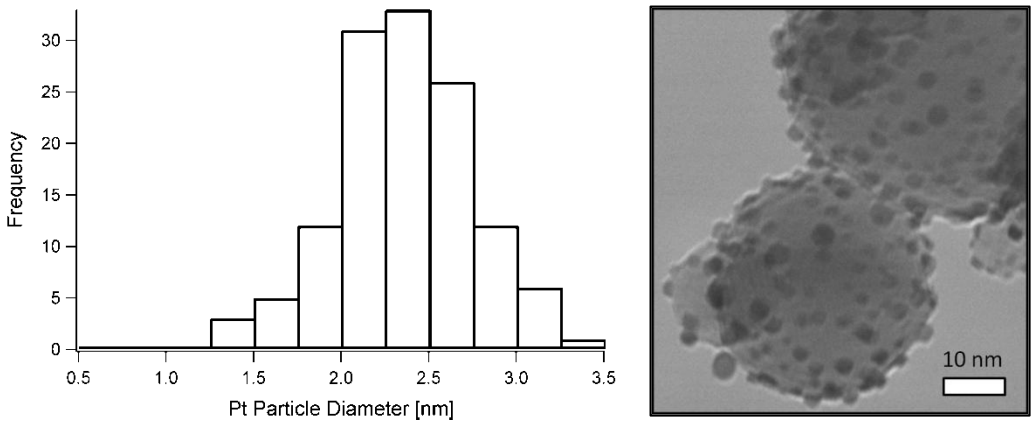

Figure 3.2A. Pt ALD particle size distribution and TEM images of 5 cycles O_2 Pt ALD

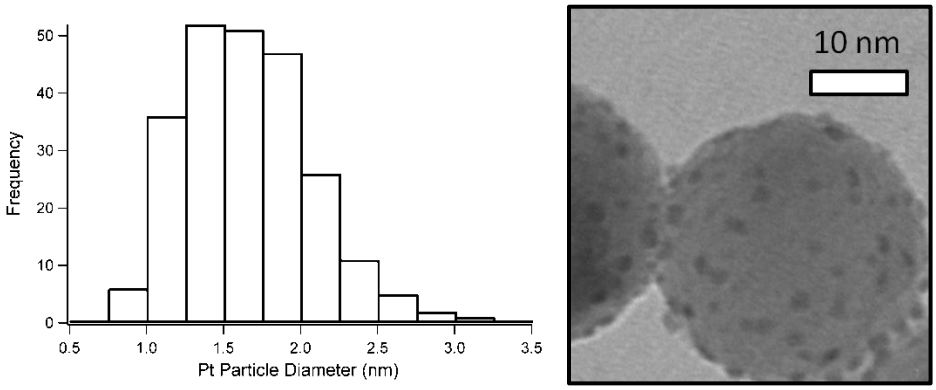

Figure 3.2B. Pt ALD particle size distribution and TEM image of 5 cycles H_2 Pt ALD

Platinum loadings measured by ICP were identical for the two samples at approximately 4.7 wt%. Analysis by TEM revealed that some alumina support particles had no Pt nanoparticles, indicating that the Pt particles were not uniformly distributed. Average particle size, weight loadings, and chemisorption values are listed in Table 3.1. Controlling the particle size on an oxide support is often difficult to achieve for particles smaller than 2.5 nm, especially for

techniques that do not require purification, removal of particle-stabilizing ligands, or anchoring steps.

Table 3.1. Pt catalyst properties

Catalyst [a]	**H_2 Adsorbed (µmol · $g_{catalyst}^{-1}$)**	**Pt Weight Loading (%)**	**Particle Size by TEM (nm)**	**Chemisorption Particle Size (nm) [H:Pt ratio]**
1 cycle Pt ALD with O_2	26	1.2	1.4 +/- 0.2	1.3 [0.9]
1 cycle Pt ALD with H_2	33	0.94	1.1 +/- 0.2	<1.1[b] [1.4]
5 cycle Pt ALD with O_2	74	4.7	2.4 +/- 0.5	1.8 [0.6]
5 cycle Pt ALD with H_2	91	4.7	1.7 +/- 0.4	1.4 [0.8]
Commercial 5 wt% Al_2O_3	40	5	3.9 +/- 1.1	3.6 [0.3]

[a] ALD catalysts reported in this table were synthesized on non-porous nanopshere alumina
[b] This sample had an H:Pt ratio of 1.4, making the particle size estimate slightly smaller than actual. The 1.1 nm size is the upper threshold (ignoring any H adsorbed beyond a H:Pt = 1)

3.4.2 In-situ ALD FTIR

The relative OH concentration during Pt ALD was measured via *in-situ* FTIR for both H_2 and O_2 ALD chemistries. Figure 3.3a shows spectra collected following each half cycle when H_2 was used as the second-cycle reactant. The OH stretching band (the broad peak at ~3500 cm^{-1}) did not change much after the first half-cycle. To ensure the surface was saturated, the precursor was statically dosed into the chamber for 30 min, and further exposure (up to 3 h) did not change the IR signal. Scans after subsequent cycles indicated more significant losses of hydroxyl groups, as shown in Figure 3.3a. During the 3rd Pt ALD cycle (not shown), the overall signal dropped to less than 0.1 % transmittance because the Pt increased the opacity of the sample. The sample grid was metallic and black after Pt ALD, whereas the original alumina/KBr powder was completely white. Carbonaceous species (2800-2900 C-H stretching regions) were also present

on the sample during most cycles, but these features were more prominent after the Pt doses (as expected from the organic groups of the precursor). Spectral noise at wavenumbers greater than 3500 cm^{-1} was due to gas phase water outside the *in situ* vessel. These results agree with the mechanism proposed by Setthapun *et al.* that Pt deposits on OH groups after the first cycle when H_2 is used.[19] Interestingly, during the H_2 doses, the OH groups also decreased in concentration. These losses were likely from H_2 dissociating on the Pt, then recombining with surface OH groups to form water.

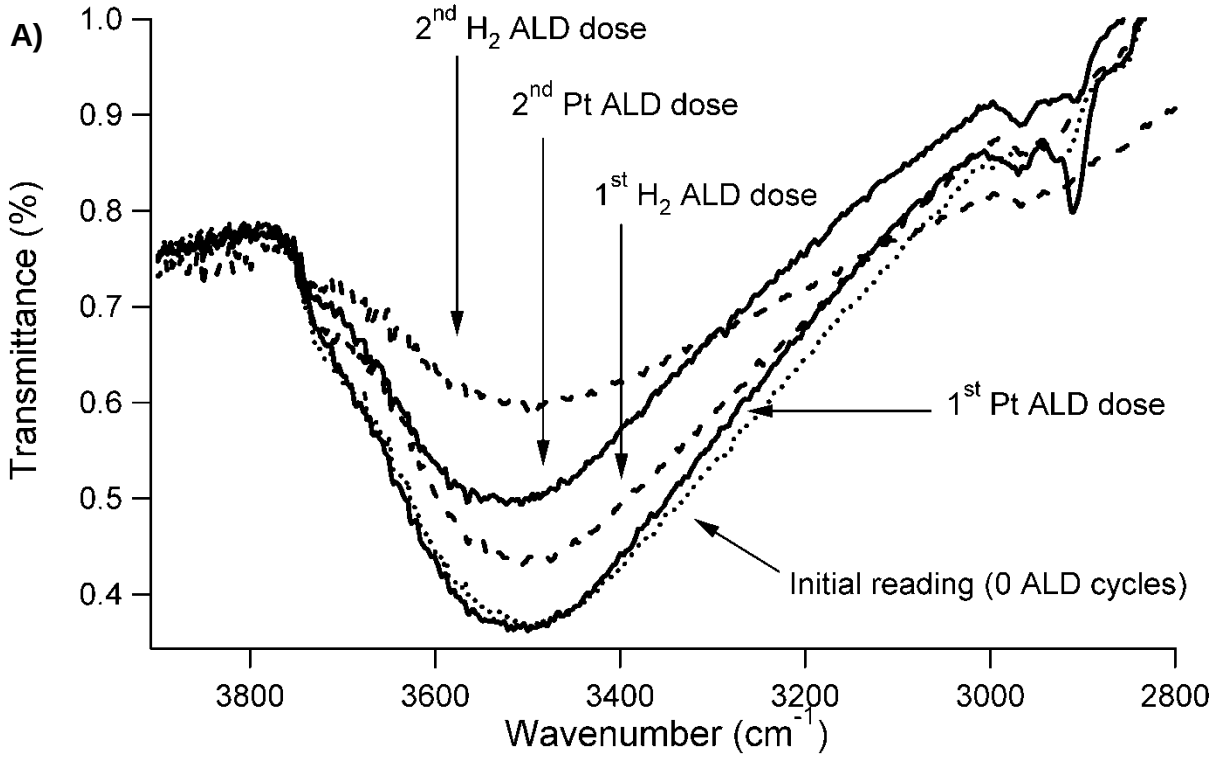

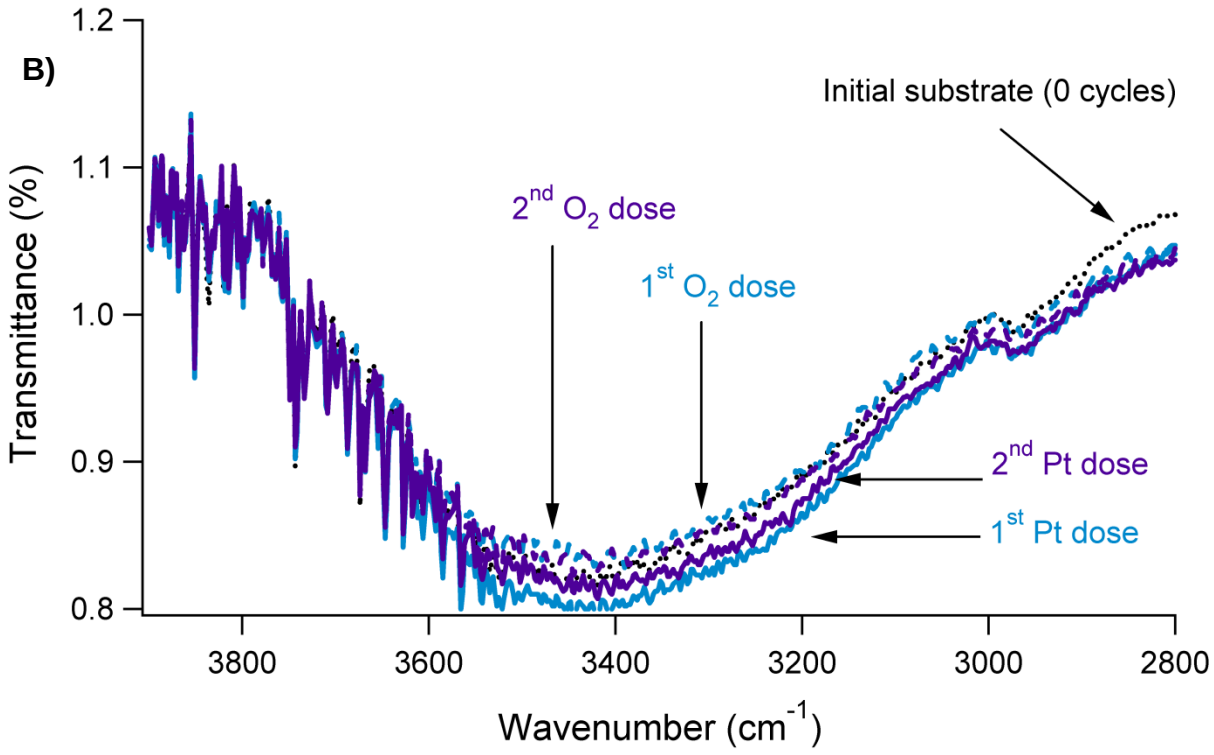

Figure 3.3. A) In-situ Pt ALD FTIR spectrogram with H_2 used as the second precursor. B) In-situ Pt ALD FTIR spectrogram with O_2 used as the second precursor.

The presence of OH groups during each cycle indicates that only a fraction of the OH groups reacted, and the rest remained on the surface. These residual OH groups may be protected by steric hindrance from the organometallic precursor (the bound precursor can extend approximately 0.7 nm away from the edge of a Pt particle), or they may be unreactive and lack an active Lewis acid site due to the orientation of the hydroxyl groups.[28] By reacting on the surface of the alumina, the newly-deposited Pt particles had to diffuse to form larger clusters. We propose that these hydroxyl groups played a significant role in limiting the size of the Pt clusters since the OH groups are known to interact with Pt or Pd atoms by reducing adsorption strength of the metal atoms on alumina near OH groups (therby decreasing their transition to sites near OH groups) and increasing the diffusion barrier across the alumina surface.[21, 22] The Pt clusters were therefore more numerous and smaller when deposited with H_2 instead of O_2.

A schematic representing this proposed particle formation mechanism is shown in Scheme 3.1, which illustrates the atom migration and coalescence that is often neglected in traditional single-site mechanisms in ALD literature.

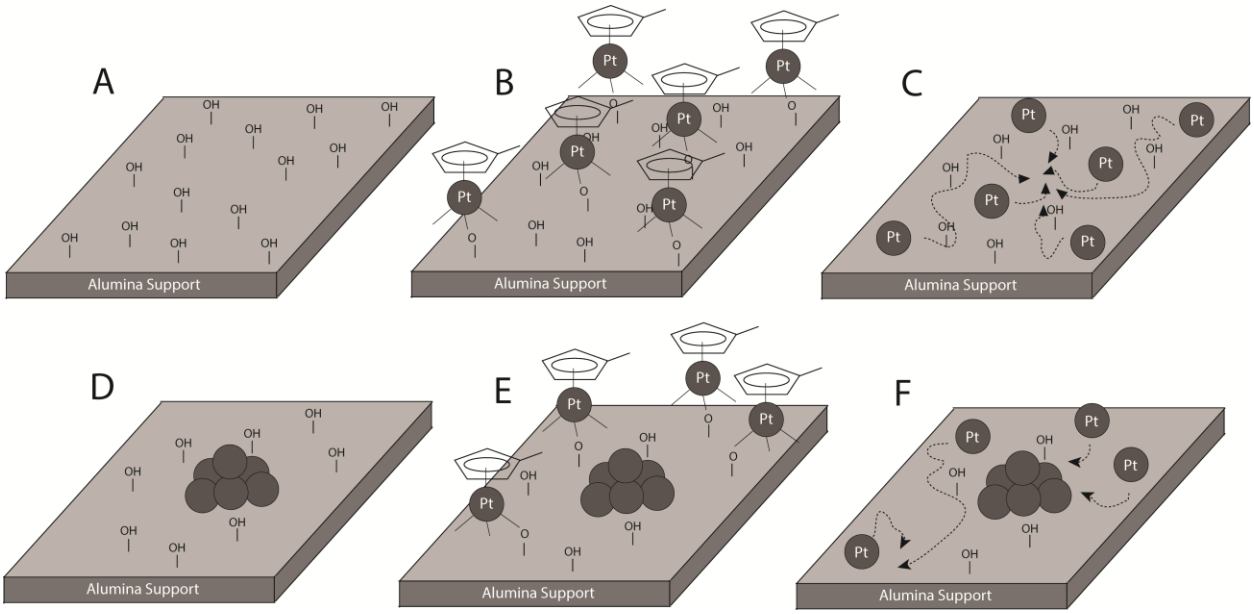

Scheme 3.1. Reaction scheme for metal island growth H_2 ALD. A) Alumina surface before Pt dose. B) Surface after MePt(Me_3Cp) dose. C) Pt atoms diffusing on surface after H_2 dose D) Pt nanoparticle formed. E) Next MePt(Me_3Cp) dose reacts on OH groups. F) Subsequent H_2 dose allows Pt to diffuse to existing particles or to form new particles.

When O_2 was used as the second ALD reagent, no discernable differences in hydroxyl groups were detected with additional ALD cycles (Fig. 3.3B). As with the H_2 chemistry, the sample became opaque due to Pt deposition after 3 cycles. Platinum was confirmed to be deposited on the sample by visual examination and ICP, much like that of the grid after Pt with H_2. The nearly-constant OH group concentration also supports the O_2-based Pt ALD mechanism proposed by Setthapun *et al.*, who suggested that halfway through the second cycle, new $PtMe_3$(MeCp) molecules start bonding to Pt-O species instead of OH groups. They observed this trend by monitoring the Pt EXAFS spectra, with no direct measurement of the OH groups, but here we monitored the OH concentration and arrive at a similar conclusion. Their EXAFS

studies combined with findings from this study suggest that after the first and second cycles nucleate Pt particles, the OH groups are still present but likely don't play any role in further Pt deposition when O_2 is used as the second reagent. Once new Pt precursor molecules bond to existing Pt clusters of ~30 atoms, the Pt atoms stick to the cluster because it is energetically unfavorable for Pt atoms to diffuse off that particle to form smaller particles or Ostwald ripen to grow similarly-sized particles.[29] In contrast, Pt atoms deposited with H_2 chemistry deposit on OH groups and diffuse across the alumina surface, thereby limiting their size relative to O_2 chemistry ALD that mainly grow on existing particles, as shown in Scheme 2. This argument applies when Pt particles are already on the surface, but a different mechanism must apply for the first Pt ALD cycle to create different particle sizes for the two chemistries. The difference between OH concentrations on the bare support and after the first Pt doses were so minimal that deducing mechanistic differences during the first ALD step (based on concentration of OH groups) was not possible.

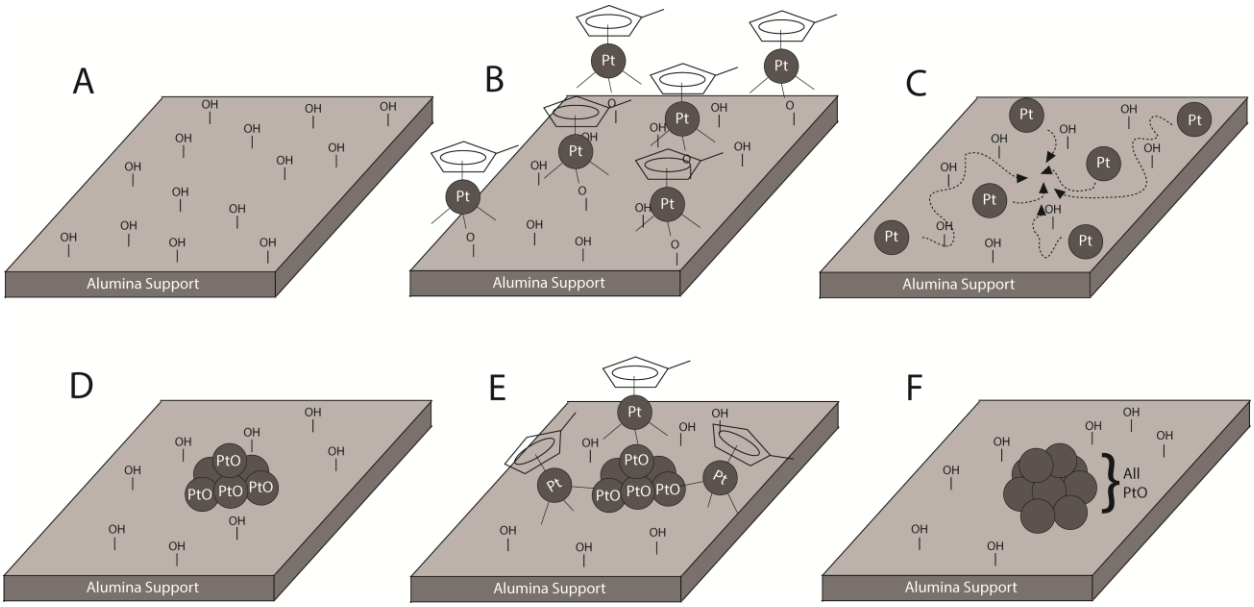

Scheme 3.2. Reaction scheme for metal island growth O_2 ALD. Steps A and B are identical to those in Scheme 1. C) Pt atoms diffusing on surface after O_2 dose D) Pt nanoparticle formed. E) Next MePt(Me_3Cp) dose reacts on Pt-O sites. F) Subsequent O_2 dose removes organic ligands and newly deposited Pt bind to existing Pt clusters.

3.4.3 Probing surface structure by CO DRIFTS and CO TPD

The surface structure of the Pt nanoparticles was probed with CO using DRIFT spectroscopy and TPD. Lundwall *et al*. demonstrated the robustness of these techniques to detect differences in terrace or step site density for Pt particle sizes of 2.4 nm to greater than 4 nm.[30] They used UHV conditions, but these same techniques were applied here under ambient pressures on alumina-supported catalysts. Catalysts were prepared on porous supports for use in the reactor studies and the CO DRIFTS experiments, and their weight loadings and chemisorption H_2 uptake values are listed in Table 3.2.

Table 3.2. Catalyst properties for Pt ALD deposited on porous Al_2O_3

Catalyst	H_2 Adsorbed ($\mu mol \cdot g_{catalyst}^{-1}$)	Pt Weight Loading (%)	H:Pt ratio (mol H ·mol Pt_{total}^{-1})
1 cycle Pt ALD with H_2	62	1.4	1.7
1 cycle Pt ALD with O_2	58	1.4	1.6
5 cycle Pt ALD with H_2	103	3.0	1.3
5 cycle Pt ALD with O_2	167	7.4	0.9

The Pt particles deposited on the porous supports were in general smaller than those prepared on the nanosphere alumina previously mentioned. The largest particles, synthesized by 5 cycles of Pt ALD with O_2, only had Pt diameters of ~1.3 nm, but calculating particle size when the H:Pt ratio exceeds unity results in an underestimation of particle size, and therefore was not reported (the H:Pt ratio exceeds 1 if the particle size is below 1.1 nm). As particle size decreases, the ability for under-coordinated Pt to adsorb more than one H atom per active site increases, and therefore the H:Pt ratio increases with decreasing particle size.[27] The H:Pt ratio observed for the 1-cycle Pt ALD catalyst (with H_2) is in agreement with theoretical H:Pt ratios associated with raft-type Pt clusters of ~10 atoms. The smaller particle size on the porous support than on the non-porous nanospheres could be due to differences in OH surface concentration, curvature effects from the nanospheres, or diffusion limitations of the Pt precursor on the porous support. An in-depth study would need to be carried out to investigate why the particle sizes differed between the two substrates, but the general particle size trends were the same on each substrate.

Measuring the size of these small clusters can be challenging, but CO DRIFTS can help elucidate the average coordination number of the Pt clusters, and like H:Pt ratio, the CO stretching frequency is related to particle size. The two main features in the CO DRIFT spectra

were around 1815-1850 cm^{-1} and 2040-2075 cm^{-1} (spectra are shown in Supplemental Figure 3.S1). The peaks around ~1825 cm^{-1} correspond to bridge-bonded CO, whereas the other feature corresponds to CO linearly-bonded to an atop site at a step edge,[31] and linearly-bonded CO on a terrace site typically occurs for Pt(111) around 2065 – 2100 cm^{-1}. The frequencies reported in Figure 3.4 were measured at a CO pressure of ~180 Pa or higher, whereas at a pressure of 10.7 Pa, only one peak at 2017 cm^{-1} was observed for the 1-cycle sample, at 2042 cm^{-1} for the 5-cycle sample (CO DRIFTS at several CO pressures are shown in Supplemental Figure 3.S2). These shifts as a function of CO coverage were consistent with shifts due to dipole-coupling between CO molecules.[32, 33] The CO stretching peak position is plotted against H:Pt ratio in Figure 3.4, The prominent step-site IR feature of the ALD catalysts indicates that the concentration of step sites and other undercoordinated sites is high on these ~1.0 nm particles. Additionally, the bridge-bonded CO feature (around 1850 cm^{-1}) was minimal for the ALD catalysts because the particles are too small to have many sites on which CO could form a bridge conformation. Kappers and van der Maas investigated the variation of CO frequencies with coordination of Pt atoms, and assigned a coordination number of 5 to a CO adsorption peak at 2035 cm^{-1},[34] which is nearly identical to the peak location for the Pt catalyst produced from one ALD cycle with H_2. Additionally, the peak at 2047 cm^{-1} corresponds to an average coordination number of 6 for the 5-cycle ALD sample. The CO stretching frequencies for the catalysts are plotted against H:Pt ratio in Figure 3.4, and as expected, the frequency decreases as H:Pt ratio increases as the particles become smaller. A sample of the 5-cycle Pt ALD (O_2) catalyst was intentionally sintered to 1.6 nm (by treating in 100% H_2 for 4 h at 873 K) to show the effect of a slightly larger particle in the CO DRIFTS experiments and for catalytic evaluation.

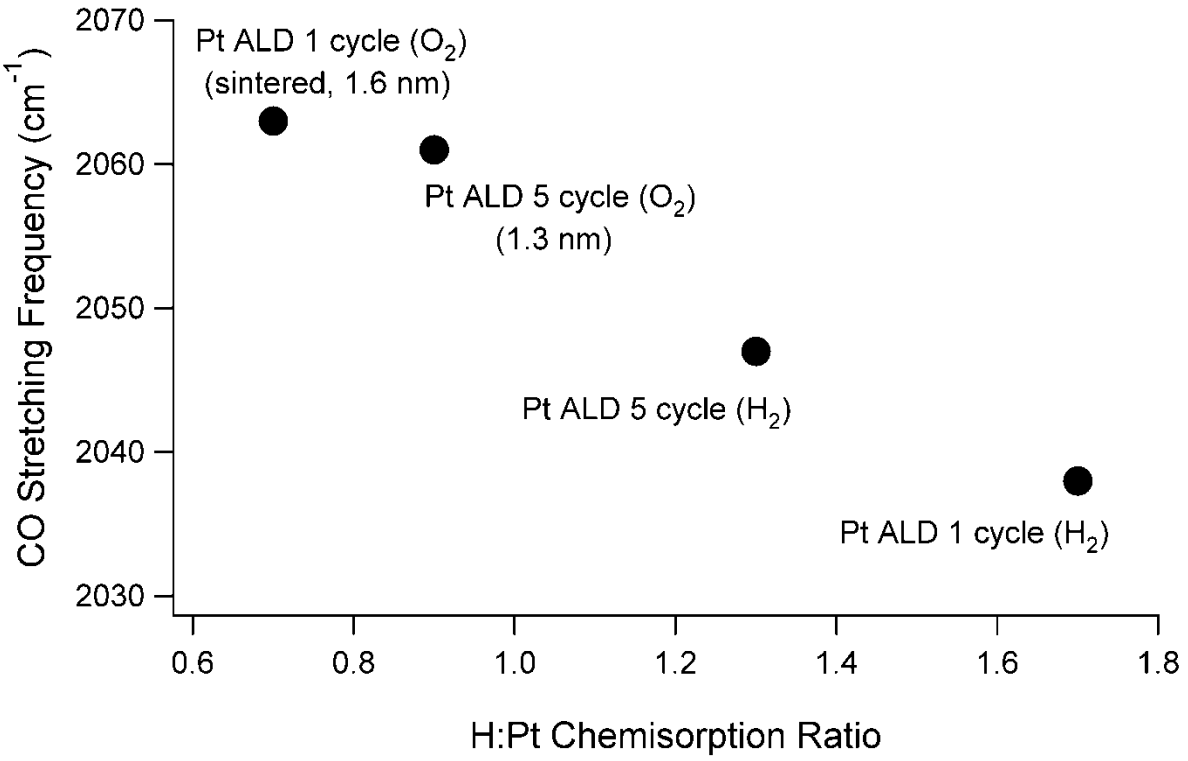

Figure 3.4. Carbon monoxide stretching frequencies from DRIFTS as a function of H:Pt ratios from chemisorption for several ALD catalysts.

The structures of the catalysts were further probed by CO-TPD. to elucidate the relative ratios of terrace sites to step sites on these small ALD catalysts. The study by Lundwall *et al.* investigated particle sizes from 2.5 nm to > 4 nm. In this study, particles with a smaller size (~1 nm) were investigated and the CO TPD profiles are shown in Figure 3.5a. The commercial 5 wt % Pt catalyst had a broad peak that is most likely composed of two separate peaks, one near 400 K corresponding to terrace site desorption and one near 450 K corresponding to step-site desorption. These two desorption modes were also identified by Lundwall *et al* for similarly-sized Pt particles.[30] All the ALD catalysts still desorbed CO as the temperature approached 550 K (shown as the trailing edge of the desorption peak), but all the CO had desorbed by 525 K for the commercial catalyst. The ALD catalysts made with H_2 each had a low temperature peak around 350 K that was not present for the other catalysts. The broad nature of the CO desorption

indicated that the surface of the Pt ALD particles were heterogeneous, encompassing a variety of terrace, step, corner, edge and kink sites. The higher-temperature desorption modes correspond to associative desorption on corner, edge, and kink sites.[35] Only terrace and step site desorption was observed by Lundwall *et al.*, but their particle diameters were at least 2.5 nm and therefore had a lower concentration of edges and corners than the ALD catalysts used in this study. Lower-coordinated atoms increase π back-bonding, which strengthens the binding energy of CO on Pt, and red-shifts the CO stretching frequency, as seen in Figure 3.4.

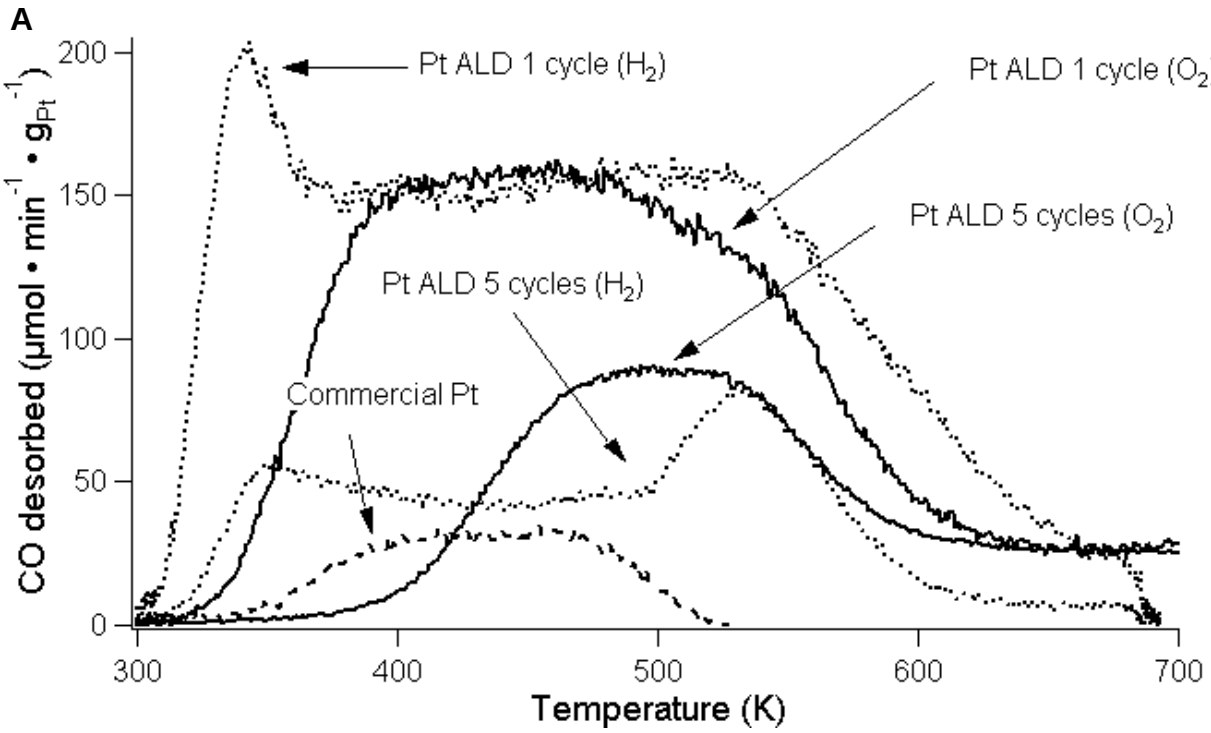

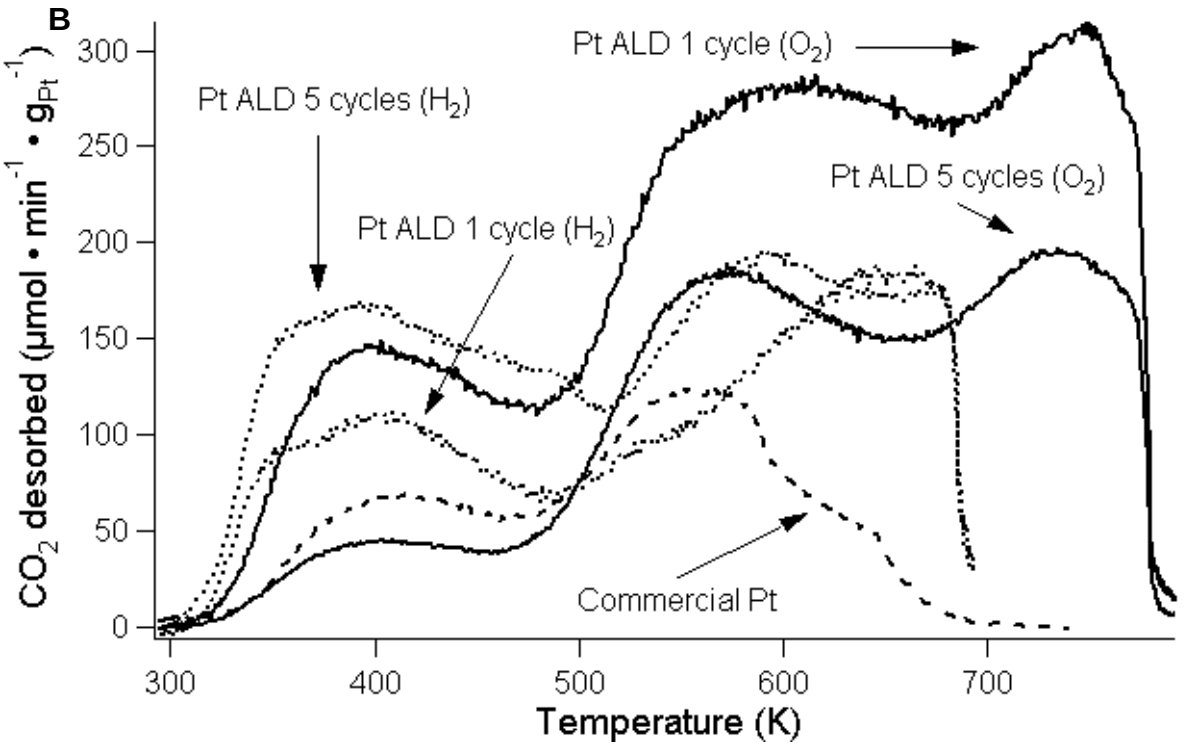

Figure 3.5. Carbon monoxide TPD of Pt catalysts with different particle sizes: A) CO desorption, B) CO_2 desorption

The desorption temperatures of this study agree with results from CO TPD in UHV on stepped Pt,[36, 37] and are similar to the results of CO TPD of Pt particles supported on γ-alumina.[35, 38] The 5-cycle H_2 Pt ALD sample, although it is likely slightly larger, still exhibited many of the nanoscale features of the 1-cycle sample. This sample most likely had some smaller particles, similar in size to the 1-cycle sample.

A significant portion of the adsorbed CO desorbed as CO_2, as shown in Figure 3.5b. Carbon dioxide can come from two reactions: 1) the water-gas shift reaction where OH groups from the alumina support combine with CO to produce CO_2 and H_2 gas, and 2) the Boudard reaction in which CO dissociates to form CO_2 and surface carbon.[35, 38, 39] For all catalysts investigated, the higher temperature CO_2 desorption coincided with H_2 desorption (shown in Supplemental Figure 3.S3), indicating that the CO_2 desorption proceeded through the water gas shift reaction

pathway at temperatures above ~500 K. The two catalysts synthesized by O_2 ALD exhibited similar desorption modes, and formed more CO_2 than the other catalysts. The O_2-synthesized catalysts most likely had a higher concentration of OH groups near the Pt particles to form more CO_2 during the TPD because the OH groups showed no decrease in concentration with ALD cycles when measured during *in-situ* FTIR of O_2-ALD.

A temperature-programmed study was also performed in the DRIFTS apparatus to help correlate peak features in CO TPD with species on the surface, as shown in Figure 3.6. The 5-cycle H_2 catalyst was used because its CO desorbed over a broad temperature range and it would provide a larger signal than the 1-cycle samples. The room temperature absorbance was similar to the CO stretching frequency in Figure 3.4, but increasing the temperature to 400 K redshifted the peak approximately 4 cm^{-1}. Additional increases in temperature shifted the CO adsorption peak even further, but at 500 K the peak shifted significantly. These absorption peaks were below 2000 cm^{-1}, and the study by Kappers and van der Maas assigned CO adsorption slightly below 2000 cm^{-1} to atoms with coordination numbers of 3 to 4.[34] The low wavenumber at temperatures >500 K indicate that the high-temperature features in the CO TPD were most likely desorption from sites with low coordination numbers. The CO TPD and the CO DRIFTS studies indicate that the ALD catalysts had a high concentration of these low-coordinated atoms.

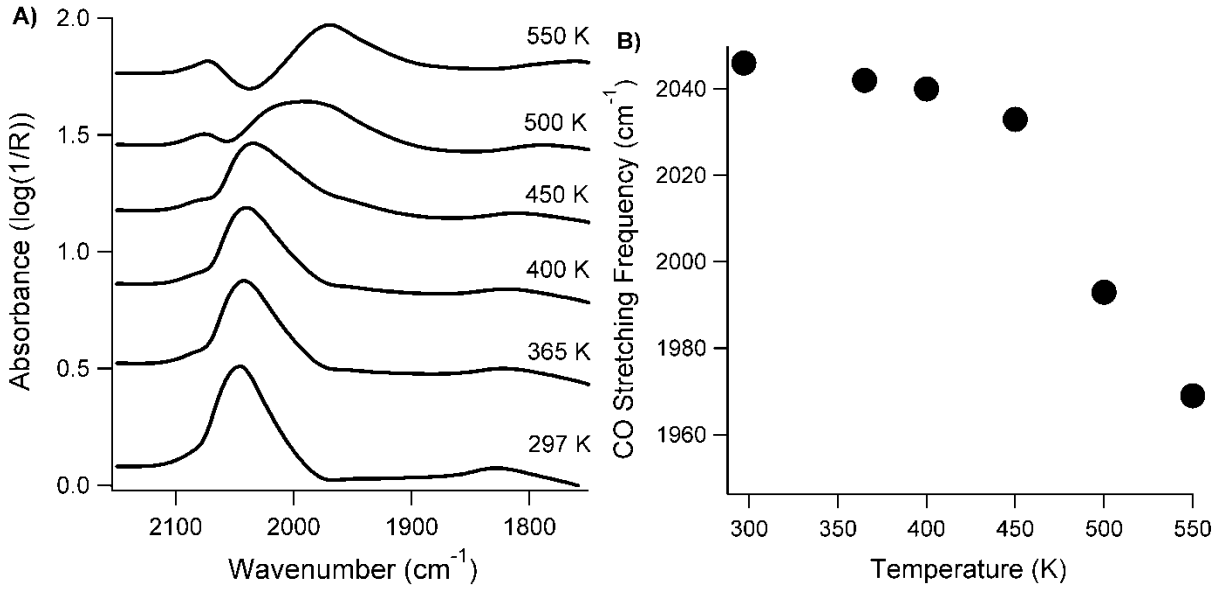

Figure 3.6. A)CO DRIFTS spectra for the 5-cycle H_2 ALD catalyst as a function of temperature, B) CO stretching frequency peak position as a function of temperature.

3.4.4 Catalyst evaluation for ODHP

The catalysts were screened for C_3H_6 selectivity, shown in Figure 3.7, by running the ODHP reaction with O_2 as the limiting reagent to reduce combustion of C_3H_8 and C_3H_6. The variation in selectivity with temperature agrees with the ODHP experiments by Lei *et al,* where the selectivity had a maximum around 673 K.[40] At 673 and 723 K, the catalysts with the smallest average particle size (one cycle Pt ALD with either H_2 or O_2) had the highest selectivities to C_3H_6 at 673 K, whereas at lower temperatures there were no trends with particle size. Propane should selectively dehydrogenate on lower coordinated atoms, which decrease in number as particle size increases. The two catalysts prepared with one ALD cycle had almost identical catalytic performance at the highest temperatures since they had similar particle sizes. The best catalyst had a ~5 % yield (conversion x selectivity), as shown in Supplemental Figure 3.S4, similar to a recently-reported PtPd bimetallic catalyst for ODHP, but the selectivity in this study was achieved using only one metal.[40] Selectivity to C_3H_6 was below the 1% detection limit for

the commercial Pt particles with an average particle size of 3.6 nm. The catalysts all stabilized within 2 h reaction time following a temperature increase, and showed no indication of further deactivation once at steady state. An example of the C_3H_6 mass signal versus time is shown in Supplemental Figure 3.S5.

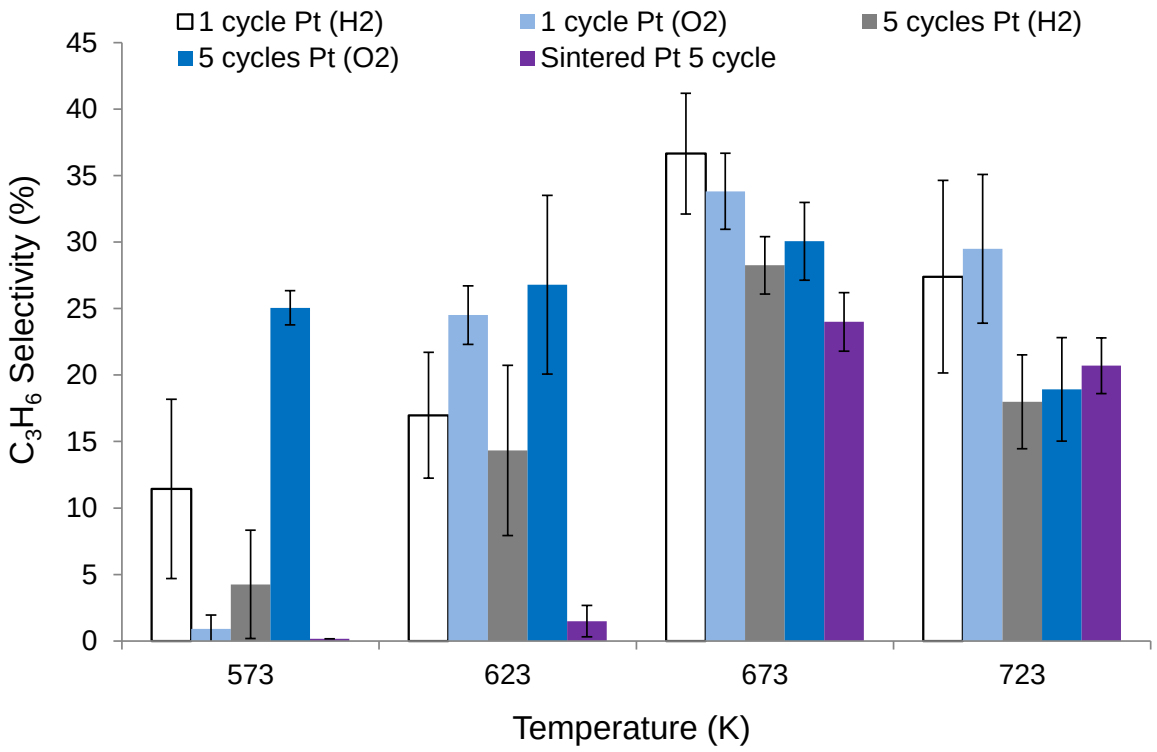

Figure 3.7. Selectivity to C_3H_6 vs. temperature for Pt ALD catalysts in the ODHP reaction. Error bars represent standard deviation from multiple experiments. The same catalyst weight and approximate space velocity were used for all measurements.

All the catalysts that had detectable ODH activity also produced H_2, which could have hydrogenated some of the C_3H_6 back to propane, since the O_2 was entirely exhausted during the reaction and not available to form water. Hydrogen production during ODH has been reported recently for a variety of catalysts,[7] and can be produced from catalytic dehydrogenation further down the catalyst bed once the O_2 has been exhausted, or the H_2 could come from the the water gas shift reaction if any CO was produced. Catalytic dehydrogenation was investigated by

running only C_3H_8 through the catalyst bed for the 5-cycle H_2 catalyst. During this test, H_2 and C_3H_6 were both detected at ~1/3 of the amount produced during ODH, but steadily decreased with time on stream, likely due to coking. The high selectivity observed in the O_2-lean reaction conditions likely was a combined effect of ODH (until the O_2 was depleted) and catalytic dehydrogenation.

Turnover frequencies, listed in Table 3.3, were measured at less than full O_2 conversion at 673 K and were the highest for the smallest particles and decreased with particle size. In a study on 8-10 Pt atom clusters by Vajda *et al.*, the Pt catalysts achieved TOFs of ~0.8 s^{-1} at 673 K.[9] The ALD catalysts reported here had intermediate TOFs between Vajda's catalysts and Pt monoliths tested with extremely short contact times (with a TOF of 0.01 s^{-1}).[10] The selectivities for all catalysts (when run at less than 100% O_2 conversion) were lower than when run in the O_2-lean conditions, likely because there was more O_2 available for C_3H_6 and C_3H_8 combustion.

Table 3.3. Catalytic ODHP performance at 673 K

Catalyst	C_3H_6 TOF [a] (mol C_3H_6· mol $Pt_{surface}^{-1}$·s^{-1})	C_3H_6 Selectivity (%)	C_3H_8 Conversion (%)
1 cycle Pt ALD with H_2	0.42 +/- 0.03	18	6.4
1 cycle Pt ALD with O_2	0.43 +/-0.04	13	6.3
5 cycle Pt ALD with H_2	0.26 +/- 0.04	7.4	7.7
5 cycle Pt ALD with O_2	0.11 +/- 0.02	7.0	6.9

[a] Errors of the TOFs reported above are representative of error in measuring the catalyst weight

3.5 Conclusions

Platinum nanoparticles particle could be synthesized between ~ 1 and 2.5 nm by varying the chemistry (O_2 or H_2) and number of cycles used. These catalysts were selective for oxidative dehydrogenation of propylene, with the smallest particles having the highest C_3H_6 TOFs , which were about half of the values reported for 8-10 atom clusters reported in literature. The differences between the second half-reaction chemistries used to produce these catalysts were probed via *in situ* IR, which showed gradual depletion of OH groups when H_2 was used, but relatively little change when the ALD was done with O_2. The type of surface atom was also found to vary with particle size, and these features were studied by CO DRIFTS and CO TPD. The catalyst with more lower-coordinated surface features (identified by CO DRIFTS) correlated with higher ODHP selectivity and activity at 673 K. The smallest particle sizes had the highest selectivity (37%) and TOF to C_3H_6 at ~0.42 s^{-1}. These small particle sizes are achievable through the facile ALD synthesis, and these ALD catalysts had much higher TOFs than mostly Pt (111)-terminated surfaces.

3.6 References

[1] G.A. Somorjai, H. Frei, J.Y. Park, Journal of the American Chemical Society 131 (2009) 16589-16605.
[2] G.A. Somorjai, R.L. York, D. Butcher, J.Y. Park, Physical Chemistry Chemical Physics 9 (2007) 3500-3513.
[3] Y. Li, G.A. Somorjai, Nano Letters 10 (2010) 2289-2295.
[4] E.L. Hu, S.M. Davis, R. Davis, E. Scher, Applications: Catalysis by Nanostructured Materials: Nanotechnology Research Directions for Societal Needs in 2020, in, Springer Netherlands, 2011, pp. 445-466.
[5] Ceresana, Market Study: Propylene (UC-1705), in, Ceresana, 2011.
[6] A. Corma, F. Melo, L. Sauvanaud, F. Ortega, Catalysis Today 107 (2005) 699-706.
[7] F. Cavani, N. Ballarini, A. Cericola, Catalysis Today 127 (2007) 113-131.
[8] R.A. Van Santen, Accounts of Chemical Research 42 (2008) 57-66.
[9] S. Vajda, M.J. Pellin, J.P. Greeley, C.L. Marshall, L.A. Curtiss, G.A. Ballentine, J.W. Elam, S. Catillon-Mucherie, P.C. Redfern, F. Mehmood, P. Zapol, Nat Mater 8 (2009) 213-216.
[10] B. Silberova, M. Fathi, A. Holmen, Applied Catalysis A: General 276 (2004) 17-28.

[11] M. Gharibi, F.T. Zangeneh, F. Yaripour, S. Sahebdelfar, Applied Catalysis A: General 443-444 (2012) 8-26.
[12] G.A. Somorjai, Y.G. Borodko, Catalysis Letters 76 (2001) 1-5.
[13] J.D. Aiken Iii, R.G. Finke, Journal of Molecular Catalysis A: Chemical 145 (1999) 1-44.
[14] F. Bozon-Verduraz, F. Fiévet, J.-Y. Piquemal, R. Brayner, K. El Kabouss, Y. Soumare, G. Viau, G. Shafeev, Brazilian Journal of Physics 39 (2009) 134-140.
[15] T. Aaltonen, M. Ritala, T. Sajavaara, J. Keinonen, M. Leskela¨, Chemistry of Materials 15 (2003) 1924-1928.
[16] S.T. Christensen, J.W. Elam, F.A. Rabuffetti, Q. Ma, S.J. Weigand, B. Lee, S. Seifert, P.C. Stair, K.R. Poeppelmeier, M.C. Hersam, M.J. Bedzyk, Small 5 (2009) 750-757.
[17] J. Li, X. Liang, D.M. King, Y.-B. Jiang, A.W. Weimer, Applied Catalysis B: Environmental 97 (2010) 220-226.
[18] Y. Zhou, D.M. King, X. Liang, J. Li, A.W. Weimer, Applied Catalysis B: Environmental 101 (2010) 54-60.
[19] W. Setthapun, W.D. Williams, S.M. Kim, H. Feng, J.W. Elam, F.A. Rabuffetti, K.R. Poeppelmeier, P.C. Stair, E.A. Stach, F.H. Ribeiro, J.T. Miller, C.L. Marshall, The Journal of Physical Chemistry C 114 (2010) 9758-9771.
[20] W. Kessels, H. Knoops, S. Dielissen, A. Mackus, M. van de Sanden, Applied Physics Letters 95 (2009) 013114-013114-013113.
[21] N. Aaron Deskins, D. Mei, M. Dupuis, Surface Science 603 (2009) 2793-2807.
[22] M. Corral Valero, P. Raybaud, P. Sautet, The Journal of Physical Chemistry B 110 (2006) 1759-1767.
[23] D.M. King, J.A. Spencer Ii, X. Liang, L.F. Hakim, A.W. Weimer, Surface and Coatings Technology 201 (2007) 9163-9171.
[24] T.D. Gould, A.M. Lubers, B.T. Neltner, J.V. Carrier, A.W. Weimer, J.L. Falconer, J. Will Medlin, Journal of Catalysis 303 (2013) 9-15.
[25] A.J.M. Mackus, N. Leick, L. Baker, W.M.M. Kessels, Chemistry of Materials 24 (2012) 1752-1761.
[26] K.L. Miller, C.W. Lee, J.L. Falconer, J.W. Medlin, Journal of Catalysis 275 (2010) 294-299.
[27] B.J. Kip, F.B.M. Duivenvoorden, D.C. Koningsberger, R. Prins, Journal of Catalysis 105 (1987) 26-38.
[28] S.D. Elliott, J.C. Greer, Journal of Materials Chemistry 14 (2004) 3246-3250.
[29] Y. Zhou, C.L. Muhich, B.T. Neltner, A.W. Weimer, C.B. Musgrave, The Journal of Physical Chemistry C 116 (2012) 12114-12123.
[30] M.J. Lundwall, S.M. McClure, D.W. Goodman, The Journal of Physical Chemistry C 114 (2010) 7904-7912.
[31] N. Lebedeva, A. Rodes, J. Feliu, M. Koper, R. Van Santen, The Journal of Physical Chemistry B 106 (2002) 9863-9872.
[32] C.A. Schoenbaum, D.K. Schwartz, J.W. Medlin, Journal of Catalysis 303 (2013) 92-99.
[33] R.M. Hammaker, S.A. Francis, R.P. Eischens, Spectrochimica Acta 21 (1965) 1295-1309.
[34] M.J. Kappers, J.H. Maas, Catalysis Letters 10 (1991) 365-373.
[35] A. Tanksale, J.N. Beltramini, J.A. Dumesic, G.Q. Lu, Journal of Catalysis 258 (2008) 366-377.
[36] G.S. Zafiris, R.J. Gorte, Journal of Catalysis 140 (1993) 418-423.
[37] J. Xu, J.T. Yates Jr, Surface Science 327 (1995) 193-201.

[38] K. Foger, J.R. Anderson, Applications of Surface Science 2 (1979) 335-351.
[39] S.D. Jackson, B.M. Glanville, J. Willis, G.D. McLellan, G. Webb, R.B. Moyes, S. Simpson, P.B. Wells, R. Whyman, Journal of Catalysis 139 (1993) 207-220.
[40] Y. Lei, B. Liu, J. Lu, R.J. Lobo-Lapidus, T. Wu, H. Feng, X. Xia, A.U. Mane, J.A. Libera, J.P. Greeley, J.T. Miller, J.W. Elam, Chemistry of Materials 24 (2012) 3525-3533.

3.7 Supplemental Figures

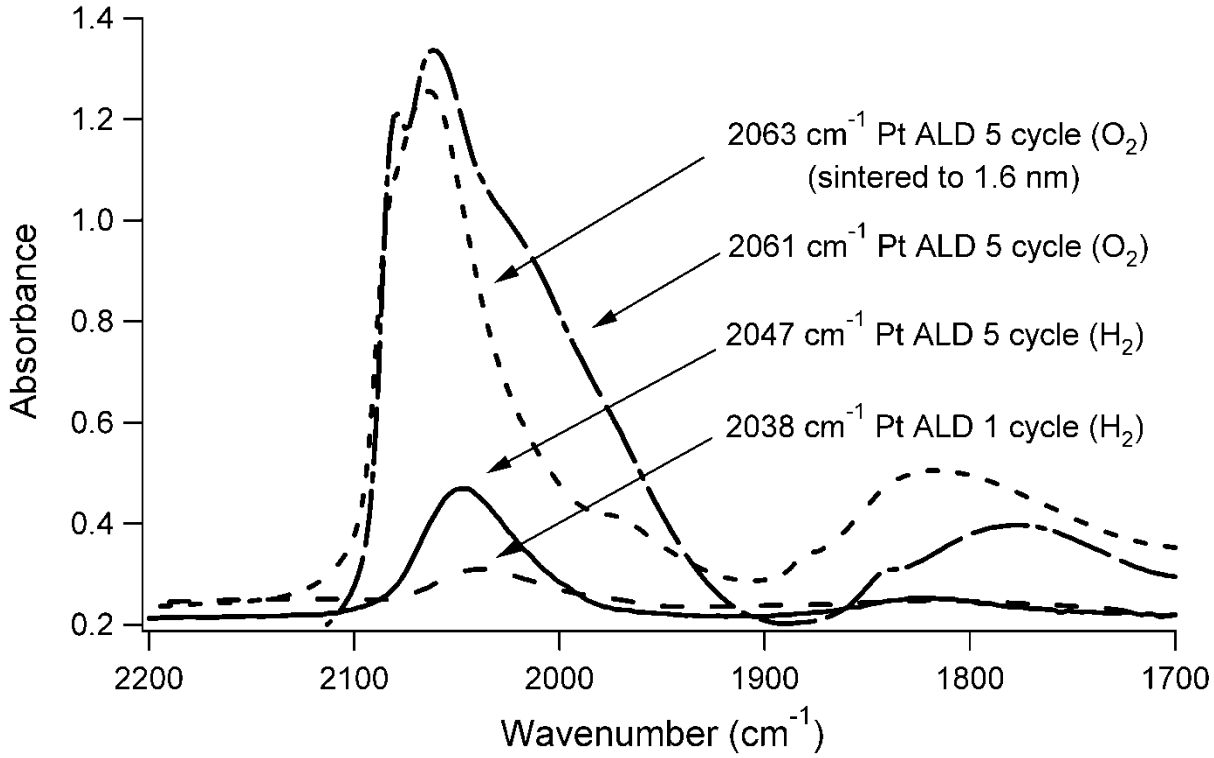

Figure 3.S1. Absorbance from CO DRIFTS experiments after CO saturation (~ 180 kPa) for the different Pt/Al_2O_3 catalysts. Peak locations for single-atom linearly-adsorbed CO stretching are noted.

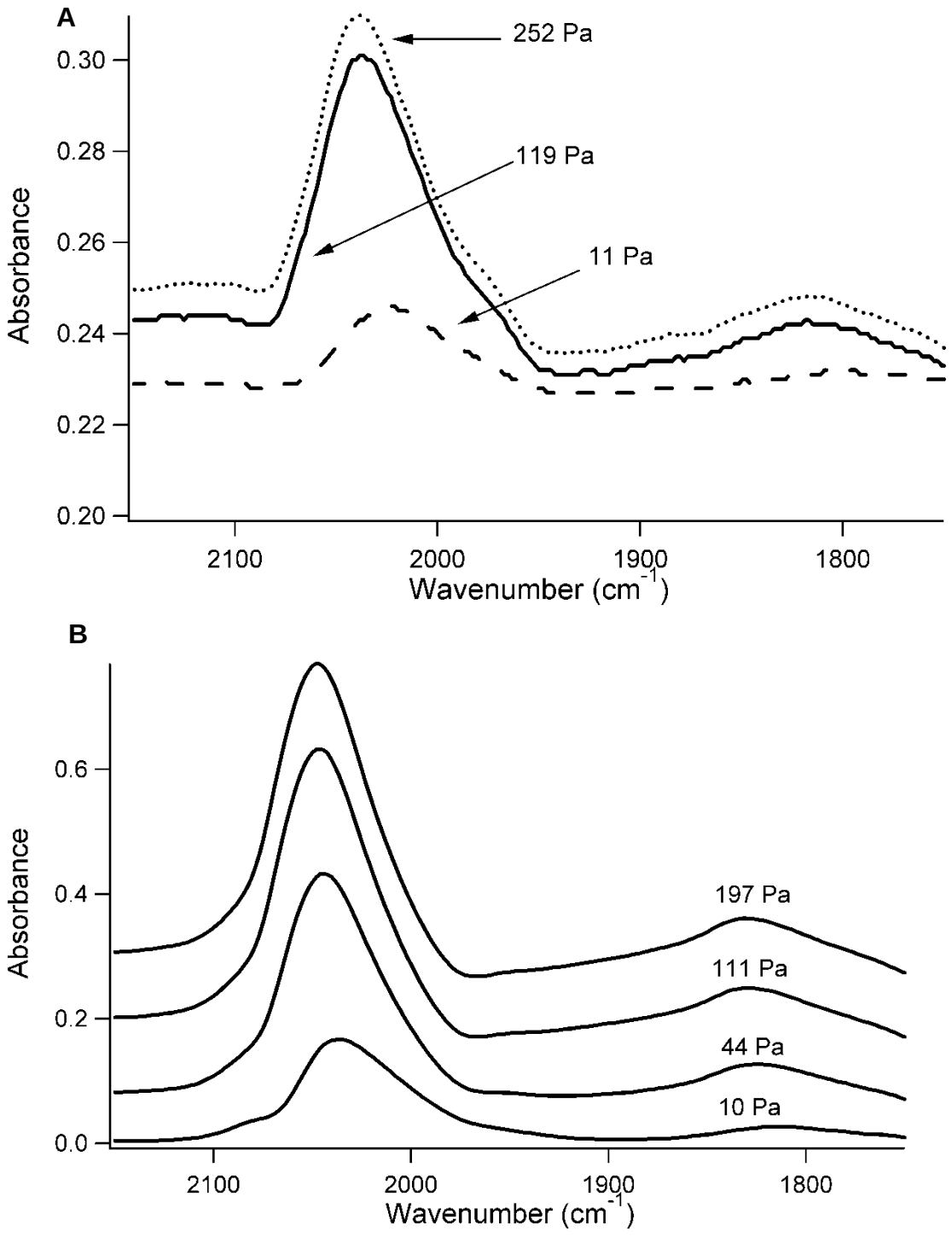

Figure 3.S2. CO DRIFTS spectra for catalyst at varying CO pressures (different pressures are labeled): A) 1 cycle Pt ALD (with H_2), B) 5 cycles Pt ALD (with H_2)

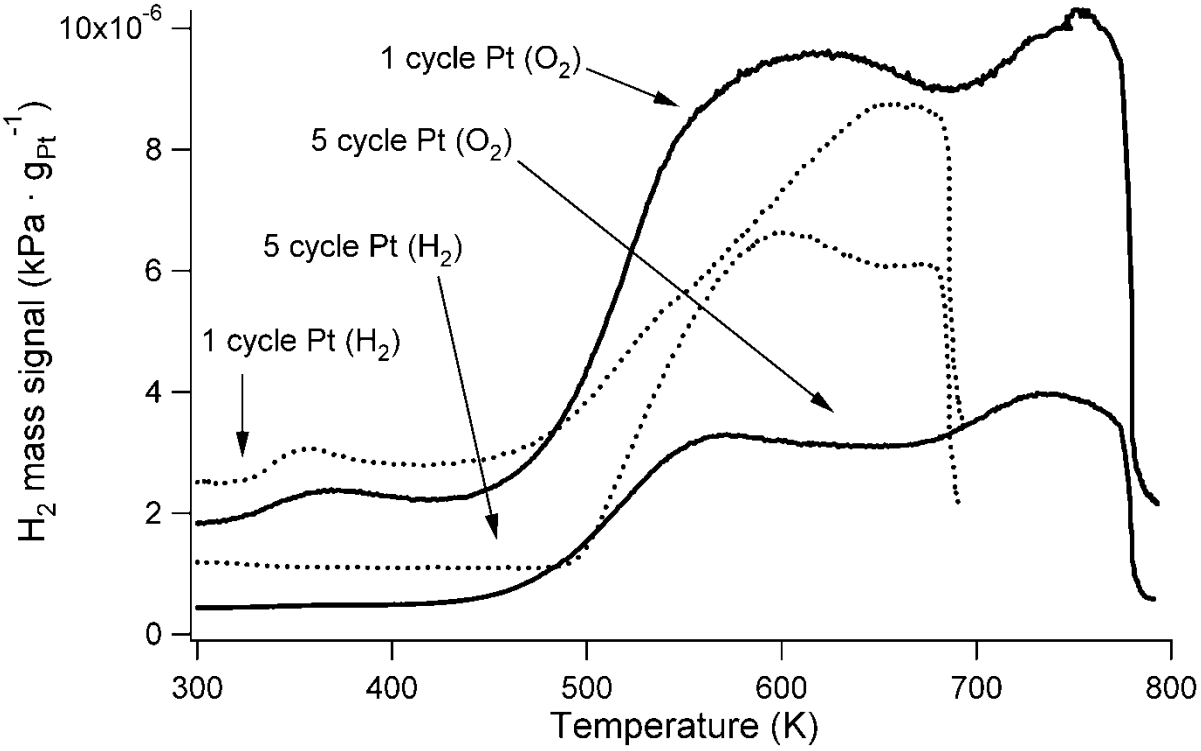

Figure 3.S3. Hydrogen produced during CO TPD for the ALD catalysts, coinciding with CO_2 desorption. The signal shown above is the raw H_2 signal normalized per g_{Pt}, but the H_2 signal was not calibrated.

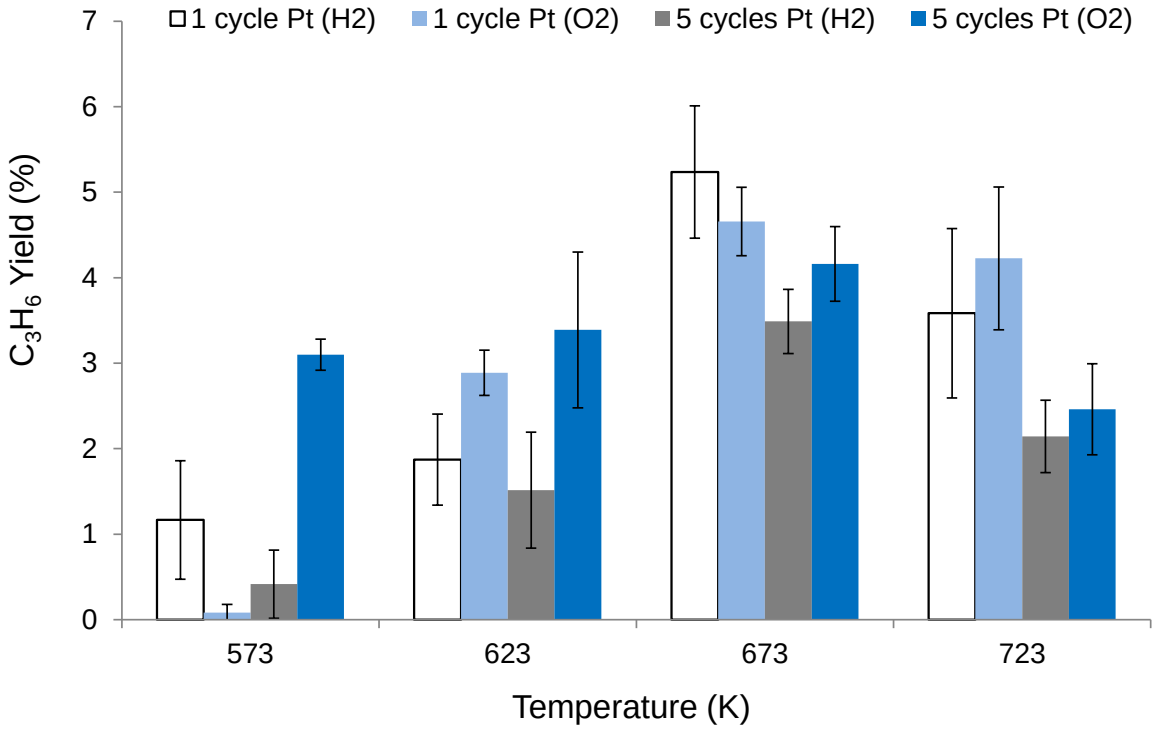

Figure 3.S4. Yield of C_3H_6 during ODHP on the Pt ALD catalysts in O_2-lean reaction conditions.

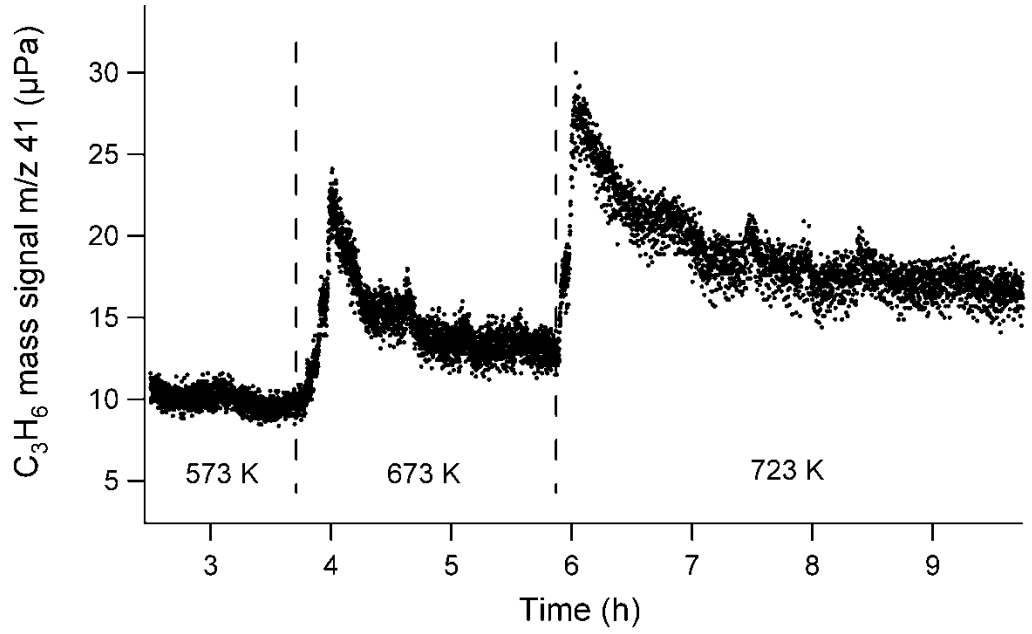

Figure 3.S5. ODHP reaction vs time for three temperatures on the Pt ALD 5-cycle (H_2) catalyst.

Chapter 4: Enhanced Dry Reforming of Methane on Ni and Ni-Pt Catalysts Synthesized by Atomic Layer Deposition

Submitted to *Journal of Catalysis* (January 2014)

4.1. Abstract

Atomic layer deposition (ALD) was used to deposit Ni and Pt on alumina supports to form monometallic and bimetallic catalysts with initial particle sizes of 1 to 2.4 nm. The ALD catalysts were more active (per mass of metal) than catalysts prepared by incipient wetness (IW) for dry reforming of methane (DRM), and they did not form carbon whiskers during reaction due to their sufficiently small size. Catalysts modified by Pt ALD had higher rates of reaction per mass of metal and inhibited coking, whereas NiPt catalysts synthesized by IW still formed carbon whiskers. Temperature-programmed reduction of Ni catalysts modified by Pt ALD indicated the presence of bimetallic interaction. Density functional theory calculations suggested that under reaction conditions, the NiPt surfaces form Ni-terminated surfaces that are associated with higher DRM rates (due to their C and O adsorption energies, as well as the CO formation and CH_4 dissociation energies).

4.2. Introduction

Recent advances in natural gas recovery and the associated drop in price of natural gas have drawn much attention to methane steam reforming and dry reforming of methane (DRM) with CO_2. Increases in global demand for transportation grade fuels and efforts to cap the amount of gas released or burned in blowouts have made gas to liquids (GTL) technologies more attractive.[1] The most widely used and economically viable GTL process is Fischer-Tropsch (F-T), which requires a syngas feed stream that is produced mainly by methane reforming.[1, 2]

Nickel, which is the primary catalyst used for these reforming reactions, is plagued by deactivation due to sintering and coking.[3, 4] Sintering decreases the metal surface area, and coking can build up enough carbon to clog or alter flow in reactors, cause overheating in tubular reformers, and destroy catalyst particles.[3, 5] The carbon whiskers formed during coking do not strongly affect the reforming rate initially because the carbon diffuses from the Ni active surface to the rear of the particle where the carbon whisker is attached.[3, 6] Reforming reactions are typically run at 973 to 1073 K to thermodynamically limit the reverse water-gas shift (RWGS) side reaction and coking from the Boudard reaction, but these high temperatures exacerbate sintering and are energy-intensive.[7] Promoters, such as K and Au, limit coking by acting as step-edge site blockers or by decreasing the carbon adsorption energy to prevent carbon nucleation on the catalyst.[5, 8] A recent density functional theory (DFT) study on graphite formation from CH_4 decomposition indicated that carbon preferentially nucleates on Ni(211) step edges as opposed to terrace sites.[5] This study also calculated that a Ni step edge must be longer than 2.5 nm to form a stable carbon cluster from which more carbon can grow.

Several studies have shown that adding Pt to Ni catalysts improves DRM activity and stability at temperatures of 773 to 973 K.[9-11] Platinum can increase activity by increasing the reducibility of NiO species in close proximity to Pt; H and CO form on Pt and spill over to reduce NiO.[12] Additionally, Pt has been shown to limit coking, so that more active surface area is available for reaction.[13] Islands of Pt on the Ni surface or Pt in a surface alloy decrease the ensemble size of Ni regions and thus limit coking, which is more prevalent on larger Ni particles. Platinum also limits the amount of carbon whisker growth due to the low solubility of carbon in Pt and the low adsorption strength of carbon on Pt compared to Ni.[3, 14] Carbon whiskers grow on Ni when carbon diffuses across the surface and through sub-surface layers to

find favorable step-edge facets from which to grow.[3] According to previous DFT calculations, the barriers for diffusion across the surface (137 kJ/mol) and subsurface diffusion (150 kJ/mol) are much smaller than the 225 kJ/mol barrier for carbon diffusion in bulk Ni. [15]

Typical Ni and NiPt bimetallic catalysts have been prepared by precipitation, incipient wetness impregnation, microemulsion, or other solution-based techniques.[9, 10, 13] In the current study, Ni and NiPt bimetallic catalysts for the DRM reaction were synthesized by atomic layer deposition (ALD) with the goal of increasing the activity and resistance to coking over traditionally-prepared catalysts. Aaltonen *et al.* first deposited Pt films by ALD using hundreds of cycles of $Me(Me_3Cp)Pt$ and O_2.[16] Since that time, much research has focused on creating Pt nanoparticles with less than 10 cycles of Pt ALD on metal oxide supports.[17-20] Ruthenium, Pd, RuPt, and PdPt bimetallic catalysts were also deposited on metal oxide supports using ALD in recent years.[21-23] With the exception of one study of Pt ALD that used H_2 as the second half-cycle reagent,[19] all other noble metal nanoparticle formation by ALD used O_2 or formalin.[18, 20-24] Previous work demonstrated recently[25] that Ni ALD could also be performed with H_2.

In the present study, catalysts with approximately 2.4 nm Ni particles were synthesized by ALD, and their performance in DRM was compared to catalysts prepared by IW impregnation. The ALD-prepared catalysts had higher DRM rate per g-metal because of a higher active surface area. They also exhibited enhanced coking resistance. Catalysts prepared by ALD did not form carbon whiskers after 72 h of reaction at 873 K, whereas IW-prepared Ni catalysts readily formed these destructive carbon whiskers. Catalysts with even higher activity, stability, and coking resistance were prepared by adding Pt with ALD to create bimetallic catalysts with high dispersions to maximize the bimetallic effect. We characterized the structure

of bimetallic NiPt ALD catalysts using temperature-programmed studies, microscopy and specific chemisorption. Although the benefits of adding Pt to Ni DRM catalysts using methods other than ALD are known, reasons for the enhanced performance are not well understood, and thus DFT was used to elucidate why these structures provide enhanced DRM activity and coking resistance.

4.3. Experimental Methods

4.3.1 Catalyst synthesis.

Nickel and Pt particles were formed on alumina supports by ALD. Two alumina supports were used: a nonporous alumina (Aldrich 544833 gamma alumina, ~40 m^2/g BET surface area, ~45-nm diameter spheres) and a porous gamma alumina (Albemarle MARTOXID AN/I, ~150 m^2/g BET surface area, ~75-μm particle diameters). The Ni ALD was performed in a stainless steel fluidized bed reactor (FBR) described elsewhere.[25, 26] The Pt ALD was performed in a quartz tube FBR (6-mm inner diameter) with a quartz glass frit of 40-μm pore size that supported the powder bed. The powder was fluidized in this reactor at approximately 0.25-Pa pressure with He carrier gas flow rates of 5 to 20 sccm. Platinum was deposited at 448 K, which is much lower than the typical 573 K used for Pt ALD with $Me_3(MeCp)Pt$ and O_2.[18, 19, 24] In this work, H_2 was used as the second reagent instead of O_2 for both Ni and Pt ALD. For bimetallic Ni + Pt ALD catalysts, the Ni particles were first deposited by incipient wetness (IW) impregnation or by ALD. Details of the IW and ALD Ni synthesis are explained in previous work.[25] The Ni catalysts were dried for 2 h under vacuum at 939 K before Pt was deposited by ALD in the quartz FBR. A bimetallic NiPt catalyst was also synthesized by sequential IW impregnation (Ni followed by Pt) using the same methodology as the Ni IW synthesis, but using $H_2Pt_2Cl_6 \cdot 6H_2O$ as the metal precursor instead of $Ni(NO_3) \cdot 6H_2O$.

4.3.2 Catalyst Characterization.

The catalysts were characterized by temperature-programmed studies in a quartz tube reactor (6.35-mm inner diameter) at ramp rates of 60K /min and the effluent from the reactor was analyzed with an SRS RGA 200 mass spectrometer. For TPR, the catalysts were first oxidized for 2 h at 573 K and then cooled to room temperature in inert gas. The temperature subsequently was ramped in 50 sccm of 2.5% H_2 (balance Ar) while the H_2 uptake was measured with the mass spectrometer. For CO TPD, the catalysts were reduced for 2 h at 673 K, then cooled to room temperature, dosed with CO (50 sccm 20% CO in Ar) for 10 min, and then purged with Ar before ramping the temperature. In the case of post-reaction CO TPD experiments, the catalysts were reacted as normal, then cooled to room temperature before dosing CO.

Transmission electron microscopy (TEM) was used to estimate catalyst particle sizes and determine the type of carbon deposited on the surface. Particle size estimates were obtained using Image J software to analyze images from an FEI Tecnai 12 - Spirit Biotwin TEM and a Phillips CM-100 TEM. Samples were electrostatically adhered to copper grids with a lacey carbon over-layer (Ted-Pella 01895 Lacey Carbon Film grids) to avoid effects of solvents from dropcasting. Samples prepared for imaging purposes were synthesized using the same methodology as previously mentioned, but a nonporous nanosphere alumina (Aldrich 544833 gamma alumina) was used so that the metal catalyst was on the surface of the spheres.

The weight loadings of each sample were determined by inductively coupled plasma mass spectroscopy (ICP-MS) of samples digested in a concentrated $HF/HNO_3/HCl$ solution for over 24 h. The number of active sites was measured with a Quantachrome AS-1 Autosorb. The catalysts were reduced at 873 K in pure H_2 for 2 h before measuring the H_2 uptake to simulate the approximate surface area of these catalysts under reaction conditions. The active metal surface

area and particle diameters were not estimated for bimetallic samples because the surface composition must be known in order to attribute chemisorbed H_2 to Ni or Pt; instead the H_2 uptake is reported.

4.3.3 Reaction Studies.

The catalysts were evaluated for DRM activity in a quartz tube, packed bed reactor (6.35-mm ID). The catalysts were reduced for 2 h at 673 K in 10% H_2 (balance Ar), with the exception of the IW catalyst, which was reduced at 773 K before reaction to ensure the particles were fully reduced after they were calcined at 773 K during synthesis. All catalysts were heated to 873 K and held at that temperature for approximately 10 min before the reactants were introduced to the reactor. Effluent gases were analyzed by a SRI 8610c GC with a Haysep-D packed column. Gas flow rates were 20 sccm CH_4, 20 sccm CO_2, and 60 sccm Ar. The amount of catalyst in the bed was varied (typically 50 to 200 mg) to achieve similar initial CH_4 conversions (35 to 40%). The amount of catalyst, total volumetric flow rate, and CH_4 and CO_2 concentrations were similar to those used in several Ni-based DRM studies.[6, 9, 10, 13, 27, 28] Most reactions were run for 12 h, but some were run for up to 72 h. At the end of the reaction time, the reactant flow was stopped and replaced by inert carrier gas before cooling the catalysts in order to avoid additional carbon deposition as the reactor cooled.

4.3.4 Density Functional Theory Calculations.

All DFT calculations were performed by Matthew Montemore, and details regarding the computational methods used for those calculations can be found elsewhere.[29] Here we present pertinent methods to aid in understanding of the results presented in section 4.4 (this section 4.3.4 is courtesy of Matthew Montemore).[29]

A phase diagram was generated using atomistic thermodynamics, as described in detail in previous work.[30, 31] Briefly, the most stable surface structure at a given set of chemical potentials is the one that minimizes the surface energy:

$$\gamma(T,p) = \gamma_{clean} + \frac{E_{ads}}{A_{surf}} - \sum_i \frac{N_i \Delta\mu_i(T,p)}{A_{surf}} \qquad (1)$$

The number of each species in the surface unit cell, N_i, is defined by the surface structure, while the chemical potentials $\mu_i(T,p)$ are variables that depend on the temperature and pressure:

$$\mu_i(T,p) = \mu_0(T,p^0) + kT\ln(\frac{p^i}{p^0}) \qquad (2)$$

Several simplifications were made to make the phase diagram generation tractable. First, only two metal structures were considered: (i) a pure Pt top layer, a pure Ni subsurface layer, and NiPt bulk layers (Pt/Ni/NiPt); or (ii) a pure Pt top layer, a pure Ni subsurface layer, and NiPt bulk layers (Ni/Pt/NiPt). Previous work has shown that one of these two metal structures is the most stable under most O_2 chemical potentials.[31] Since these two structures have the same number of Pt and Ni atoms, terms that depend on N_{Pt} and N_{Ni} were not included in Equation 1.

Since the transition between the surface terminations occurs at a low coverage[31] (see Figure 4.3 below), only structures with 4/9 ML or less of combinations of C, CO, and O were considered. Their surface chemical potentials were calculated as:

$$\mu(O^*) = \mu(CO_2) - \mu(CO)$$
$$\mu(CO^*) = \mu(CO)$$
$$\mu(C^*) = \mu(CO) - \mu(O^*)$$
$$= 2\mu(CO) - \mu(CO_2)$$

Chemical potentials denoted with an asterisk indicate surface species; all other species are in the gas phase. Gas-phase chemical potentials are referenced to the isolated molecules. To account for coverage effects, adsorption energies calculated at 1/3 ML were used, but otherwise adsorbate-adsorbate interactions were ignored. Since only surface structures with a single type of adsorbate were found to be stable in the conditions tested, this is likely to be a good approximation.

4.4. Results and Discussion

4.4.1 Nickel Catalysts.

The Ni ALD catalyst was prepared with one ALD cycle on both porous and nonporous spherical alumina as described previously.[25] The Ni weight loadings of the ALD and IW catalysts were similar at 4.7 and 6 wt%, respectively, but the particle size of the as-synthesized catalysts differed significantly at 2.4 nm for the ALD catalyst [25] and 17 nm for the Ni IW catalyst. High-temperature reduction of the ALD catalyst resulted in some sintering. After the catalyst was held for 2 h at 873 K in 50% H_2, the average particle size obtained from TEM was 3.6+/-0.4 nm. This is similar to the particle size of 4.0 +/- 0.1 nm obtained from chemisorption after the same pretreatment (Table 4.1).

Table 4.1. Catalyst composition and chemisorption results

Catalyst	Weight loading		H_2 chemisorption	Active metal surface area	Particle size
	Ni (%)	Pt (%)	μmol/$g_{catalyst}$ (μmol/g_{metal})	($m^2/g_{catalyst}$)	(nm)
Ni IW	6	-	31 (520)	2.4	17
Ni ALD	4.7	-	96 (2000)	7.5	4
Pt ALD	-	1	33 (3300)	3.2	1
Ni IW + Pt ALD	6	1	69 (990)	-	-
Ni ALD + Pt ALD	4.7	1	105 (1800)	-	-
Ni IW + Pt IW	6	1	34 (490)	-	-

Nickel catalysts synthesized by incipient wetness (IW) and ALD techniques were evaluated for the DRM reaction. All IW-synthesized catalysts reached steady state within the first hour, but the Ni ALD catalysts took up to 25 h to reach steady state, as shown in Figure 4.1. The CH_4 reforming rate at 873 K (normalized per g_{metal}) at steady state for the Ni ALD catalyst was 1.6 times that for the IW Ni catalyst. Correspondingly, the metal surface area of the Ni ALD catalyst (calculated using post-reaction particle size measured by TEM)[25] was approximately 1.4 times higher than the IW catalyst surface area. Thus, the higher rate appears to be due primarily to the higher metal surface area (calculated from post-reaction particle size). However, comparing DRM rates normalized by surface area can over-represent the number of surface sites when carbon blocks an indeterminable number of sites. For this reason, we compare DRM rates normalized per gram-metal to avoid assumptions of rates normalized by surface area.

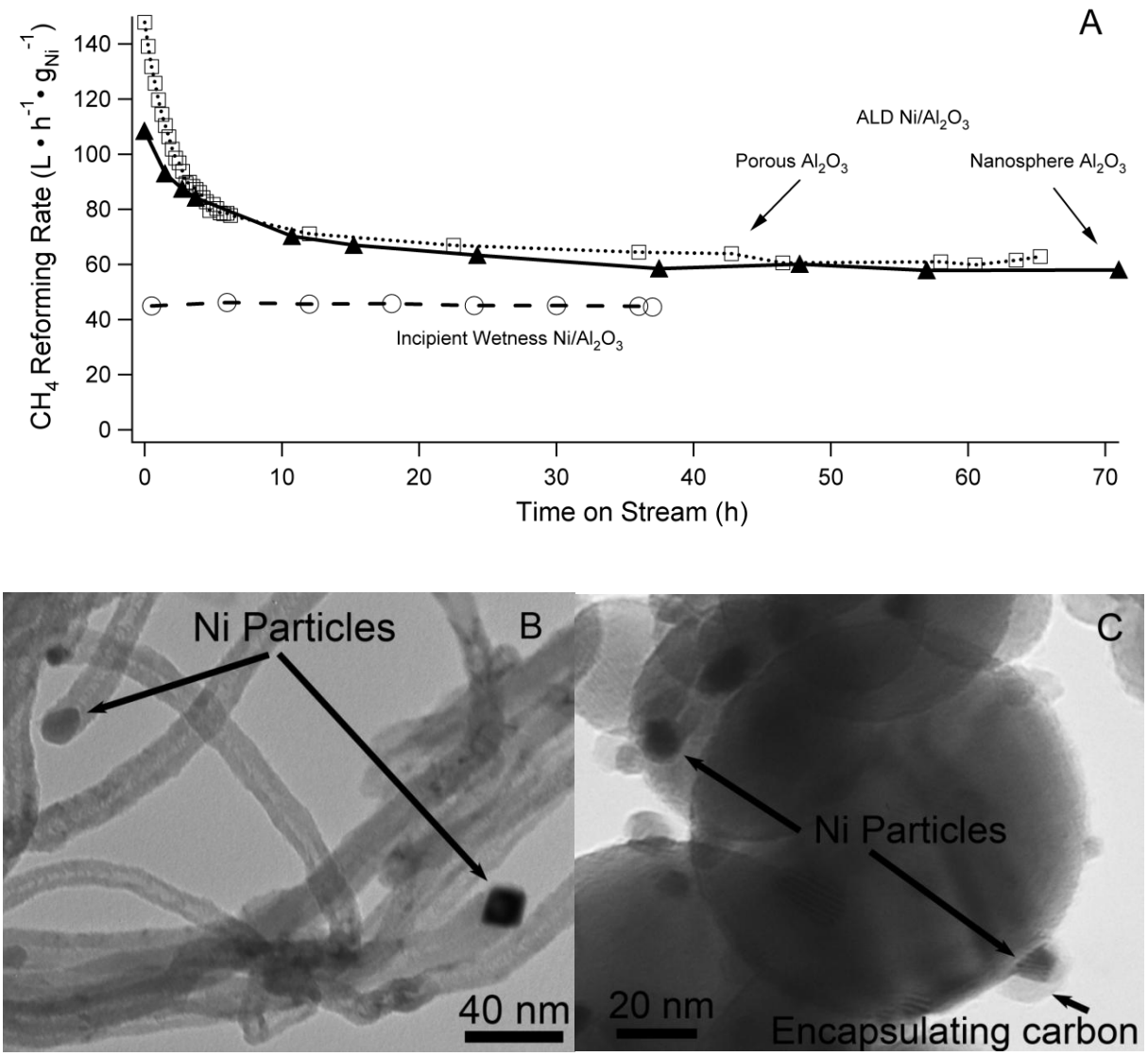

Figure 4.11. A) DRM reforming rates as a function of time for Ni IW and Ni ALD catalysts at 873 K. Both porous and nanosphere Al_2O_3 supports were used for the Ni ALD catalysts. B) TEM image showing carbon whiskers on the Ni IW catalyst supported on porous Al_2O_3 after 36 h on-stream. C) TEM image of Ni ALD catalysts on nonporous Al_2O_3 spheres after 72 h of DRM at 873 K.

The Ni ALD catalyst not only had a higher DRM rate (60 L $CH_4 \cdot h^{-1} \cdot g_{Ni}^{-1}$) than the IW catalyst (37 L $CH_4 \cdot h^{-1} \cdot g_{Ni}^{-1}$), it also had a higher rate than Ni catalysts in the literature; those rates were 10 to 25 L $CH_4 \cdot h^{-1} \cdot g_{Ni}^{-1}$ at 873 K under similar flow rates and pressures.[10, 13]

Nickel/Al_2O_3 IW catalysts investigated in this study had a higher rate than other Ni/Al2O3 catalysts reported in literature due to their lower weight loading and higher dispersion. The Ni ALD catalysts also had higher rates than a Ni/Mg(Al)O catalyst (5-6 nm Ni particles from a hydrotalcite-derived synthesis),[32] which had reforming rates of 43 L $CH_4 \cdot h^{-1} \cdot g_{Ni}^{-1}$ at similar conditions.[28] However, the Ni ALD catalysts had lower rates than similar-sized (2 nm initially) Ni nanoparticles of a Ni(Si_xO_z)/CeO_2 catalyst, which had a DRM rate of 270 L $CO \cdot h^{-1} \cdot g_{Ni}^{-1}$ (which corresponds to ~100 to 135 L $CH_4 \cdot h^{-1} \cdot g_{Ni}^{-1}$ depending on the H_2 to CO ratio) after 43-h reaction time.[33] Note that the steady-state rate for the Ni ALD catalysts in Fig. 4.1a was only reached after about 25 h, during which time the catalyst lost 59 to 67% of its activity. The Ni ALD catalyst was then stable for up to 72 h at 873 K.

The Ni ALD activity loss during DRM at 873 Kwas smaller than that observed by Baudouin et al. (80 to 90 %) when they used Ni/SiO_2 catalysts with initial particle diameters from 1 to 7 nm for DRM at 773 K.[27] The Ni ALD catalysts in the current study deactivated similarly to a 2.1-nm Ni(Si_xO_z)/CeO_2 catalysts that deactivated by 55% after 43 h.[33] The ALD catalyst particle diameters measured by TEM were 3.5 +/- 0.7 nm after 2-h reduction in 10% H2 at 673 K, and during reaction they sintered to 9.4 +/- 2.4 nm, which corresponds to a 39 to 77 % surface area loss. The activity loss over time appeared to be characteristic of particle sintering, so we modeled the reaction rate loss as being proportional to active surface area loss, as described by Bartholomew.[34] The decrease in surface area of transition metals due to sintering is known to follow power-law kinetics:

$$\frac{d}{dt}(A_{Ni}) = k(A_{Ni})^n \qquad (3)$$

where A_{Ni} is the surface area of the Ni catalyst, and *k* is the rate constant.[2, 34, 35] If we assume deactivation was solely due to a change in surface area, the reaction rate data in Figure 4.1a can be fit to the above power law, yielding a value of n = 7.5. This value of n is within the

particle coalescence regime ($n \approx 8$ or greater), as opposed to the atom migration sintering regime ($2 < n < 5$).[2, 4, 34, 35]

Although the Ni ALD particles sintered, they were still smaller than the IW Ni particles (approximately 17 nm both before and after reaction), and their small size may have limited the amount or type of coke deposition. No carbon nanotubes (whiskers) were detected by TEM on the Ni ALD catalyst after reaction, whereas the Ni IW catalyst had carbon nanotubes deposited throughout the sample after 36 h of reaction, as shown in Figure 4.1b. Although the reaction rate was stable for the IW catalyst, at longer times the carbon whiskers would be expected to eventually plug the reactor or destroy the catalyst particles. These carbon deposition results are similar to those found in the TGA study by Beengard *et al*. that showed when n-butane flowed over Ni catalysts while the temperature was ramped, coking began at a temperature 100 K higher and at a slower rate on 7-nm Ni particles than on 107-nm Ni particles.[5]

The Ni ALD particles shown in Figure 4.1 did not grow large enough to nucleate carbon whiskers after 72 h of reaction, but instead had thin layers of encapsulating carbon as shown in Figure 4.1c. This suggests that operating under reaction conditions can help limit sintering to the critical carbon formation size, which may be related to the encapsulating carbon formed on the particle surface. Particle migration and coalescence has been described as a surface-mediated transport of Ni atoms and Ni-OOH complexes from one side of the particle to the other.[4, 35] One possible explanation for not forming carbon whiskers on the Ni ALD catalyst is that once the encapsulating carbon layer formed on the Ni, particle migration and coalescence was effectively inhibited before reaching the critical whisker formation size. To support this hypothesis, we pre-sintered a Ni ALD catalyst for 24 h at 873 K in 20% H_2 and then ran the DRM reaction. This pre-sintered sample formed carbon whiskers instead of encapsulating

carbon, as shown in Supporting Information Figure 4.S1. The carbon whisker diameters (17.5 +/- 5.3 nm) were used as an approximation of the effective particle size,[3, 36, 37] indicating that these pre-sintered particles sintered to larger sizes under reaction conditions than the regular Ni ALD sample.

4.4.2.1 Nickel-Platinum ALD Catalyst Materials Characterization.

The nickel catalysts described above were used to create bimetallic catalysts by adding Pt by ALD or IW techniques. The Pt ALD deposited extremely small particles (approximately 1 nm) so that one ALD cycle added significant active surface area to the Ni IW catalyst, whereas Pt addition by IW added little surface area. The Pt ALD did not significantly increase the surface area of the Ni ALD catalyst (as indicated by a slight decrease in the H2 chemisorption uptake after Pt ALD), which was consistent with forming bimetallic particles rather than nucleating new particles. Weight loadings and chemisorption uptakes for each catalyst are listed in Table 4.1.

Temperature-programmed reduction (TPR) was performed to gauge bimetallic interaction of the catalysts (Figure 4.2). Monometallic catalysts were also investigated with TPR, and the Ni ALD catalyst exhibited a lower reduction temperature than larger Ni IW particles. The main H_2 uptake peak of the PtNi catalysts was between the peaks for the single-metal catalysts; this indicated the Pt was in close proximity to the Ni. This intermediate-temperature peak results by reducing a NiPt alloy or by Pt providing dissociated H for reducing nearby NiO species.[38] However, the peaks for the single-metal catalysts are also present in Figure 4.2 for the IW Ni catalyst modified with Pt ALD, suggesting that the catalyst was composed of isolated Pt and Ni particles or regions and NiPt alloy particles. The NiPt catalyst synthesized entirely by ALD did

not show much monometallic character however, indicating a higher degree of bimetallic interaction.

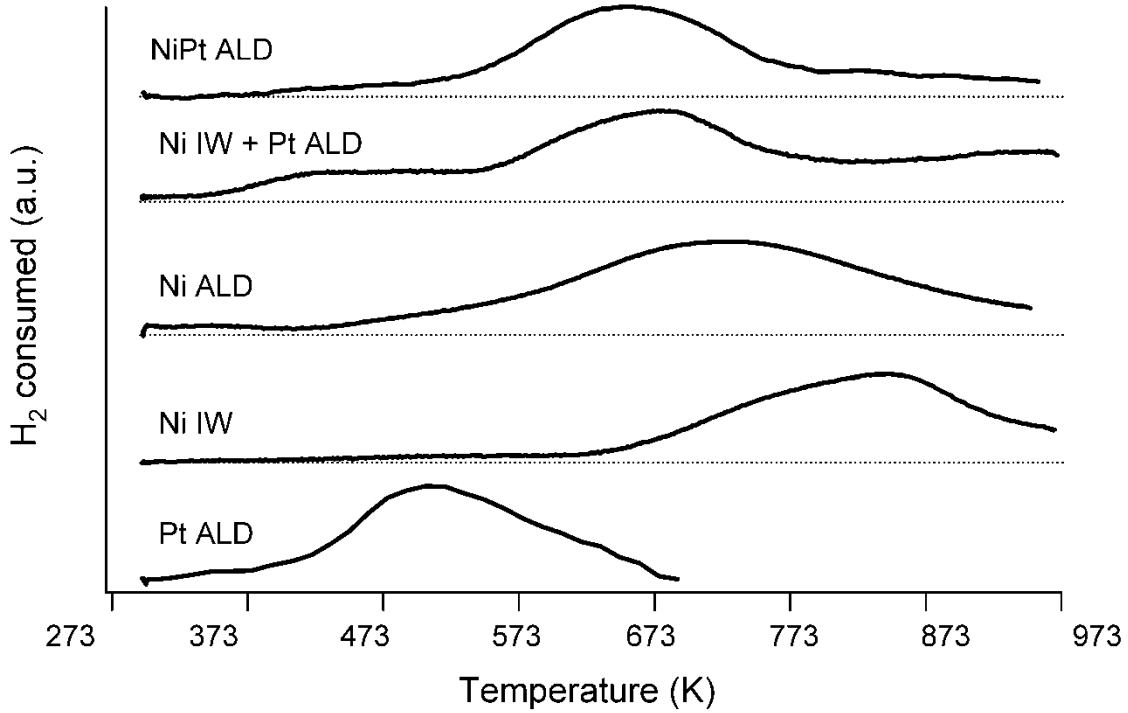

Figure 4.2. Hydrogen uptake of Ni, Pt, and NiPt catalysts obtained by temperature-programed reduction.

The structure of the bimetallic catalyst can change under reaction conditions, depending on which gases adsorb on the metal surface. Nickel-platinum bimetallic layers have been shown to change which metal terminates the surface depending on which gas adsorbed.[12, 39] Probing the catalyst surface structure with *in-situ* techniques is difficult under the harsh conditions associated with DRM. Instead, M. Montemore used DFT to analyze how the surface energy of different terminations varied as a function of coverage for multiple adsorbates associated with the DRM reaction. Previous work[31] has shown that for oxygen adsorption, the surface consists of either a pure Pt or a pure Ni top layer, depending on the oxygen chemical potential. Therefore, only the Pt/Ni/NiPt and Ni/Pt/NiPt structures were examined. As shown in Figure 4.3, M. Montemore determined that the Pt-terminated surface is more favorable at low adsorbate

coverages, but the difference becomes smaller as the coverage of any adsorbate increases.[29] The surface Pt termination is predicted to change to a Ni termination at low coverages of O or C, moderate coverages of CO, and high coverages of H.

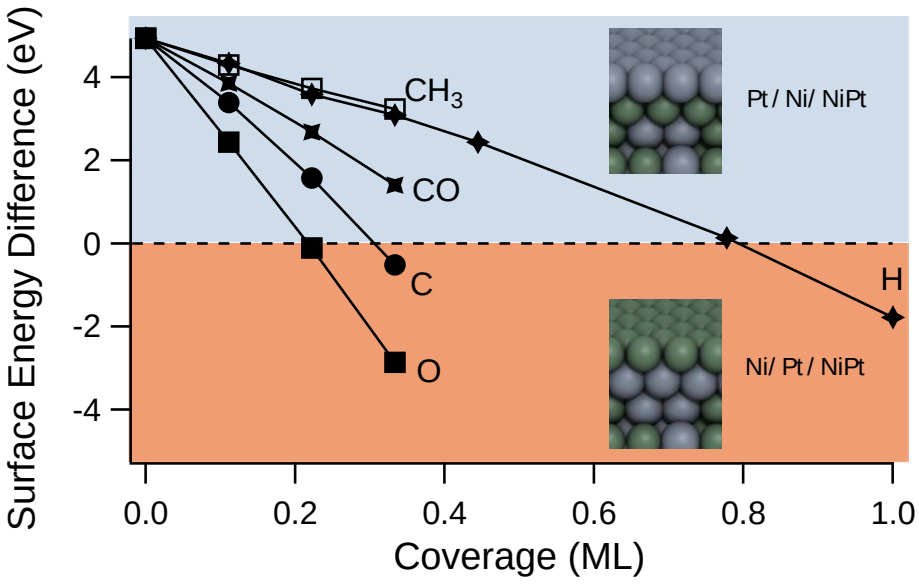

Figure 4.3. Adsorbate dependent surface termination of Ni-Pt bimetallic surfaces, where a positive value indicates that Pt/Ni/NiPt is more favorable and a negative value indicates that Ni/Pt/NiPt is more favorable. Insets show metallic structures that were used for the DFT calculations.

A phase diagram for the surface structure at different CO and CO_2 chemical potentials was also calculated by M. Montemore,[29] as shown in Figure 4.4. Under the experimental reaction conditions, the surface is predicted to be Ni-terminated and covered with atomic C. At low chemical potentials of both CO and CO_2, the surface is predicted to be Pt-terminated and bare, while at low CO_2 chemical potential the surface can be Pt-terminated with adsorbed CO, Pt-terminated and bare, or Ni-terminated with adsorbed O, depending on the CO chemical potential. Previous work on aqueous phase reforming of ethylene glycol on Ni-Pt catalysts also indicated that mostly Ni is on the surface under reaction conditions[39].

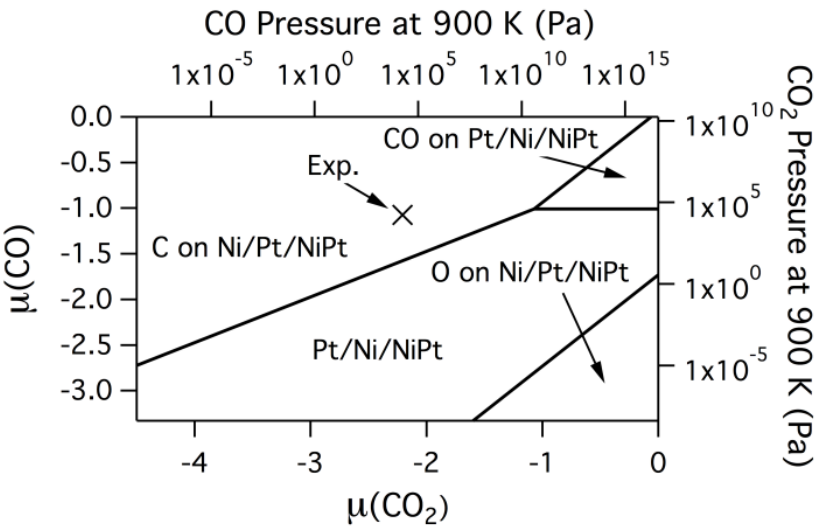

Figure 4.4. Phase diagram for NiPt bimetallic surfaces as a function of the CO and CO_2 chemical potentials. The "X" denotes representative chemical potentials of the adsorbates during the experiments in this work assuming atmospheric total pressure.

As an additional check on the DFT results, the surface structure was experimentally probed on a NiPt ALD catalyst. The catalyst surface during (and probably after) the DRM reaction conditions likely has significant amounts of surface C,[40, 41] which favors a Ni-terminated bimetallic surface as shown in Figure 4.4. Carbon monoxide TPD was performed on a fresh (reduced 2 h in 20% H_2 at 673 K) NiPt ALD catalyst and on a catalyst exposed to reaction conditions for 12 h at 873 K. The CO TPD, shown in Figure 4.5, has two peaks for the fresh sample, but only one peak after reaction. The peak around 373 K is representative of the α_1 single-site CO desorption mode on Pt and the higher temperature peak corresponds to a β_2 CO associative desorption mode from kink and step sites Ni.[38, 42] The Pt-related α_1 peak disappeared after reaction, indicating that those Pt sites were no longer available on the surface to bind CO. This Pt-related α_1 peak disappearance was not likely due to C covering the Pt sites. Montemore's calculations show that Pt-terminated surfaces exhibit larger C diffusion barriers (0.61-0.69 eV) than Ni-terminated surfaces (0.10-0.50 eV), and that Pt-terminated surfaces have

a less favorable C adsorption energies (-5.9 eV) than that of a Ni-terminated surface (-7.5 eV). Carbon on the bimetallic samples would thus be expected to preferentially form on the Ni regions and not diffuse to Pt metal sites or Pt-terminated bimetallic sites. Platinum weight loading of the post-reaction sample was confirmed by ICP-MS, indicating that the Pt was still in the sample at the original weight loading, just not on the surface. To ensure that the differences in CO desorption were due to reactant exposure and not high temperature, a NiPt ALD catalyst was reduced for 2 h at 673 K in 20% H_2, then held at 873 K in Ar for 12 h before running the CO TPD. This TPD showed both the low-temperature Pt peak and the high-temperature Ni peak, indicating that the disappearance of the Pt peak was not due to thermal treatment. Surface area loss and perhaps surface carbon were responsible for the decreased β_2 desorption peak after reaction. These TPD results agree with our findings from DFT that the surface was Ni-terminated during reaction.

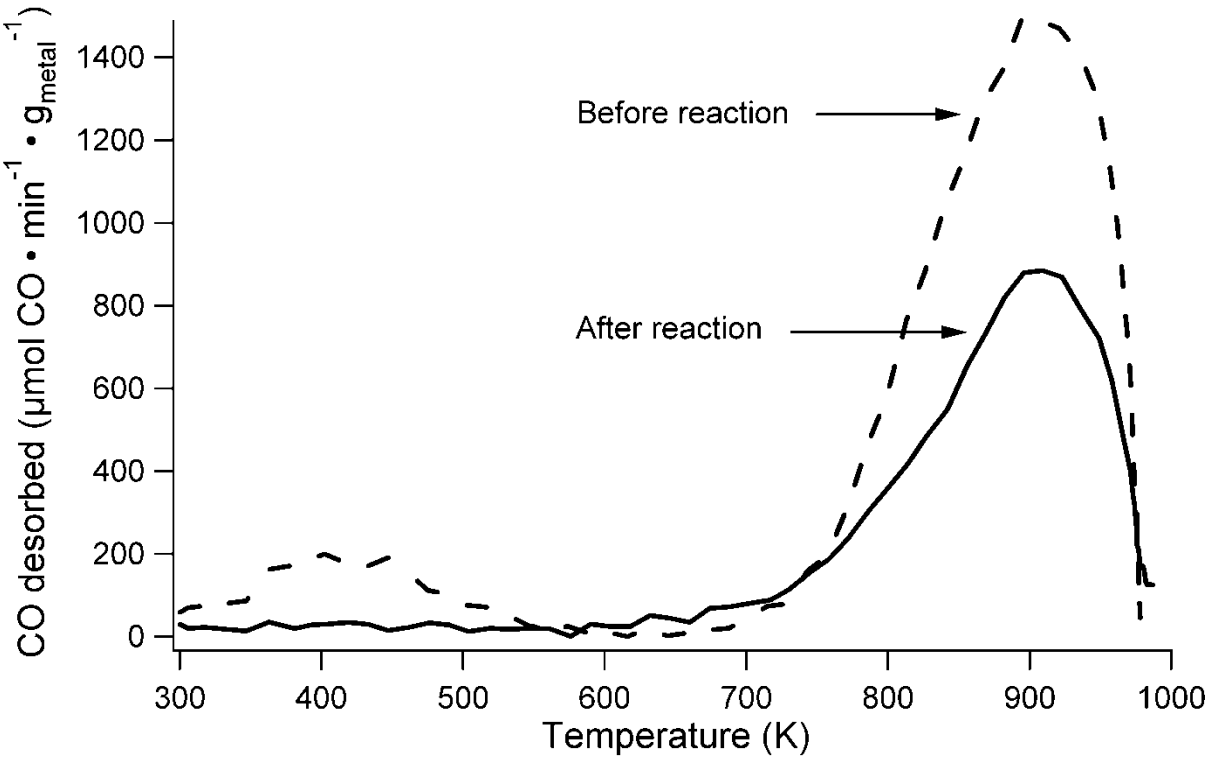

Figure 4.5. Carbon monoxide temperature-programmed desorption of Ni-Pt ALD catalysts before and after reaction.

4.4.2.2 NiPt DRM reactivity.

Modifying Ni catalysts with one cycle of Pt ALD increased the DRM catalytic activity by more than a factor of 2, as shown in Figure 4.6. A catalyst containing Pt deposited by one ALD cycle had a higher initial activity than that of the Ni ALD catalyst, but as shown in Supporting Information Figure 4.S2, it deactivated within 1 h to the steady state value reported in Figure 4.6. de Miguel *et al*.[13] observed previously that Pt-only catalysts deactivated by 75 to 80% at 973 K within 6 h during the DRM reaction. The NiPt ALD catalyst had a stable reforming rate after 10 h, whereas the monometallic Ni ALD catalyst was only stable after 25 h.

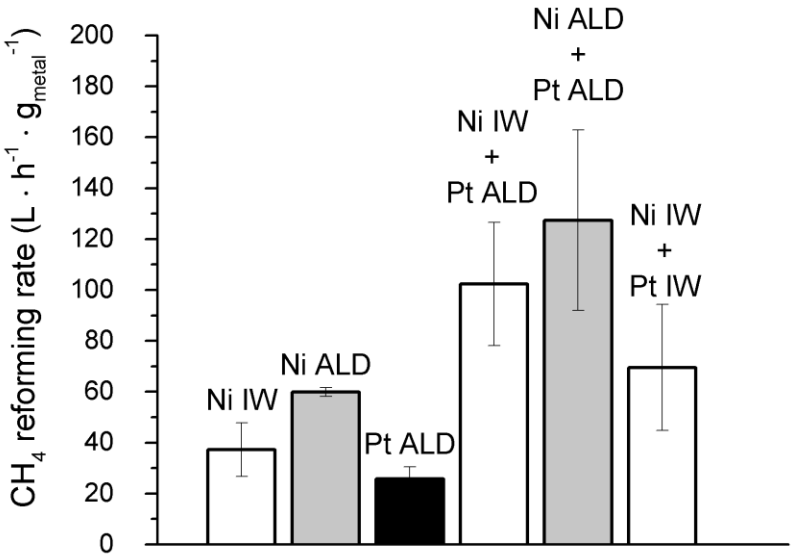

Figure 4.6. Steady-state rates of dry reforming of methane at 873 K normalized per gram of metal. The three bimetallic catalysts had Pt added to the two Ni catalysts shown on the left. Error bars represent standard deviation.

Adding Pt to the Ni catalysts by ALD increased the catalytic activity by more than the sum of each metal's activity. García-Diéguez *et al*.[10] reported no increase in DRM activity (per g_{metal}) at 873 K for $NiPt/Al_2O_3$ catalysts synthesized by simultaneous incipient wetness impregnation and reverse micro-emulsion with Ni loadings of 4 wt% and Pt loadings of 0.04% and 0.4%. de Miguel *et al*. [13] reported rates that were only 7.5% higher (per g_{metal}) at 973 K for $NiPt/Al_2O_3$ catalysts (0.5 wt% Pt, 10 wt% Ni) synthesized by excess-solution impregnation. Nickel-platinum catalysts prepared in this work by sequential incipient wetness impregnation had a dry reforming rate of 70 L $CH_4 \cdot h^{-1} \cdot g_{metal}^{-1}$. This is lower than the ALD bimetallic catalysts (102 to 127 L $CH_4 \cdot h^{-1} \cdot g_{metal}^{-1}$), but higher than the NiPt catalysts reported in literature (DRM rates of 13 to 26 L $CH_4 \cdot h^{-1} \cdot g_{metal}^{-1}$) because those catalysts had higher weight loadings and lower dispersions than the IW NiPt catalyst used in this study.[9, 10, 13] During DRM, the H_2/CO product ratios (~0.5-0.6) were similar for all catalysts investigated except for the Ni ALD + Pt ALD catalyst, which had a slightly higher ratio (0.67) as shown in Supporting Information

Figure 4.S3. These H_2:CO ratios are similar to other Ni, Pt, and NiPt catalysts reported in literature for DRM at 873 K.[10, 43]

DFT was used by M. Montemore to understand why the bimetallic catalysts had superior DRM rates.[29] Specifically, he investigated how bimetallic NiPt surfaces interacted with the different adsorbates found in the DRM reaction. Recent work by Jones *et al.* used first principles calculations and experimental investigations to elucidate which pure metals would be most favorable for CH_4 steam reforming.[14] They found that Ru was the best reforming metal and that the high reforming TOFs were correlated with the C and O adsorption energies calculated for that surface. By applying the same principles, M. Montemore used the O and C adsorption strengths on Ru as a benchmark to gauge which bimetallic catalyst surfaces would be more effective for dry reforming; i.e., a catalyst with C and O adsorption energies closer to those of Ru was deemed likely to be a superior catalyst.[29] In addition to comparing the C and O adsorption energies, the dissociative CH_4 adsorption and CO formation energies were also investigated since these are the kinetically limiting steps.[14] Four surfaces, shown in Supporting Information Figure 4.S4, were used to model the PtNi bimetallic surfaces. As can be seen in Figure 4.7, the Ni-terminated alloy has similar adsorption properties to Ru, and the similarity is maintained (though lessened) if 1/3 of the atoms in the top layer of this surface are replaced with Pt. This is in contrast to Ni, Pt, and the Pt-terminated alloy (even with 1/3 ML of Ni in the surface), which bind O and C too weakly. As noted above, experimental investigation and theoretical prediction indicated that the Ni-terminated surface is present under reaction conditions.

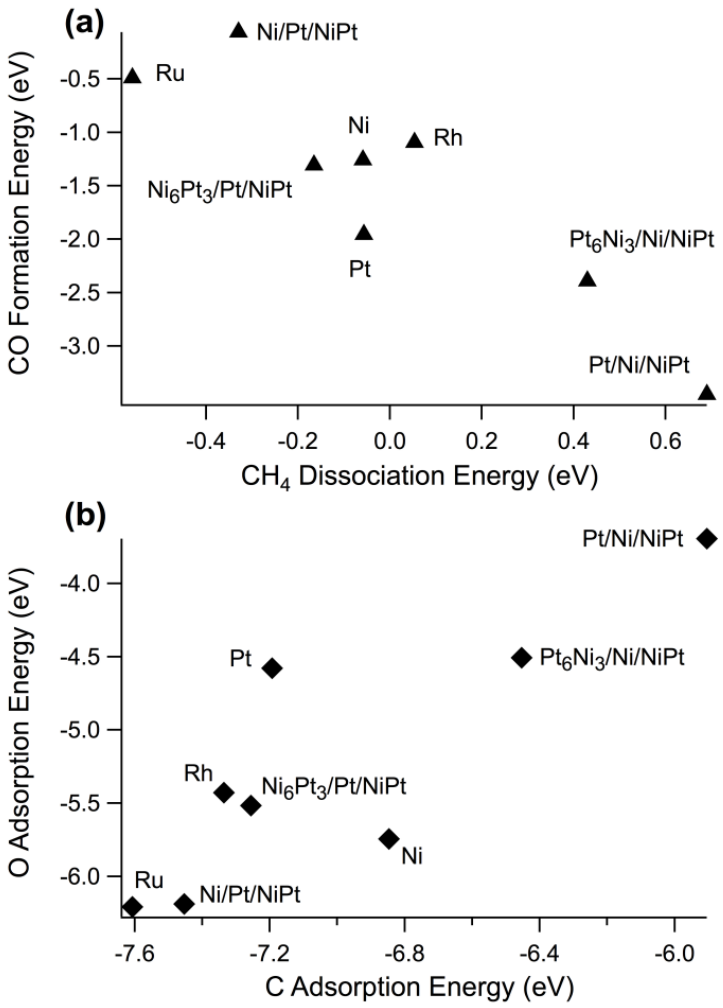

Figure 4.7. A) Carbon and oxygen adsorption energies of different metal surfaces. B) CO formation and CH_4 dissociation energies of different metal surfaces.

4.4.2.3 Carbon deposition on NiPt.

The post-reaction TEM images of the NiPt ALD catalyst show the particles ranged from approximately 3 to 20 nm (with average particle size of 9.4 +/- 4.5 nm), as shown in Figure 4.8. The larger particles would be expected to form carbon whiskers if they were not bimetallic, though the smaller particles could be monometallic and still not form carbon whiskers. Analysis by TEM of post-reaction bimetallic ALD samples indicated only sparse carbon whiskers on the samples, as shown in Figure 4.8, but the IW-prepared NiPt catalyst still had a large number of carbon whiskers. The carbon whisker growth on the IW Ni + Pt IW catalyst was similar to that of

the Ni IW catalyst, indicating that incipient wetness did not distribute Pt effectively on Ni particles, but ALD did. Platinum has been shown to decrease coking during dry reforming of methane on Ni-Pt bimetallic catalysts,[9, 11, 13] so the presence of carbon whiskers on the IW bimetallic catalyst is most likely due to large Ni-only catalyst particles or regions.

Temperature-programmed oxidation was used to characterize the amount of carbon deposited on the catalysts by measuring the amount of CO_2 produced. As shown in Supporting Information Figure 4.S5, the Ni IW + Pt IW catalyst had more than 2 orders of magnitude more carbon deposited than the Ni ALD + Pt ALD sample. This large discrepancy in carbon deposited was another indicator that Pt deposited by IW was not effectively dispersed and therefore did not limit coking the way Pt ALD did.

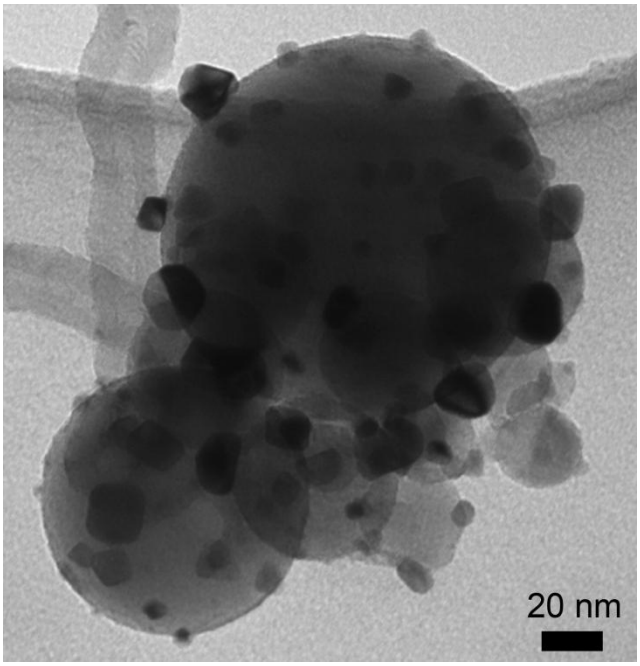

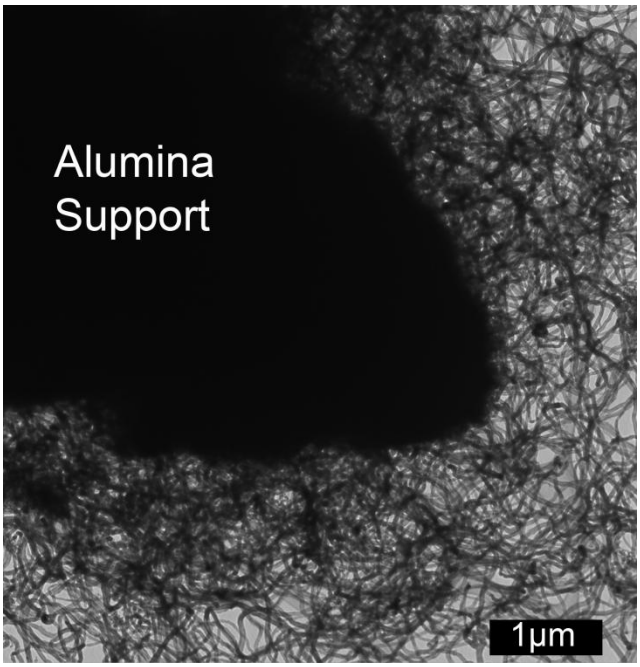

Figure 4.8. (Top) Bimetallic NiPt ALD catalyst particles after 32 h of reaction at 873 K indicate varying particle sizes with minimal carbon whisker deposition. Metal particles (dark <20 nm) were supported on spherical alumina supports. (Bottom) NiPt catalyst prepared by IW after 42 h of reaction show growth of carbon whiskers.

Density functional theory was used by M. Montemore to explore possible explanations for the amount of carbon deposition on different catalysts.[29] Importantly, whisker formation requires a much larger ensemble of contiguous sites than methane activation, so that whereas small quantities of surface Pt atoms would not be expected to strongly affect DRM activity, they may affect whisker growth. M. Montemore's DFT calculations suggest that suppression of coking may be due to the presence of some Pt "defects" on the active surface.[29] The tendency to coke likely depends on a number of factors, including the rate of C diffusion and the energetics of graphitic carbon formation.[15] In particular, the activation barriers for C diffusion have previously been used to explain the increased coke resistance of NiSn alloys.[44] M.Montemore's climbing-image, nudged elastic band calculations of the barrier for diffusion from an fcc hollow to a neighboring hcp hollow on Pt gave an identical result as simply performing an adsorption calculation in the bridge site.[29] Therefore, we used the difference in

adsorption energy between the bridge site and most stable site as a measure of the ease of carbon diffusion. The results (see Table 2) may explain why there is substantial coking on Ni but not on Pt, Ru and Rh: Ni has a much lower barrier to C diffusion. The Ni-terminated alloy also has a low barrier, but the coverage of 1/3 ML of Pt atoms in the surface layer significantly increases this barrier. At the high temperatures used in methane reforming, some Pt atoms may be on the surface, and these atoms may inhibit large-scale diffusion of C atoms.

Table 4.2. Barriers to atomic carbon diffusion

Surface	Diffusion Barrier (eV)
Ni	0.36
Pt	0.85
Ni/Pt/NiPt	0.10
Pt/Ni/NiPt	0.61
Ni_6Pt_3/Pt/NiPt	0.50
Pt_6Ni_3/Ni/NiPt	0.69
Ru	0.77
Rh	0.67

Since carbon preferentially nucleates at Ni step edges, M. Montemore investigated the effect of replacing one Ni (211) step edge atom with a Pt atom.[29] The calculated C adsorption energy (-7.45 eV) was weaker than the Ni (211) step edge C adsorption energy (-7.85 eV), indicating that Pt atoms near step edges may destabilize C nucleation. The same trend holds on the Ni-terminated alloy, Ni/Pt/PtNi(211); Pt at the step site destabilizes C by 0.07 eV, making it nearly equal to the adsorption energy on the Ni/Pt/PtNi(111) terrace (-7.45 eV). Therefore, surface Pt atoms inhibit C diffusion across the terraces and destabilize C adsorption at the step site, both of which may inhibit coking.

4.4 Conclusions

Nickel catalysts prepared by atomic layer deposition (ALD) had higher rates per g-metal for dry reforming of methane (DRM) than larger Ni particles synthesized by incipient wetness. These Ni ALD catalysts also inhibited the growth of carbon whiskers during reaction because the Ni particles were ~ 8 nm smaller than the IW catalyst particles, even after sintering. Adding Pt to the Ni catalysts by ALD increased the catalytic activity more than a factor of two, and the activity of these catalysts (on a per gram metal basis) was higher than NiPt DRM catalysts reported in the literature because of the small size of these particles. Also, less carbon deposited on the NiPt ALD catalysts than on all other catalysts investigated. Temperature-programmed reduction suggests these NiPt catalysts contain both bimetallic alloys and individual metal nanoparticles. Results from DFT calculations indicated that the NiPt catalyst surface was Ni-terminated under reaction conditions because adsorbates bring Ni to the surface. These Ni-terminated catalysts were predicted to perform better than Pt-terminated bimetallic catalysts or the individual metals. Bimetallic catalysts may have coked less because of the higher C diffusion barrier on terraces and weaker C adsorption energy at step edges where Pt is present. These ALD catalysts performed better than most DRM catalysts reported in the literature, likely because of their nanoscale features and maximized bimetallic interaction.

Acknowledgments

The work was supported through the National Science Foundation Graduate Research Fellowship Program and NSF Grants CBET 1067800 and CBET 0854251. The authors thank Fred Luizer in the University of Colorado's Laboratory of Environmental and Geological Studies (LEGS) for conducting ICP-MS analysis. The authors also thank Tom Giddings and the MCDB Bio3d Electron Microscopy center for the use of TEM microscopes and sample preparation equipment. Special thanks to Sarah Gould for designing graphical art. We acknowledge

supercomputing time at the Center for Nanoscale Materials at Argonne National Laboratory, supported by the U.S. Department of Energy, Office of Basic Energy Sciences, under Contract DE-AC02-06CH11357. A portion of the research was performed using EMSL, a national scientific user facility sponsored by the Department of Energy's Office of Biological and Environmental Research and located at Pacific Northwest National Laboratory.

4.5 References

[1] D.A. Wood, C. Nwaoha, B.F. Towler, Journal of Natural Gas Science and Engineering 9 (2012) 196-208.
[2] J.R. Rostrup-Nielsen, J. Sehested, J.K. Nørskov, Hydrogen and synthesis gas by steam- and C02 reforming, in: Advances in Catalysis, Academic Press, 2002, pp. 65-139.
[3] S. Helveg, J. Sehested, J.R. Rostrup-Nielsen, Catalysis Today 178 (2011) 42-46.
[4] J. Sehested, Catalysis Today 111 (2006) 103-110.
[5] H. Bengaard, J.K. Nørskov, J. Sehested, B.S. Clausen, L.P. Nielsen, A.M. Molenbroek, J.R. Rostrup-Nielsen, Journal of Catalysis 209 (2002) 365-384.
[6] V.C.H. Kroll, H.M. Swaan, C. Mirodatos, Journal of Catalysis 161 (1996) 409-422.
[7] S. Wang, G.Q. Lu, G.J. Millar, Energy & Fuels 10 (1996) 896-904.
[8] F. Besenbacher, I. Chorkendorff, B. Clausen, B. Hammer, A. Molenbroek, J.K. Nørskov, I. Stensgaard, Science 279 (1998) 1913-1915.
[9] M. García-Diéguez, E. Finocchio, M.Á. Larrubia, L.J. Alemany, G. Busca, Journal of Catalysis 274 (2010) 11-20.
[10] M. García-Diéguez, I.S. Pieta, M.C. Herrera, M.A. Larrubia, L.J. Alemany, Applied Catalysis A: General 377 (2010) 191-199.
[11] B. Pawelec, S. Damyanova, K. Arishtirova, J.L.G. Fierro, L. Petrov, Applied Catalysis A: General 323 (2007) 188-201.
[12] W. Yu, M.D. Porosoff, J.G. Chen, Chemical Reviews 112 (2012) 5780-5817.
[13] S.R. de Miguel, I.M.J. Vilella, S.P. Maina, D.S. José-Alonso, M.C. Román-Martínez, M.J. Illán-Gómez, Applied Catalysis A: General (2012).
[14] G. Jones, J.G. Jakobsen, S.S. Shim, J. Kleis, M.P. Andersson, J. Rossmeisl, F. Abild-Pedersen, T. Bligaard, S. Helveg, B. Hinnemann, J.R. Rostrup-Nielsen, I. Chorkendorff, J. Sehested, J.K. Nørskov, Journal of Catalysis 259 (2008) 147-160.
[15] F. Abild-Pedersen, J.K. Nørskov, J.R. Rostrup-Nielsen, J. Sehested, S. Helveg, Physical Review B 73 (2006) 115419.
[16] T. Aaltonen, M. Ritala, T. Sajavaara, J. Keinonen, M. Leskela¨, Chemistry of Materials 15 (2003) 1924-1928.
[17] Y. Zhou, D.M. King, X. Liang, J. Li, A.W. Weimer, Applied Catalysis B: Environmental 101 (2010) 54-60.
[18] J. Li, X. Liang, D.M. King, Y.-B. Jiang, A.W. Weimer, Applied Catalysis B: Environmental 97 (2010) 220-226.

[19] W. Setthapun, W.D. Williams, S.M. Kim, H. Feng, J.W. Elam, F.A. Rabuffetti, K.R. Poeppelmeier, P.C. Stair, E.A. Stach, F.H. Ribeiro, J.T. Miller, C.L. Marshall, The Journal of Physical Chemistry C 114 (2010) 9758-9771.
[20] W. Kessels, H. Knoops, S. Dielissen, A. Mackus, M. van de Sanden, Applied Physics Letters 95 (2009) 013114-013114-013113.
[21] X. Liang, L. Lyon, Y.-B. Jiang, A. Weimer, Journal of Nanoparticle Research 14 (2012) 1-12.
[22] S.T. Christensen, H. Feng, J.L. Libera, N. Guo, J.T. Miller, P.C. Stair, J.W. Elam, Nano Letters 10 (2010) 3047-3051.
[23] Y. Lei, B. Liu, J. Lu, R.J. Lobo-Lapidus, T. Wu, H. Feng, X. Xia, A.U. Mane, J.A. Libera, J.P. Greeley, J.T. Miller, J.W. Elam, Chemistry of Materials 24 (2012) 3525-3533.
[24] A.J.M. Mackus, N. Leick, L. Baker, W.M.M. Kessels, Chemistry of Materials 24 (2012) 1752-1761.
[25] T.D. Gould, A.M. Lubers, B.T. Neltner, J.V. Carrier, A.W. Weimer, J.L. Falconer, J. Will Medlin, Journal of Catalysis 303 (2013) 9-15.
[26] D.M. King, J.A. Spencer Ii, X. Liang, L.F. Hakim, A.W. Weimer, Surface and Coatings Technology 201 (2007) 9163-9171.
[27] D. Baudouin, U. Rodemerck, F. Krumeich, A.d. Mallmann, K.C. Szeto, H. Ménardd, L. Veyre, J.-P. Candy, P.B. Webb, C. Thieuleux, C. Copéreta, Journal of Catalysis 297 (2013) 27-34.
[28] A. Olafsen, C. Daniel, Y. Schuurman, L. Råberg, U. Olsbye, C. Mirodatos, Catalysis Today 115 (2006) 179-185.
[29] T.D. Gould, M.M. Montemore, A.M. Lubers, A. Weimer, J.L. Falconer, J.W. Medlin, Submitted to Journal of Catalysis (2013).
[30] N. İnoğlu, J.R. Kitchin, Journal of Catalysis 261 (2009) 188-194.
[31] D. Sun, Y. Zhao, H. Su, W. Li, Chinese Journal of Catalysis 34 (2013) 1434-1442.
[32] A. Olafsen, Ã. Slagtern, I.M. Dahl, U. Olsbye, Y. Schuurman, C. Mirodatos, Journal of Catalysis 229 (2005) 163-175.
[33] D. Baudouin, K.C. Szeto, P. Laurent, A. De Mallmann, B. Fenet, L. Veyre, U. Rodemerck, C. Copéret, C. Thieuleux, Journal of the American Chemical Society 134 (2012) 20624-20627.
[34] C.H. Bartholomew, Applied Catalysis A: General 107 (1993) 1-57.
[35] J. Sehested, Journal of Catalysis 217 (2003) 417-426.
[36] R.T.K. Baker, Carbon 27 (1989) 315-323.
[37] E.F. Kukovitsky, S.G. L'Vov, N.A. Sainov, V.A. Shustov, L.A. Chernozatonskii, Chemical Physics Letters 355 (2002) 497-503.
[38] A. Tanksale, J.N. Beltramini, J.A. Dumesic, G.Q. Lu, Journal of Catalysis 258 (2008) 366-377.
[39] S.A. Tupy, A.M. Karim, C. Bagia, W. Deng, Y. Huang, D.G. Vlachos, J.G. Chen, ACS Catalysis 2 (2012) 2290-2296.
[40] L.M. Aparicio, Journal of Catalysis 165 (1997) 262-274.
[41] A.K. Avetisov, J.R. Rostrup-Nielsen, V.L. Kuchaev, J.H. Bak Hansen, A.G. Zyskin, E.N. Shapatina, Journal of Molecular Catalysis A: Chemical 315 (2010) 155-162.
[42] W. Erley, H. Wagner, Surface Science 74 (1978) 333-341.
[43] F. Pompeo, N.N. Nichio, M.M. Souza, D.V. Cesar, O.A. Ferretti, M. Schmal, Applied Catalysis A: General 316 (2007) 175-183.

[44] E. Nikolla, A. Holewinski, J. Schwank, S. Linic, Journal of the American Chemical Society 128 (2006) 11354-11355.

4.8. Supplemental Information

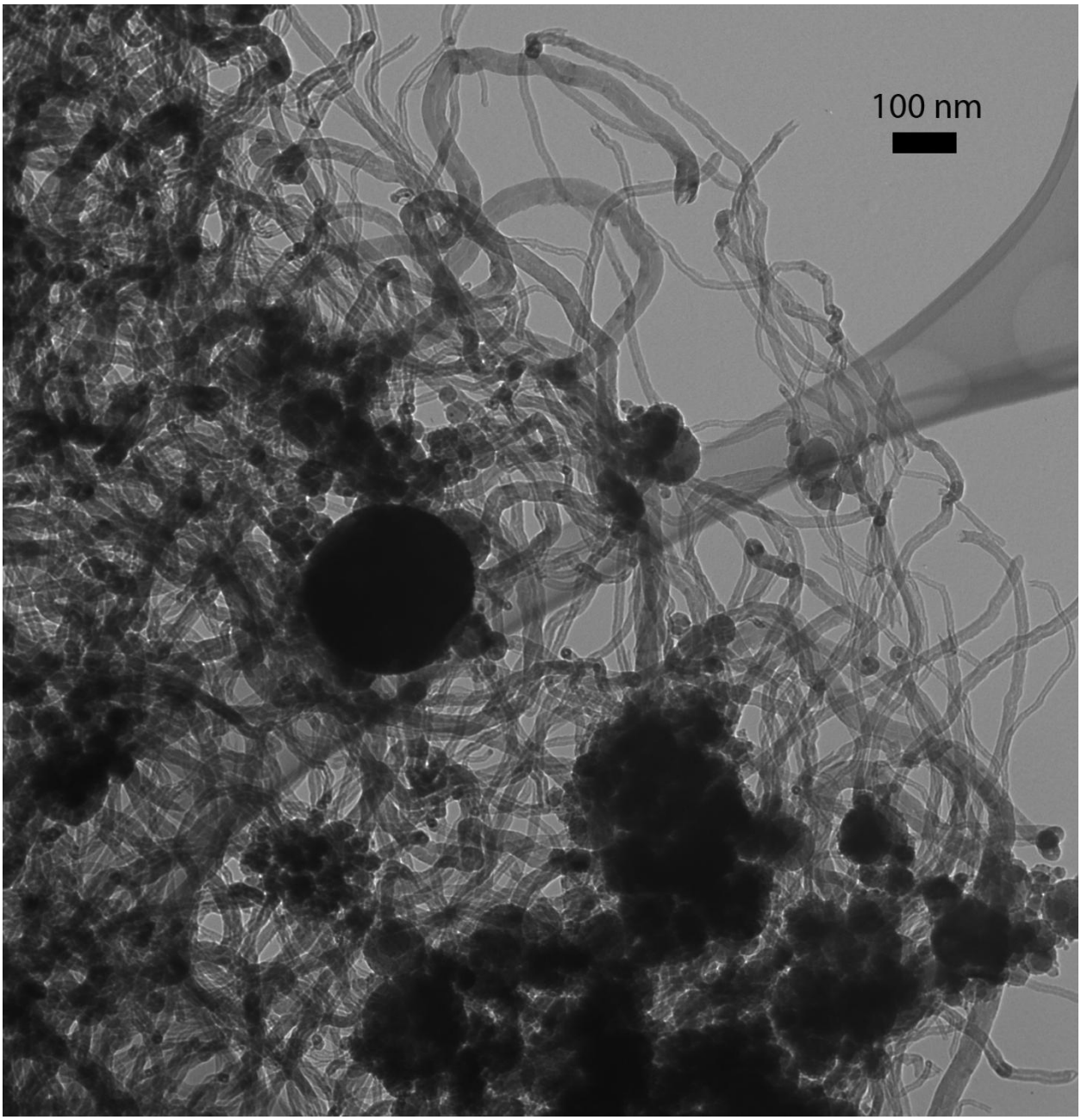

Figure 4.S1. TEM image of Ni ALD particles (pre-sintered for 24 h in 50% H_2 at 873 K) after 10-h DRM reaction time. The catalyst contains a large number of carbon whiskers.

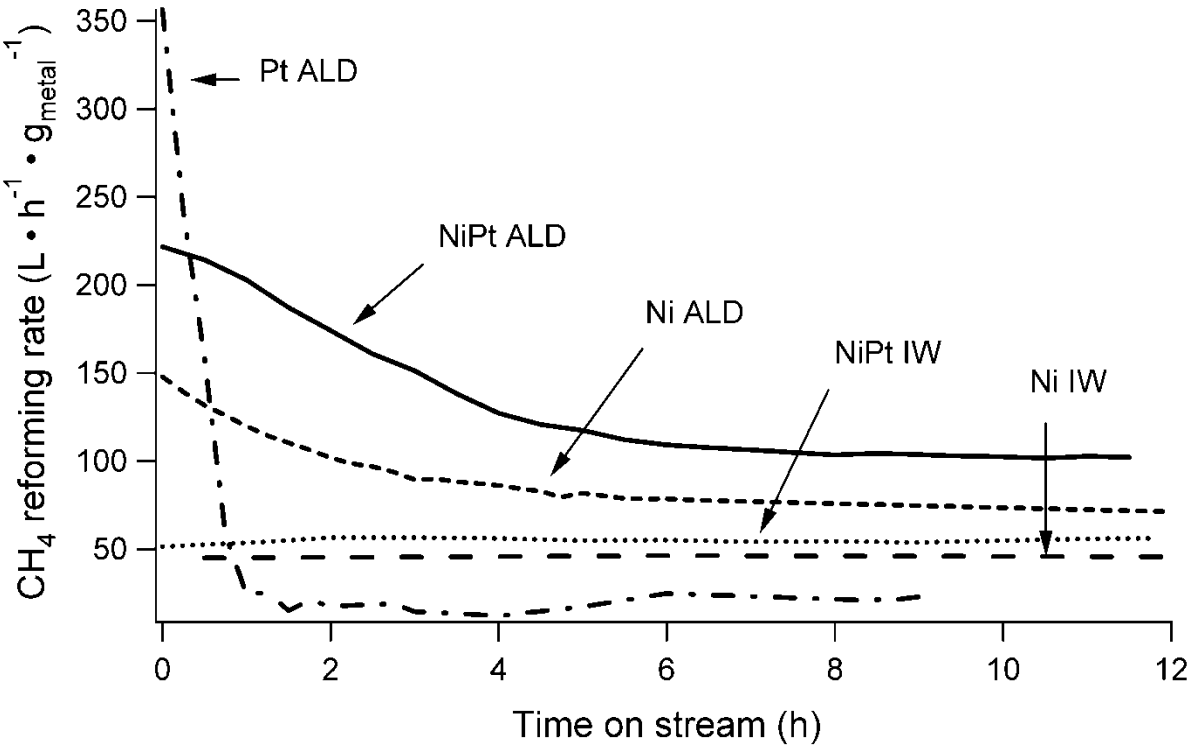

Figure 4.S2. Dry reforming rates at 873 K during first 10 h of reaction for all catalysts investigated.

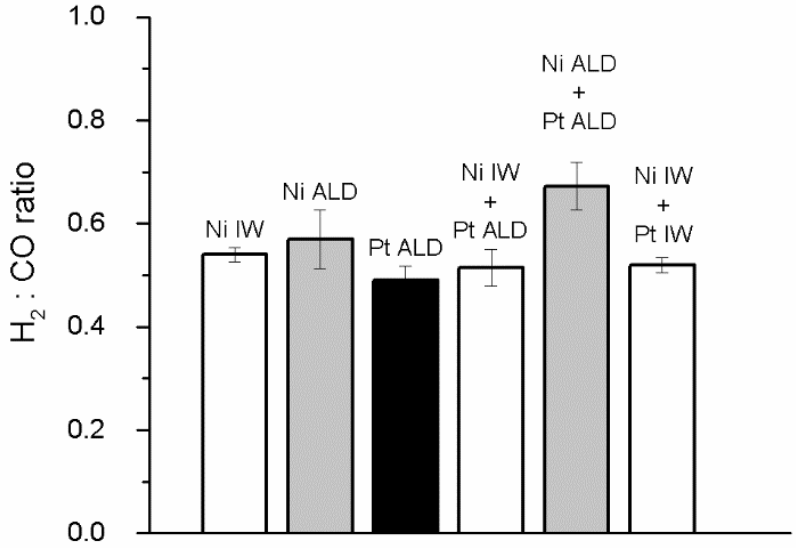

Figure 4.S3. Steady-state H_2:CO ratios for all catalysts investigated during DRM at 873 K.

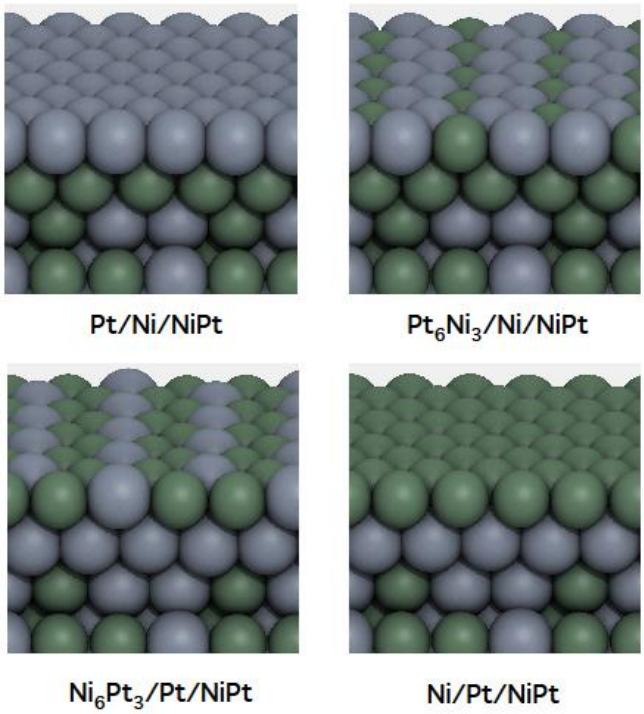

Figure 4.S4. Four NiPt alloys used in the DFT studies. All have a NiPt mixed alloy for the bottom two layers, with a Ni/Pt ratio of 1:1.

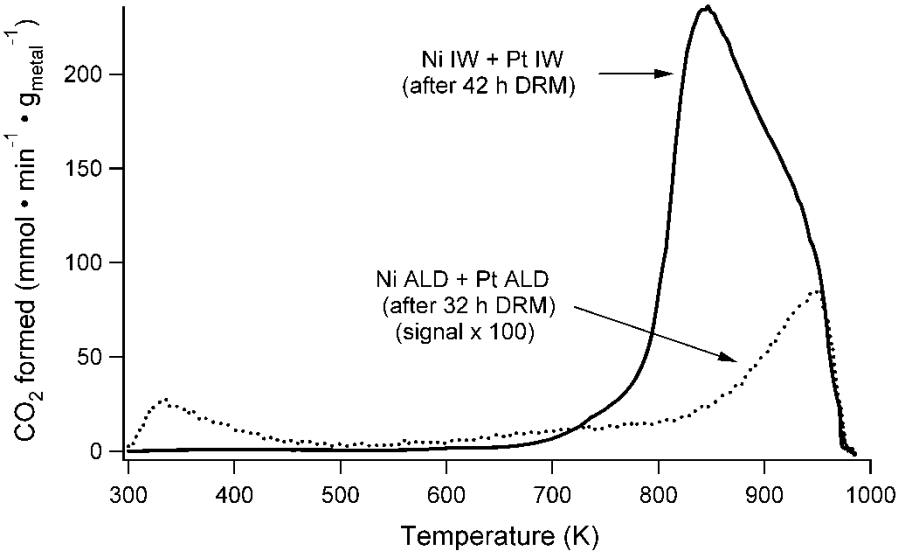

Figure 4.S5. Carbon dioxide formed during temperature-programmed oxidation of NiPt catalysts after DRM at 873 K

5. Stabilizing Ni Catalysts by Molecular Layer Deposition of Porous Aluminum Oxide

5.1. Abstract

Sintering is a major problem for catalysts used in dry reforming of methane (DRM). This study inhibited sintering of ~ 2 – 5 nm Ni particles synthesized via atomic layer deposition (ALD) by stabilizing the catalysts with an alucone molecular layer deposition (MLD) coating. This coating was synthesized using a three-step "ABC" reaction of trimethyl aluminum (TMA), ethyl amine (EA), and maleic anhydride (MA). The particles were coated with 5, 10 or 15 cycles of MLD and then calcined to form a porous alumina over-layer. Calcining the catalysts at 773 K produced a stable catalyst, but the catalyst calcined at 673 K rapidly deactivated during dry reforming of methane (DRM). The catalysts' stability during DRM at 973 K was measured, and the particle sizes were measured after reaction by TEM. The uncoated catalyst continuously deactivated with time on stream, whereas for the MLD-coated catalysts, the DRM rates increased during the first few hours on-stream before stabilizing, apparently because the nickel surface area increased. Active metal surface area increased with higher reduction temperature for the MLD-modified catalysts, whereas the nickel surface area decreased for uncoated catalysts due to sintering. Particle sizes measured by TEM after reaction were smaller for the MLD-modified catalysts. After repeated DRM at 973 K, calcination, and reduction in H_2, the 10-cycle MLD catalyst returned to the same steady-state DRM rate. Coking on the 5-cycle MLD-coated catalyst from the DRM reaction was approximately half that of the uncoated catalyst.

5.2. Introduction

Methane reforming has received much attention in the last decade due to increased recovery of shale gas from enhanced fracking technologies. The current surplus of natural gas has provided motivation for using CH_4 for chemical synthesis of fuels and chemicals, in addition to using CH_4 for electricity and heat production, especially in the case of "stranded" gas-fields at remote wells.[1] The primary chemical process utilizing CH_4 is methane steam reforming (MSR), and in 2012 it produced 95% of the US H_2 supply.[2] Another reforming reaction, dry reforming of methane (DRM): $CO_2 + CH_4 \rightarrow 2CO + 2H_2$, is used much less due to its lower H_2:CO ratio (typically less than 1) and exacerbated problems with deactivation from coking in the absence of steam.[3-5] However, with the growth of synthetic fuel production through Fischer-Tropsch (FT) synthesis of syngas,[6] DRM can prove a valuable reaction to blend streams with those from MSR to produce syngas feed streams with desired H_2:CO ratios.[3, 5, 7]

Supported Ni, which is the primary catalyst used for CH_4 reforming, deactivates due to coking and sintering.[4, 7-9] Coke formation can be thermodynamically limited by running the reactions at high temperatures,[3] but high-temperature operation is energy intensive and also sinters the catalyst, which reduces activity. Catalyst coking can be decreased without high temperatures by incorporating promoters or a second catalytic metal. Bengaard et al. demonstrated that K, S, and Au preferentially bind to Ni step edges to act as site blockers for carbon nucleation.[10] Bimetallic Ni-Pt catalysts also have higher coking resistance than monometallic Ni catalysts,[11-13] due to the lower solubility of C in Pt, higher C diffusion barriers on bimetallic surfaces, and weaker C adsorption energies at bimetallic step sites.[14, 15] Coking can also be decreased by using smaller Ni particles because their step edges are small enough to limit carbon nucleation and subsequent growth.[10] Maintaining small particles

during the DRM reaction is difficult, however, because reforming conditions readily sinter Ni particles.

Approaches for mitigating catalyst nanoparticle sintering have received much attention in recent years for a variety of catalysts. Atomic layer deposition (ALD) has been used to create barriers that inhibit diffusion of supported catalyst particles.[16] Alumina ALD was used as an overcoating to protect Pd nanoparticles, by either depositing less than a monolayer (less than 16 alumina ALD cycles) on the Pd catalyst,[17] or by depositing a thicker coating (8 nm with 40 ALD cycles), which was then cracked to create pores.[18] The cracked-alumina ALD layers prevented sintering at 948 K for 28.3 h during oxidative dehydrogenation of ethylene. Both the porous sub-monolayer alumina and the cracked alumina layers blocked step and defect sites on the Pd catalysts. Site-blocking can shut down unfavorable reactions that occur on those sites,[18] but it would also decrease the DRM activity because those step sites dominate the reaction rate.[10, 15] Bengaard et al. showed that when step sites were blocked by K on a $Ni/MgAl_2O_4$ catalyst, the activation energy for dissociative CH_4 adsorption was 36.1 kJ/mol higher than the normal $Ni/Mg/Al_2O_4$ catalyst, and their theoretical calculations showed the CH_4 activation energy was 19 kJ/mol higher on Ni(111) than Ni(211).[10] Alternatively, metal ALD can be augmented with a third chemistry to deposit inert material around catalyst particles in a three-step ALD process. This "ABC" ALD utilizes protecting ligands (e.g., alkanethiols, ethylenediamine, acetonitrile) on the metal particles while a stabilizing metal oxide is deposited around the particle.[16, 19] The protecting ligands are then removed and the metal particles are trapped by the oxide, which can limit coalescence during particle synthesis. However, this technique has not been shown to stabilize catalyst particles under reaction conditions or at high temperatures, but only limit the size of the particles deposited.

Catalysts can also be stabilized by molecular layer deposition (MLD), which is analogous to ALD, but it deposits hybrid polymer-metal thin films in sequential self-limiting reactions. These hybrid layers are then calcined (or water-etched) to remove the organic component and leave a residual porous inorganic framework. An example of an MLD layer is aluminum alkoxide (alucone), which is deposited by alternating half-cycles of trimethyl aluminum (TMA) and ethylene glycol (EG). Liang et al. used this "AB" alucone MLD layer to stabilize Pt-ALD catalyst nanoparticles.[20] They reported that when the polymeric layer was calcined, the resultant porous matrix had 0.6-nm diameter pores. These porous layers inhibited sintering of the Pt particles during calcination at 673, 873, and 1073 K for 4 h. Although the MLD layers inhibited sintering, they also decreased the Pt surface area and therefore decreased the catalytic activity for CO oxidation. The decreased activity was also likely due to mass transfer limitations in the 0.6-nm pores, and possibly due to restructuring of the porous matrix to crystalline alumina in the sample that was calcined at 1073 K.[20, 21]

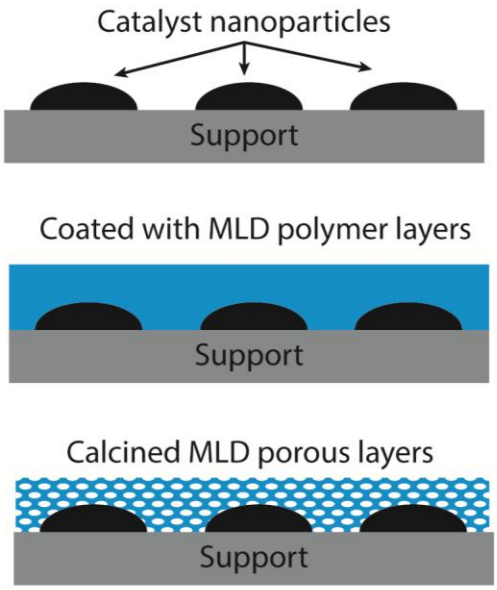

Scheme 5.1 Schematic representation of depositing metal nanoparticles, coating these particles with MLD layers, and calcining the catalyst to remove the organic to form a porous alumina layer.

Liang et al. created larger-pore MLD layers on spherical silica particles using "ABC" chemistry with larger organic molecules (~0.85-nm total organic length per cycle for ABC alucone MLD compared to ~0.15-nm organic length for AB alucone MLD).[22] This ABC chemistry uses TMA, ethyl amine (EA), and maleic anhydride (MA) to create a thicker alucone layer with a higher fraction of organic matter in the layer than AB alucone MLD.[23, 24] After calcination, Liang reported that pores formed with a 0.8-nm average diameter to create a stabilizing porous matrix, as depicted in Scheme 5.1. The present study uses this ABC alucone MLD to stabilize Ni nanoparticles that were synthesized by ALD. The uncoated catalysts lost activity through sintering and coking, and this study shows that the MLD layers inhibited sintering and coking, and the effect depended on the number of MLD cycles. The effect of these MLD layers on DRM catalytic activity is also presented. The MLD coatings altered the catalyst behavior; instead of decreasing over time, the activity increased on the MLD-modified catalysts until a steady-state DRM rate was achieved. The MLD-coated catalysts reached steady state

faster than the uncoated catalyst, had less coke deposition during the reaction, and in the case of 5-MLD cycles, had a higher DRM rate than the uncoated sample. The MLD layers stabilized the Ni particles, which sintered less than the uncoated catalyst.

5.3. Experimental Methods

5.3.1 Catalyst preparation

The Ni catalyst nanoparticles were deposited by ALD at 673 K in a fluidized-bed reactor (FBR) as described previously,[25] but using approximately 0.25 g of the Ni precursor ($NiCp_2$) to deposit less Ni. Approximately 2 g of precursor are needed to react with all available active sites on the support. This would deposit the maximum amount of Ni metal in one ALD cycle, but here less precursor was used in order to obtain a lower Ni weight loading. Nitrogen flowed over the solid Ni ALD precursor and transported the precursor vapor to the FBR. Alumina nanoparticles (< 50-nm γ-alumina spheres, ~ 37 $m^2 \bullet g^{-1}$ surface area, Aldrich 544833) were used as the catalyst support because alumina is a common support for DRM reactions, and because imaging nanoparticles by TEM on these supports required no cross-sectioning or dispersion on the TEM grids (aside from electrostatic adherence). All the catalysts were synthesized from the same 5-g batch of ALD catalyst. Approximately 1 g was removed from the batch for characterization of the uncoated catalyst and the rest was coated with MLD layers. After each set of 5 MLD coatings, 1 g of the sample was removed from the FBR, and the remaining sample was left in the reactor for further MLD coating. The catalyst was coated by alucone MLD at 450 K with ABC chemistry (TMA, EA, MA).[22] Each MLD cycle consisted of a 30- to 60-min precursor dose, followed by a 30-min purge with N2 and a 30-min evacuation between precursor doses (repeated for each of the ABC precursors).

5.3.2 Catalyst characterization

The weight loadings of each sample were determined by inductively coupled plasma mass spectroscopy (ICP-MS) after the samples were dissolved in an $HF/HNO_3/HCl$ solution for approximately 24 h. The number of active sites was measured by H_2 uptake with a Quantachrome AS-1 Autosorb. The catalysts were calcined in air at 773 K for 1 h in a tubular furnace (Lindberg heavy duty type 59754), then reduced at 773 K (unless otherwise specified) in pure H_2 for 1 h in the Autosorb before measuring the H_2 uptake. Transmission electron microscopy (TEM) was used to estimate Ni particle sizes. Particles were measured using Image J software to analyze images from an FEI Tecnai 12 - Spirit Biotwin TEM and a Phillips CM-100 TEM. Samples were electrostatically adhered to copper grids with a lacey carbon over-layer (Ted-Pella 01895 Lacey Carbon Film grids) to avoid effects of solvents from dropcasting.

The catalysts were characterized by temperature-programmed oxidation (TPO) in a quartz tube reactor (6.35-mm inner diameter) at ramp rates of 60 K/min, and the effluent from the reactor was analyzed with an SRS RGA 200 mass spectrometer. The catalysts were cooled to room temperature from 973 K under Ar flow after the DRM reaction was stopped, and then a stream of 10 sccm O_2 and 40 sccm Ar was flowed over the catalyst at room temperature. The temperature was then ramped while the CO_2 production rate was measured with the mass spectrometer.

5.3.3 Reaction studies

The catalysts were evaluated for DRM activity in a quartz tube, packed bed reactor (6.35-mm ID). The catalysts were first oxidized for 1 h at 773 K in 100 sccm 20% O_2 (balance Ar) to remove the organic components of the MLD layer and create a porous alumina matrix as depicted in Schematic 5.1. The uncoated catalysts were also oxidized so that all catalysts went

through the same pretreatment procedure. The catalysts were then reduced at 773 K for 1 h in 100 sccm 20% H_2 (balance Ar). All catalysts were heated to 973 K and held at that temperature for approximately 10 min before the reactants were introduced to the reactor. Effluent gases were analyzed by a SRI 8610c GC with a Haysep-D packed column. Gas flow rates were 20 sccm CH_4, 20 sccm CO_2, and 60 sccm Ar. Approximately 80 mg of catalyst was used for catalytic testing. At the end of the reaction time, the reactant flow was stopped and replaced by inert carrier gas before cooling the catalysts in order to avoid additional carbon deposition as the reactor cooled.

5.4. Results and Discussion

5.4.1. MLD Layer Deposition & Preparation

Nickel nanoparticles were deposited by ALD on an alumina support for testing the effectiveness of MLD layers at preventing sintering. One ALD cycle was used to create small metal particles. The weight loadings of the catalysts were kept below 0.8 Ni wt% to limit sintering. The average Ni particle size was difficult to accurately measure by TEM due to their small size (~2 to 5 nm, see Figure 5.1), but H2 chemisorption estimated the average uncoated Ni particle diameter to be ~5.3 nm (after 1-h calcination at 773 K followed by 1-h reduction at 773 K, which likely induced some sintering).

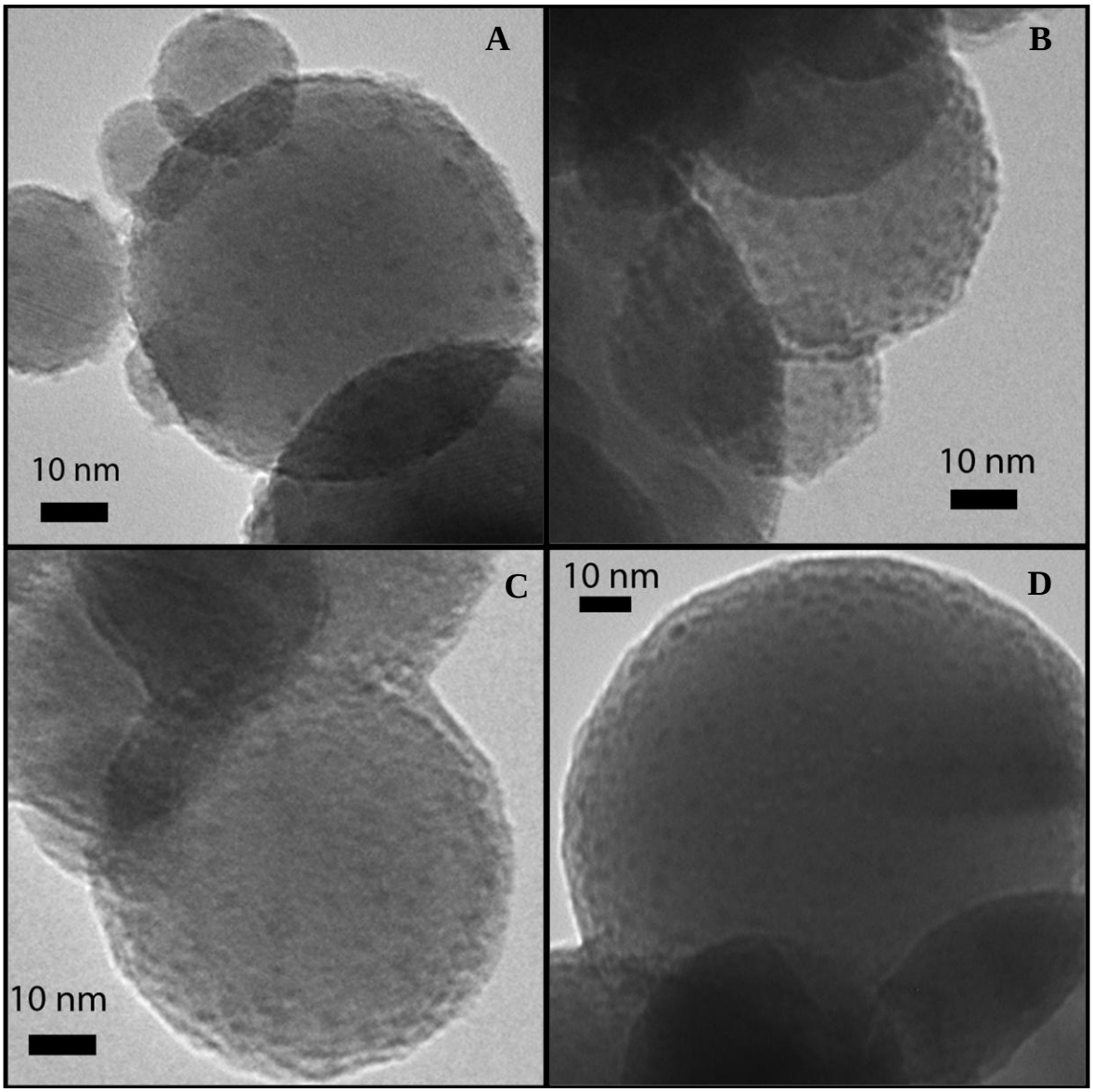

Figure 5.1. A) Ni nanoparticles (~2-5 nm dark particles) deposited on spherical alumina; Ni/Al_2O_3 nanoparticles coated by B) 5-MLD cycles, C) 10-MLD cycles, D) 15-MLD cycles, where the hybrid polymer-inorganic MLD layer is the lighter layer encompassing the spheres in B-D.

The ALD catalysts were coated with alucone using 5, 10 and 15 ABC MLD cycles. As shown in Figure 5.1, these coatings did not significantly change the Ni particle size, and ICP-MS indicated that the alumina MLD layers did not significantly alter the metal weight loadings. The coating measured by TEM for 15-MLD cycles was thicker (3.5 +/- 0.5 nm) than the 10-cycle layer (2.4 +/- 0.5 nm), as expected, but the 5-MLD cycle layer was too thin to measure.

Chemisorption measurements were initially performed after pretreating the catalysts (which were previously calcined at 773 K) by reducing the samples for 1 h in pure H_2 at 773 K. Hydrogen uptake (Figure 5.2) was then measured for the same catalyst samples after reduction at 873 K and 973 K. As expected, the uncoated catalyst lost surface area (due to sintering) with successive reductions at higher temperatures. In contrast, the MLD-coated catalysts increased H_2 uptake with increasing reduction temperature. The increase in active metal with reduction temperature is atypical, and is likely due to both reduction of NiO under the MLD film, and pore expansion within the MLD film so as to uncover more metal surface area. Further reduction of the 10 and 15 MLD-cycle catalysts at 973 K did not increase the H_2 uptake (Figure 5.2), but further reduction (two 1-h treatments at 973 K) increased the H_2 uptake of the 5-MLD sample from 6.0 +/- 0.5 to 8.1 +/- 0.2 μmol H2 • gcat-1. The 10 and 15 MLD-cycle samples had similar H_2 uptake after reduction at 973 K (i.e., once the maximum number of sites were made available), which indicates that adding more MLD cycles to the 10-MLD cycle catalyst did not block additional sites once the catalysts had been reduced at 973 K. In contrast, increasing from 5 to 10-MLD cycles increased the number of sites blocked by the MLD layer, even after reduction at 975 K. Although the 15-MLD cycle catalyst had an unexpected higher H_2 uptake at lower temperatures than the 10-MLD cycle catalyst, this difference most likely came from the 15-MLD cycle sample being left in ambient conditions for 1 month longer than the other samples (water vapor is known to start opening pores in uncalcined MLD layers[22]).

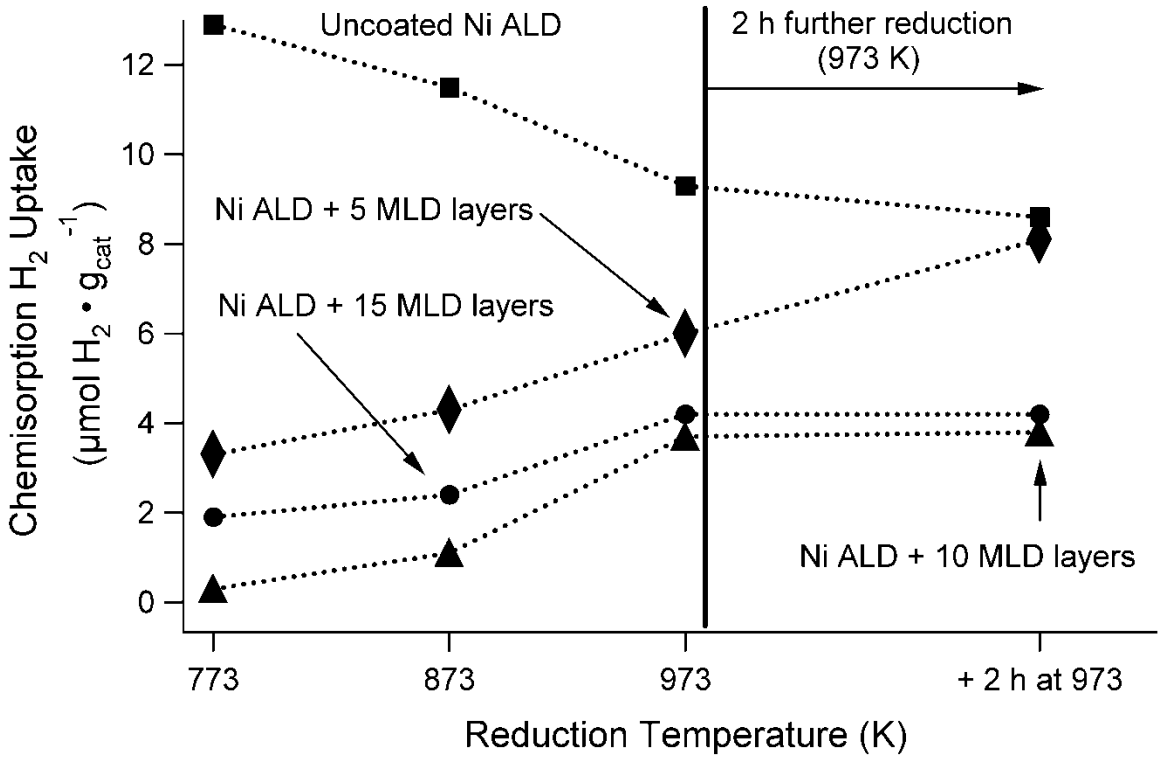

Figure 5.2.Chemisorption H_2 uptake on metal Ni sites after different reduction temperatures for the uncoated Ni ALD catalyst and catalysts modified by 5, 10, and 15 MLD layers. The size of the markers shown above are approximately equal to the measurement error.

Before using the MLD-modified catalysts in the DRM reaction, the hybrid organic-metal layer was calcined in 20% O_2. Liang et al. effectively removed the organic components of the AB chemistry MLD layers by calcination at 673 K to create the porous matrix over Pt ALD catalysts or bare alumina supports.[20, 22] However, when this calcination temperature (673 K) was used for the ABC chemistry MLD layers reported here, the catalyst deactivated rapidly (see Figure 5.3 for the 10-MLD cycle catalyst), much quicker than the uncoated catalyst. Temperature-programmed oxidation (in Supplemental Information Figure 5.S1) showed that a small fraction of organic material remained until ~773 K. When the catalyst was calcined at 773 K, however, the rate was low, but it increased with time and after 5 h surpassed the rate on the sample calcined at 673 K, as shown in Figure 5.3 for the 10-MLD sample. When the catalyst was

calcined at 673 K, the Ni metal was likely more reduced initially, and thus had a higher DRM rate initially. However, organic components remained in the MLD layer because of the milder oxidation temperature and likely blocked pores and may have coked the catalyst surface more than normal reaction conditions. Calcining at 773 K yielded approximately the same steady-state DRM rate as a TPO up to 973 K, so for all subsequent reactions, the organic components of the MLD layer were removed by calcination at 773 K.

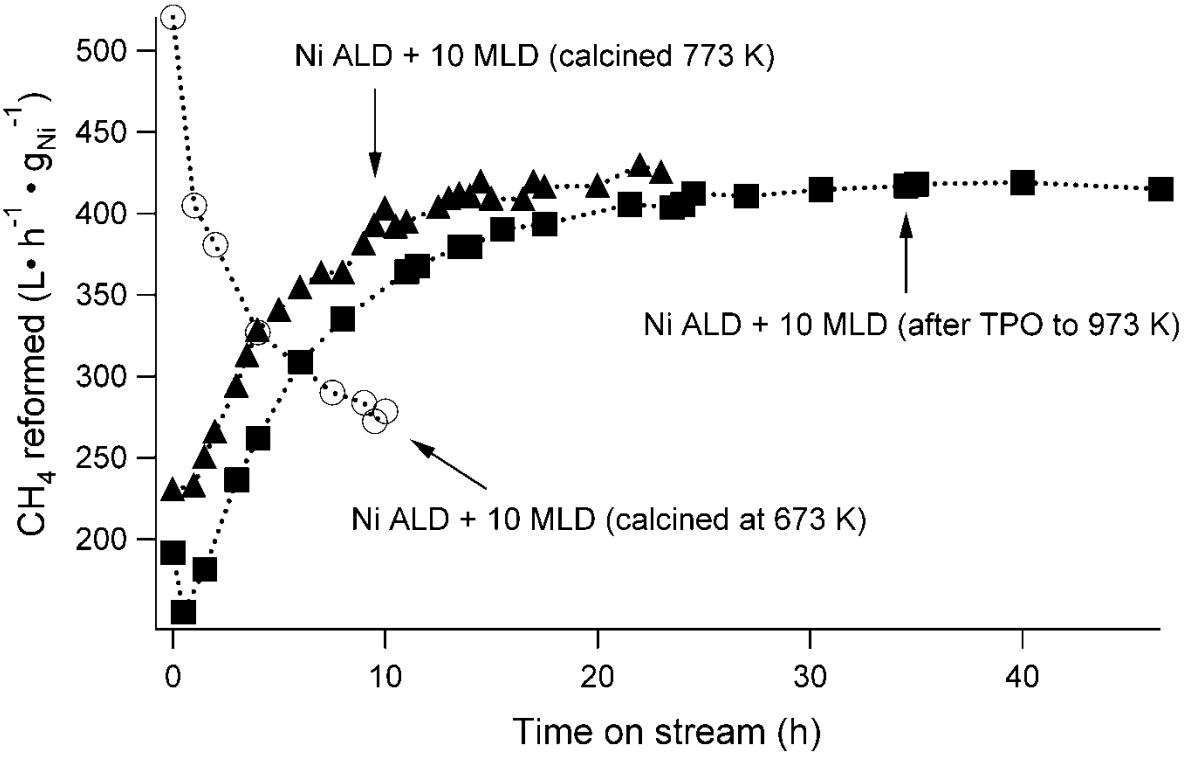

Figure 5.3. Methane dry reforming rate of the Ni ALD catalyst modified with 10 ABC MLD layers for varying calcination treatments used to remove the organic components from the MLD layers.

5.4.2. Catalyst evaluation for DRM stability and activity

The catalysts were evaluated for dry reforming activity and stability to gauge the effectiveness of the MLD layers at reducing sintering and maintaining catalytic activity. The DRM rates increased over time when the catalysts were modified with MLD layers (Figure 5.3),

but the uncoated catalyst activity decreased over time (Figure 5.4) due to sintering and coking (which is typically observed for catalysts of this size during DRM at these temperatures [26, 27]). The DRM reaction was run at 973 K to increase sintering and to determine the effectiveness of MLD at preventing sintering.

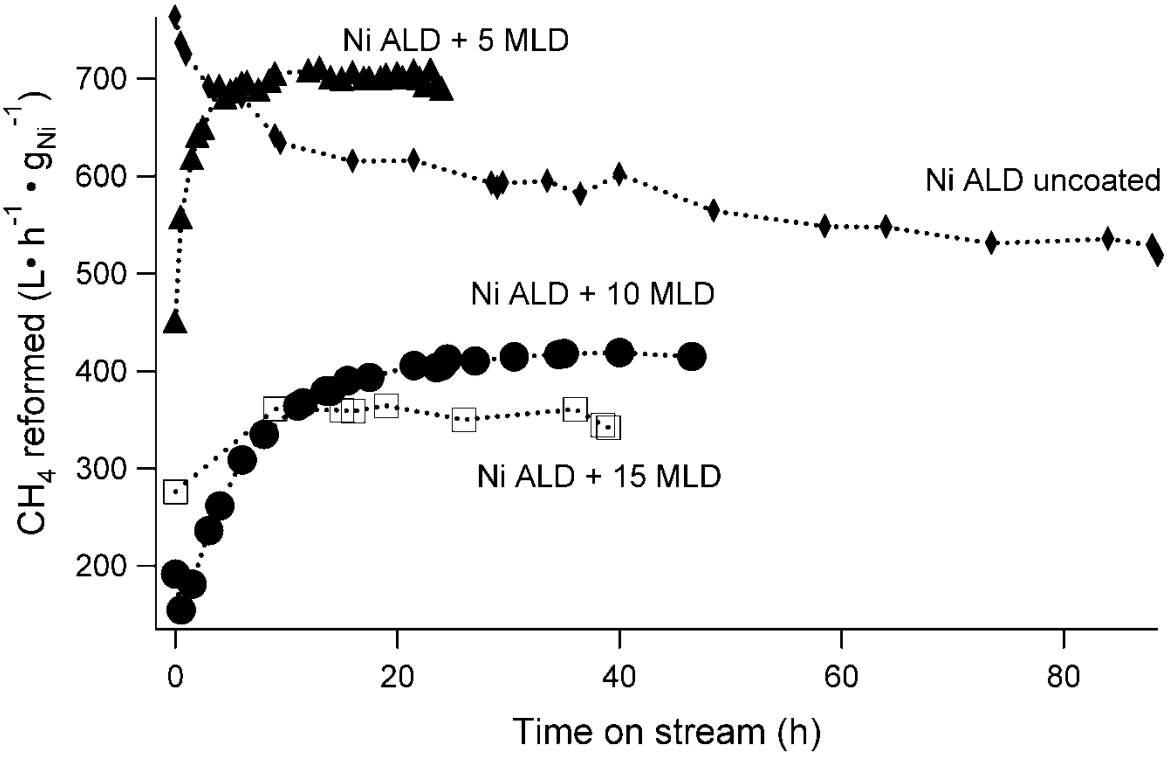

Figure 5.4. Dry reforming rates at 973 K for uncoated Ni ALD catalyst, and the same catalyst coated with 5, 10, and 15 MLD layers.

A shown in Figure 5.4, the catalyst with 5-MLD layers reached steady state fastest, and the steady-state DRM rate decreased as the number of MLD cycles increased. Adding 5 MLD layers not only stabilized the catalyst, but its steady-state rate was higher than that of the uncoated catalyst after 6 h. The rate most likely increased with time because the Ni surface area increased, either due to expansion of the alumina pores or reduction of NiO. To determine if surface area increased solely from pore expansion, a previously-calcined, 10-cycle MLD sample (1 h at 773 K) was reduced at 773 K for 1 h. The H_2 uptake for this sample was below the

detection limit. The catalyst was then held at 973 K in He for 4 h to potentially open more pores, but after reducing again at 773 K, this sample had negligible H_2 uptake. Holding the porous layer at high temperature alone could not account for the surface area increase, and therefore the surface area likely increased because the NiO (or $NiAl_2O_4$) was reduced at higher temperatures, or by reducing the catalyst with simultaneous pore expansion.

The DRM rate increased with time when the 10-MLD layer catalyst was oxidized and reduced at 773 K the first time, but when that same catalyst was oxidized and reduced again (1 h each treatment at 773 K), the opposite behavior was observed; the rate decreased with time (likely due to coking) before stabilizing at the same rate as before. Subsequent calcination and reduction of the catalyst yielded the same result, indicating that the 10-MLD layer catalyst could be regenerated and was stable for DRM. The 10-MLD cycle catalyst was also reduced at 973 K, instead of 773 K, before running the DRM reaction to determine if the activation period could be bypassed by reducing at a higher temperature. The DRM rate, shown in Supplemental Information Figure 5.S2, was similar to that of the regenerated 10-MLD cycle catalyst; the reaction rate decreased over time before stabilizing. The rate also decreased with time when the 5-MLD cycle catalyst was calcined and reduced again, as shown in Figure 5.5, but the steady-state rate was 22% lower than the fresh catalyst. Moreover, a second calcination and reduction resulted in a slightly lower rate. Although this sample was stable and more active for the DRM reaction after the initial pretreatment, the thinner MLD layer likely decomposed further during calcination and reduction so that the Ni particles sintered further. The twice-regenerated 5-MLD cycle catalyst had an average Ni particle size of 8.4 +/- 2.9 nm, which was larger than the 6.8 +/- 2.1 nm average particle size of the fresh catalyst after 24 h of reaction.

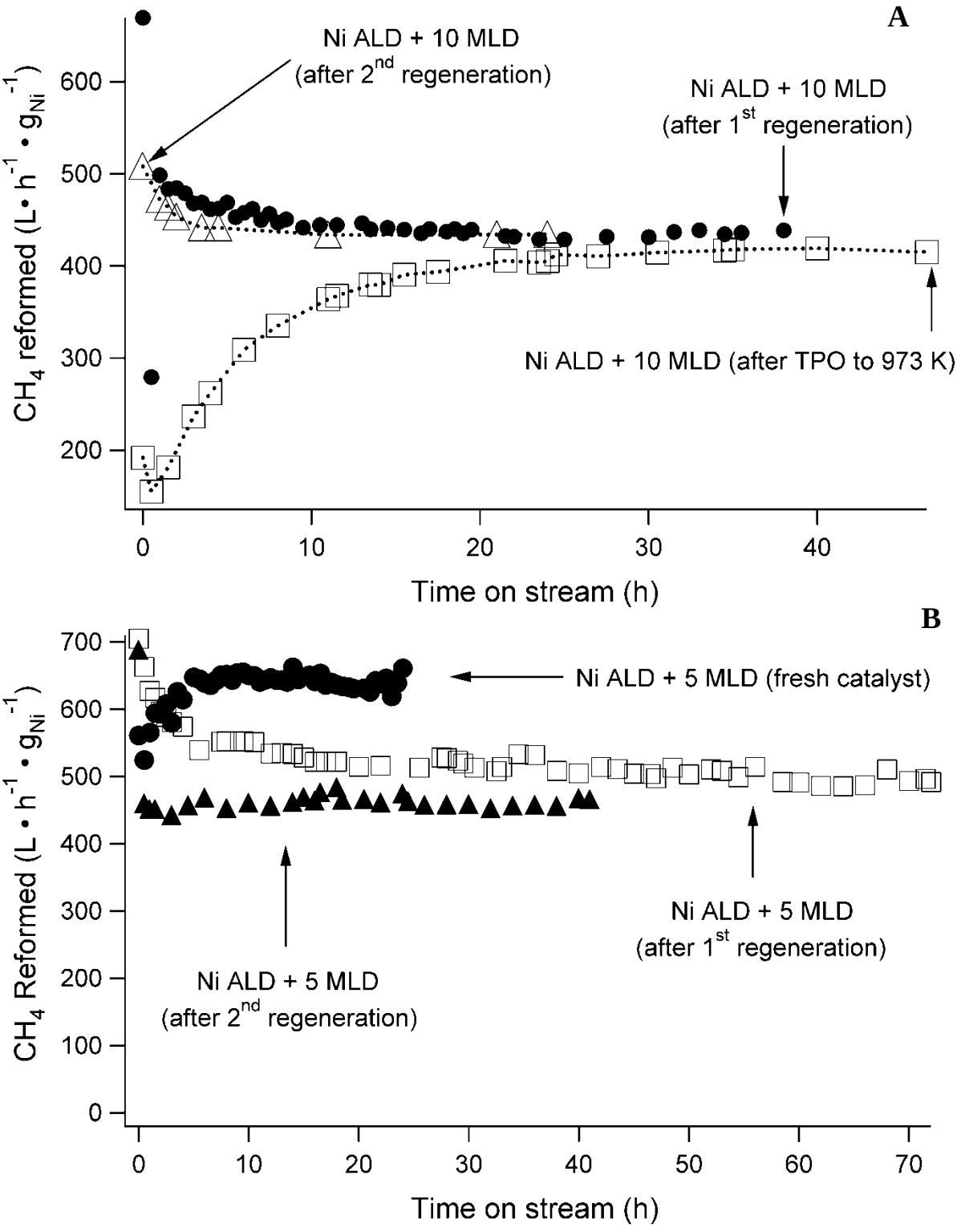

Figure 5.5. Effect of oxidizing and reducing 1 h each at 773 K on DRM rate over time on A) Ni ALD catalyst modified with 10 MLD layers, B) Ni ALD catalyst modified with 5 MLD layers.

The Ni particles sintered during DRM, as measured by TEM (Figure 5.6), but the uncoated catalyst sintered the most; it had a post-reaction particle size of 9.7 +/- 3.9 nm after 82 h of reaction. Coating the catalysts with 5-MLD cycles reduced sintering (Ni particle size after 24 h of reaction was 6.8 +/- 2.1 nm and after 2 regenerations was 8.4 +/- 2.9 nm). The 10-cycle catalyst sintered the least (Ni particle size after 108-h total reaction time and 2 regenerations was 7.8 +/- 3.5 nm). The standard deviation of particle size was also smaller for the 5 and 10-cycle catalysts, and the distribution of particle sizes (Supplemental Figure 5.S3) showed more particles in the sub 5-nm range than the uncoated catalyst and fewer particles that were > 15 nm. The wider range of particle sizes in the uncoated sample is likely due to a higher degree of Ostwald ripening, where metal atoms desorb from smaller particles and then adsorb on larger particles to minimize particle surface energy. Measuring the size of particles on the 15-MLD cycle sample after reaction was difficult because of difficulties distinguishing the calcined MLD layer from individual Ni particles.

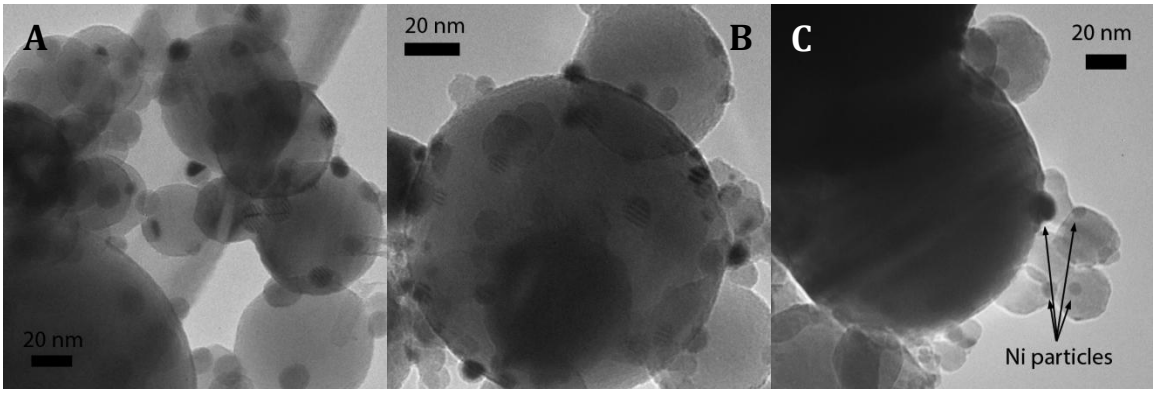

Figure 5.6. TEM images of post-reaction Ni catalysts on spherical alumina supports: (A) uncoated sample after 82-h DRM reaction, (B) coated with 5-MLD layers after 24-h reaction, (C) coated with 10-MLD cycles after 108-h total time on stream and 2 regenerations

Although reduced sintering was the main focus of this study, another benefit of small particle size is less coking.[10] Bengaard et al. showed, using thermogravimetric analysis, that 7-nm Ni particles had a 100-K higher coking onset temperature than ~100-nm Ni particles and

the smaller Ni particles coked at a much slower rate.[10] Previous work on a 6 wt% Ni IW catalyst (~17-nm particles)[28] and other studies have shown that the large Ni particles readily form carbon whiskers [14, 25], whereas carbon whiskers were not detected for any of the ALD catalysts used in this study. The amount of carbon deposited during DRM reactions was measured by TPO. The Ni ALD particles are less susceptible to coking than most Ni catalysts due to their small size, but as shown in Figure 5.7, adding MLD layers to the catalyst decreases coking during DRM. Not only does the MLD layer prevent sintering, but maintaining the small particle size also inhibits coke deposition. The CO_2 formed at a much lower temperature on the 15-cycle catalyst than the other two. This lower temperature peak is indicative of a less-stable carbon type, which could be due to a smaller available Ni ensemble size caused by the more-complete MLD layer. Olafsen et al. showed a similar lower-temperature peak during temperature-programmed hydrogenation of carbon that formed during dry reforming on Ni catalysts.[29] They attributed this peark to a less stable (and less harmful) carbon type.[29]

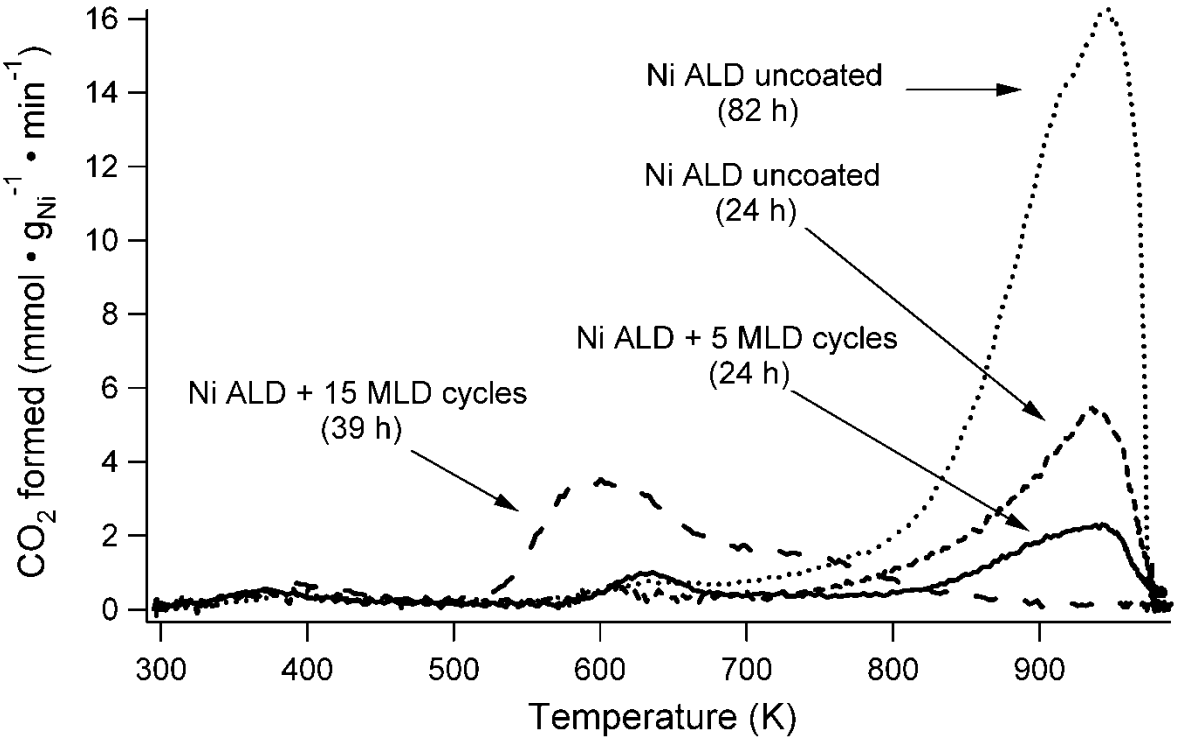

Figure 5.7. Rate of CO_2 formation during TPO after DRM at 973 K for 82 h and 24 h for the uncoated catalyst, 24 h for the 5-MLD catalyst, and 39 h for the 15-MLD catalyst.

5.5. Conclusions

Nickel/Al_2O_3 catalysts with particle sizes less than 5 nm were synthesized by ALD. These Ni particles easily sintered under DRM reaction conditions at 973 K, as demonstrated by a continual decrease in reaction rate with time, particle size increase observed by TEM, and a decrease in Ni surface area with increasing temperature. These Ni catalysts were stabilized by depositing a hybrid polymer-inorganic alucone MLD layer that was then calcined to form a porous alumina film over the catalyst particles. Calcining the MLD layer at 673 K resulted in rapid deactivation of the catalyst during DRM, whereas calcining at 773 K produced stable catalysts. The DRM rate on these catalysts increased over time before stabilizing as more Ni surface area became available. The MLD layers reduced sintering of the Ni particles relative to the uncoated catalyst. The small particle size and the greater available surface area of the 5-

MLD cycle catalyst caused that sample to have the highest steady-state DRM rate (even higher than the uncoated catalyst after 6 h). The 10-MLD cycle catalyst, even though it had a lower DRM rate, was stable even after repeated calcinations and reductions. Coating the catalysts with alumina MLD layers reduced coking during DRM compared to uncoated Ni.

Acknowledgments

We acknowledge financial support from NSF grant CBET 1067800.

5.6. References

[1] E.J. Moniz, H.D. Jacoby, A. Meggs, R. Armtrong, D. Cohn, S. Connors, J. Deutch, Q. Ejaz, J. Hezir, G. Kaufman, The future of natural gas, in, Cambridge, MA: MIT Press, 2011.
[2] Natural Gas Reforming, in: U.S.D.o. Energy (Ed.), U.S. Department of Energy, 2013.
[3] J.R. Rostrup-Nielsen, J. Sehested, J.K. Nørskov, Hydrogen and synthesis gas by steam- and C02 reforming, in: Advances in Catalysis, Academic Press, 2002, pp. 65-139.
[4] J. Rostrupnielsen, J.B. Hansen, Journal of Catalysis 144 (1993) 38-49.
[5] J.H. Edwards, A.M. Maitra, Fuel Processing Technology 42 (1995) 269-289.
[6] D.A. Wood, C. Nwaoha, B.F. Towler, Journal of Natural Gas Science and Engineering 9 (2012) 196-208.
[7] M. Gharibi, F.T. Zangeneh, F. Yaripour, S. Sahebdelfar, Applied Catalysis A: General 443-444 (2012) 8-26.
[8] J. Sehested, Catalysis Today 111 (2006) 103-110.
[9] J. Sehested, Journal of Catalysis 217 (2003) 417-426.
[10] H. Bengaard, J.K. Nørskov, J. Sehested, B.S. Clausen, L.P. Nielsen, A.M. Molenbroek, J.R. Rostrup-Nielsen, Journal of Catalysis 209 (2002) 365-384.
[11] S.R. de Miguel, I.M.J. Vilella, S.P. Maina, D.S. José-Alonso, M.C. Román-Martínez, M.J. Illán-Gómez, Applied Catalysis A: General (2012).
[12] M. García-Diéguez, E. Finocchio, M.Á. Larrubia, L.J. Alemany, G. Busca, Journal of Catalysis 274 (2010) 11-20.
[13] M. García-Diéguez, I.S. Pieta, M.C. Herrera, M.A. Larrubia, L.J. Alemany, Applied Catalysis A: General 377 (2010) 191-199.
[14] S. Helveg, J. Sehested, J.R. Rostrup-Nielsen, Catalysis Today 178 (2011) 42-46.
[15] G. Jones, J.G. Jakobsen, S.S. Shim, J. Kleis, M.P. Andersson, J. Rossmeisl, F. Abild-Pedersen, T. Bligaard, S. Helveg, B. Hinnemann, J.R. Rostrup-Nielsen, I. Chorkendorff, J. Sehested, J.K. Nørskov, Journal of Catalysis 259 (2008) 147-160.
[16] J. Lu, J.W. Elam, P.C. Stair, Accounts of Chemical Research (2013).
[17] H. Feng, J. Lu, P. Stair, J. Elam, Catalysis Letters 141 (2011) 512-517.
[18] J. Lu, B. Fu, M.C. Kung, G. Xiao, J.W. Elam, H.H. Kung, P.C. Stair, Science 335 (2012) 1205-1208.
[19] J. Lu, P.C. Stair, Angewandte Chemie International Edition 49 (2010) 2547-2551.

[20] X. Liang, J. Li, M. Yu, C.N. McMurray, J.L. Falconer, A.W. Weimer, ACS Catalysis 1 (2011) 1162-1165.
[21] N. Suzuki, Y. Yamauchi, Journal of sol-gel science and technology 53 (2010) 428-433.
[22] X. Liang, B. W Evanko, A. Izar, D. M King, Y.-B. Jiang, A.W. Weimer, Microporous and Mesoporous Materials (2012).
[23] A.A. Dameron, D. Seghete, B.B. Burton, S.D. Davidson, A.S. Cavanagh, J.A. Bertrand, S.M. George, Chemistry of Materials 20 (2008) 3315-3326.
[24] B. Yoon, D. Seghete, A.S. Cavanagh, S.M. George, Chemistry of Materials 21 (2009) 5365-5374.
[25] T.D. Gould, A.M. Lubers, B.T. Neltner, J.V. Carrier, A.W. Weimer, J.L. Falconer, J. Will Medlin, Journal of Catalysis 303 (2013) 9-15.
[26] D. Baudouin, U. Rodemerck, F. Krumeich, A.d. Mallmann, K.C. Szeto, H. Ménardd, L. Veyre, J.-P. Candy, P.B. Webb, C. Thieuleux, C. Copéreta, Journal of Catalysis 297 (2013) 27-34.
[27] D. Baudouin, K.C. Szeto, P. Laurent, A. De Mallmann, B. Fenet, L. Veyre, U. Rodemerck, C. Copéret, C. Thieuleux, Journal of the American Chemical Society 134 (2012) 20624-20627.
[28] T.D. Gould, M.M. Montemore, A.M. Lubers, A. Weimer, J.L. Falconer, J.W. Medlin, Submitted to Journal of Catalysis (2013).
[29] A. Olafsen, C. Daniel, Y. Schuurman, L. RÃ¥berg, U. Olsbye, C. Mirodatos, Catalysis Today 115 (2006) 179-185.

5.7 Supplemental Information

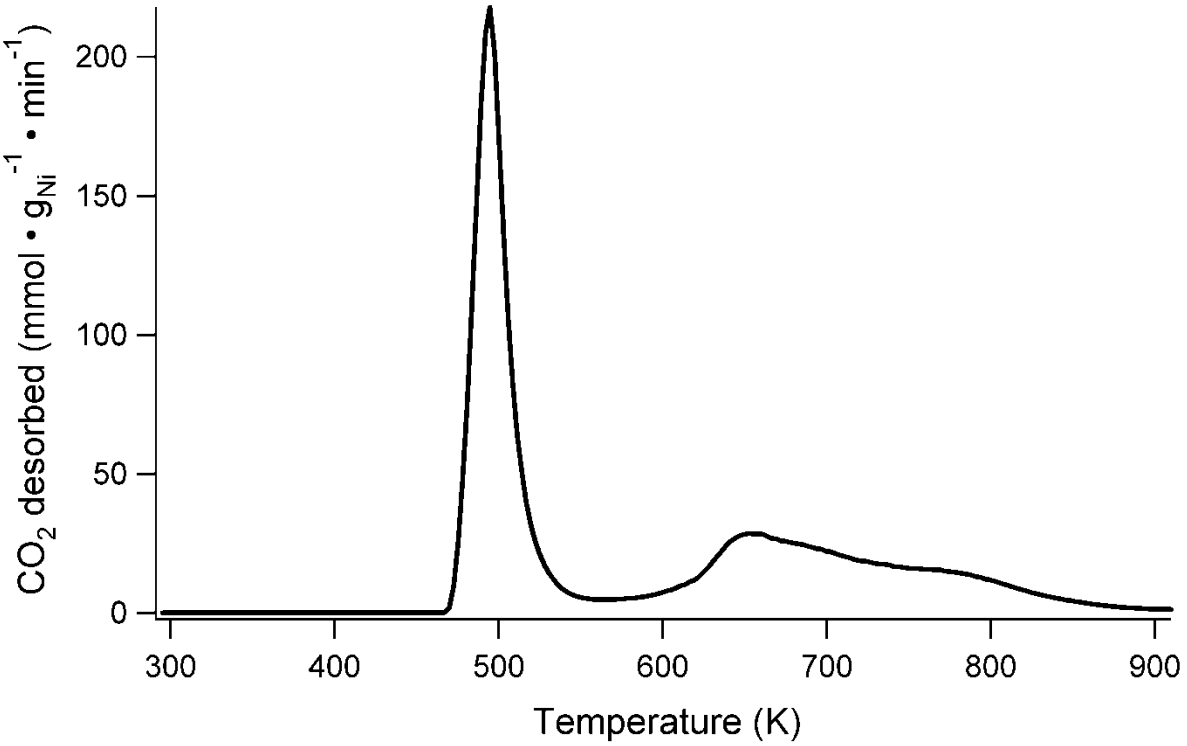

Figure 5.S1. Carbon dioxide formed during TPO used to remove the organic component of the hybrid polymer-inorganic MLD layer from a 10-MLD cycle modified Ni/Al_2O_3 ALD catalyst.

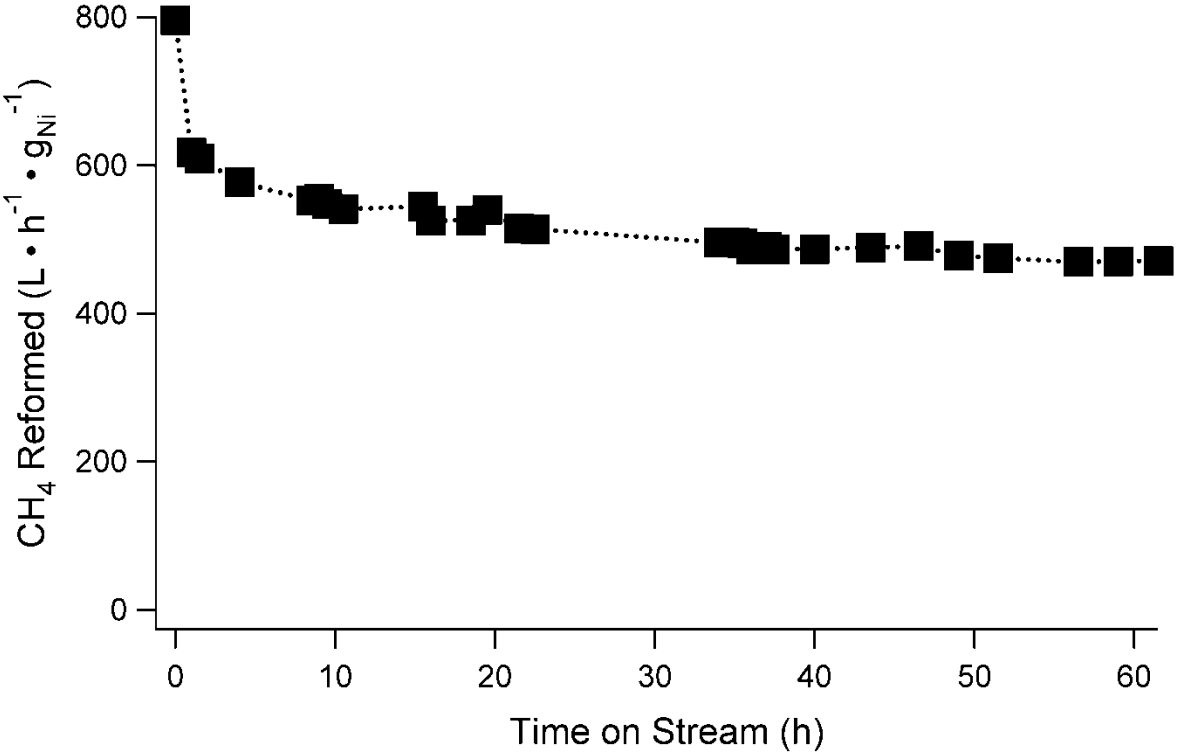

Figure 5.S2. Dry reforming rate of Ni catalyst with 10-MLD layers after oxidizing the catalyst at 773 K and then reducing it at 973 K.

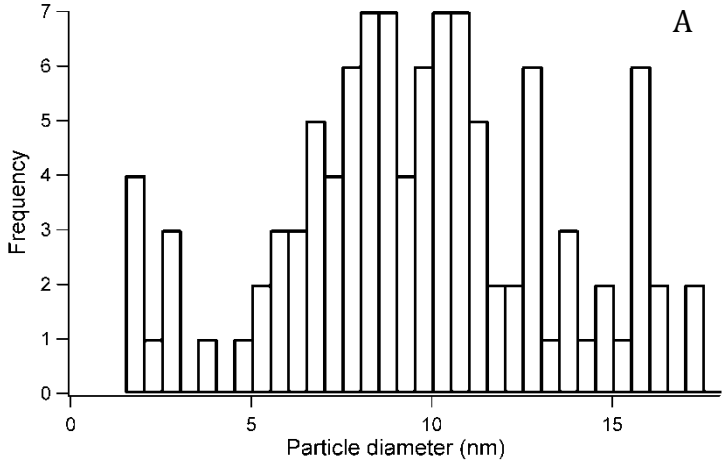

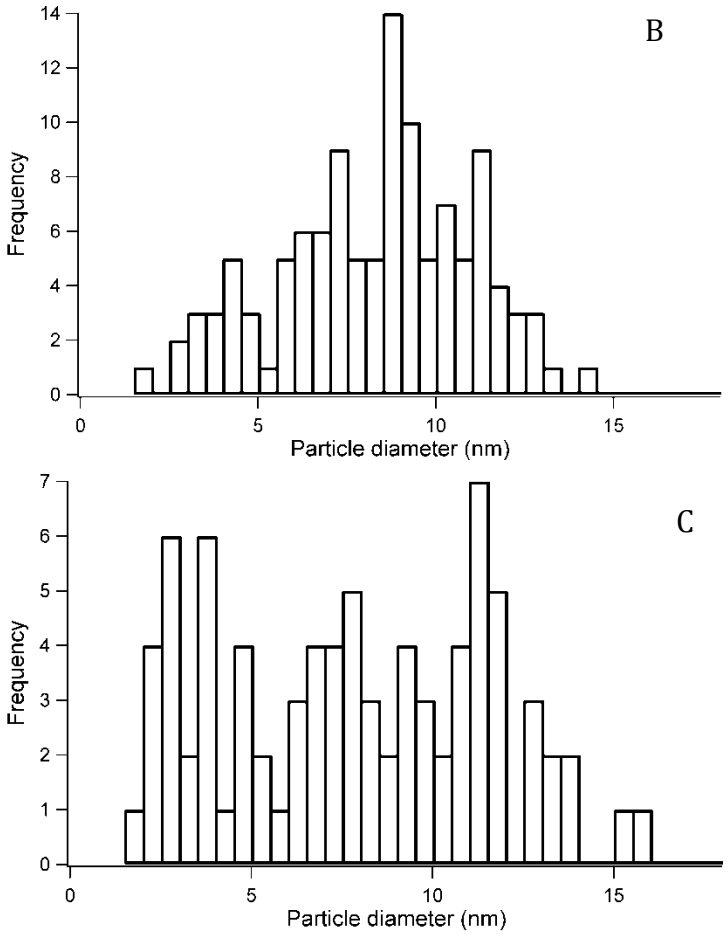

Figure 5.S3. Nickel particle size distributions of A) Ni ALD uncoated catalyst after 82-h DRM, B) Ni ALD catalyst with 5-MLD layers after 2 regenerations and 138-h total DRM time, C) Ni ALD catalyst with 10-MLD layers after 2 regenerations and 108-h DRM.

5.8 Chapter 5 Appendix: Molecular Layer Deposition on NiPt ALD Catalysts

5.8.1 Introduction and Experimental Methods

Chapter 5 demonstrated that MLD could be used to stabilize Ni catalyst particles during DRM. The same ABC MLD chemistry was also used on NiPt bimetallic catalysts, and the results are presented here. All the experiments found in Chapter 5 were performed the same way, with the exception of a few key details:

- The ALD catalysts were synthesized the same way, except that the Ni precursor flowed through a line that had trace amounts of the Pt ALD precursor, $Me_3MeCpPt$.
- The calcination temperature was 673 K, as opposed to 773 K that was used on the Ni catalysts.
- Only 10 and 15 MLD cycles were deposited. Unpublished work by Xinhua Liang indicated that MLD layers most likely did not form complete layers until around 10 MLD layers, and so a 5-cycle sample was not prepared (this NiPt work was completed before the Ni-MLD work, which did include a 5-cycle sample).

This appendix provides a summary of the results for catalyst characterization and evaluation for DRM activity and stability. The results are briefly presented and compared to the Ni-MLD catalysts previously discussed in chapter 5.

5.8.2 Characterization of Ni ALD catalysts and MLD stabilizing layers

Nickel-platinum catalysts were synthesized by ALD on an alumina support for testing the effectiveness of MLD layers at preventing sintering. One ALD cycle was used to create small metal particles. The weight loadings of the catalysts were kept low (0.9 Ni wt% and 0.1 Pt wt%) to limit sintering. The average particle size of the catalysts was difficult to accurately measure

by TEM due to their small size, which was estimated to be 4.8 nm by H_2 chemisorption. Images of these catalysts are shown in Figure 5.A1.

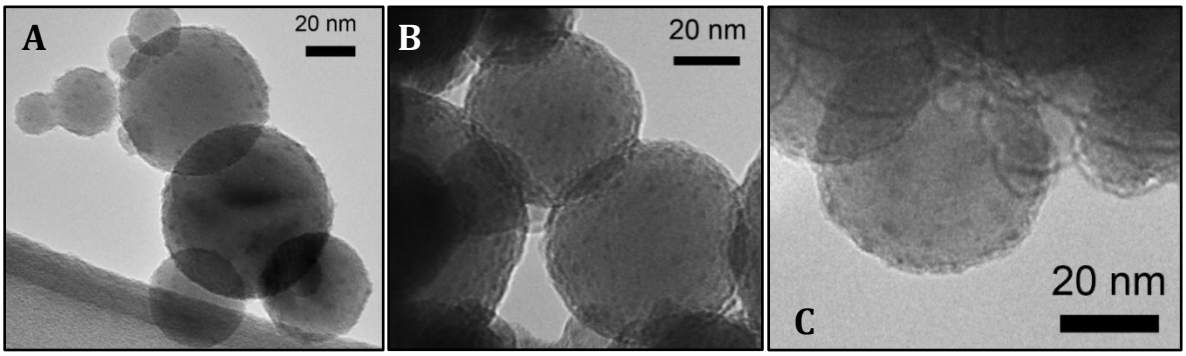

Figure 5.A1. NiPt nanoparticles (~1-2 nm dark particles) deposited on spherical alumina, B) NiPt nanoparticles coated by 10-MLD cycles, C) NiPt nanoparticles coated by 15-MLD cycles.

The ALD catalysts were coated with 10 and 15 ABC MLD cycles. As shown in Figure 5.A1, these coatings did not significantly change the Ni particle size, and ICP-MS indicated that the MLD layers did not significantly alter the metal weight loadings. The coating measured by TEM for 15-MLD cycles was thicker (2.9 +/- 0.5 nm) than the 10-cycle layer (2.1 +/- 0.2 nm), as expected. After calcination, the MLD coating was not detected by TEM for the 10-MLD cycles catalyst, but the collapsed porous layer was still visible for the 15-cycle MLD layer, as shown in Figure 5.A2.

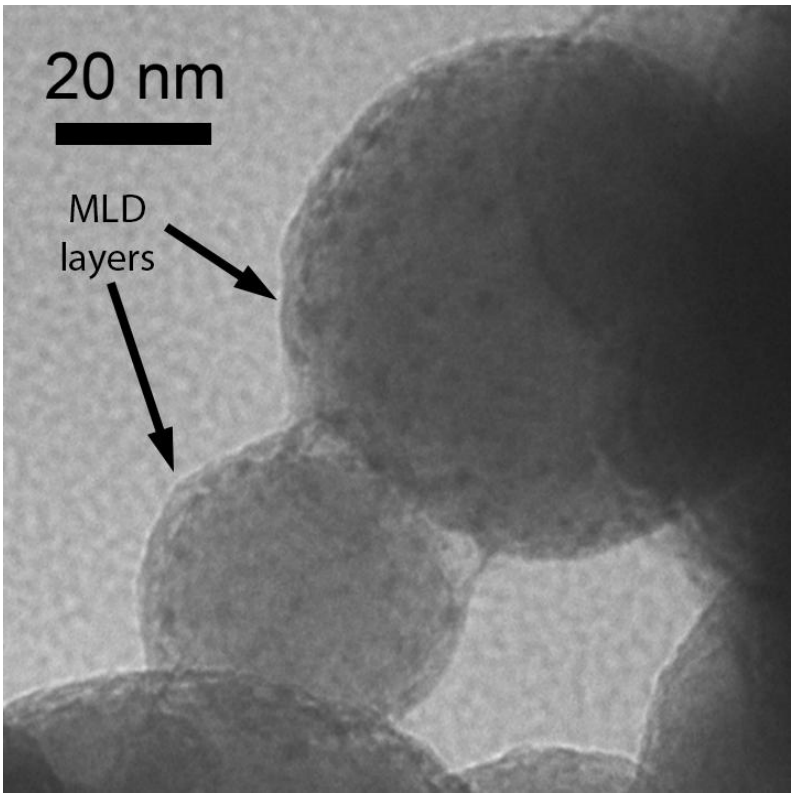

Figure 5.A2. TEM of NiPt ALD catalysts (< 2-nm dark particles) coated with 15 MLD cycles after calcination in air at 673 K for 1 h, then reduced at 773 K for 1 h.

The calcination temperature was 673 K for all NiPt-MLD catalysts, and the TPO shows a distinct difference in the removal of organic components between the Ni and NiPt catalysts (Figure 5.A3). Chemisorption measurements in Table 1 indicate that the 10-cycle MLD layers covered about 35% of the metal active sites, and 15-cycle layers covered 90% of the metal surface area. The non-linear change in active surface area with the number of MLD cycles is likely due to an initial nucleation period where the MLD deposition was not conformal. Although a temperature-ramp chemisorption study was not performed (like with the Ni ALD + MLD catalysts), there were major differences in the surface area of the catalysts. The NiPt-MLD catalyst had more surface area exposed than the Ni catalyst at 10 MLD cycles, and the available fraction (65%) of the uncoated NiPt catalyst's surface area was also higher than the Ni catalyst (~33%). The 15 MLD layers decreased the available surface area on the NiPt catalyst more than

the Ni catalyst though (10% available for NiPt and ~33% for Ni MLD). This trend could be an indication that 10 MLD cycles had not yet formed a complete layer on the NiPt catalysts (by not nucleating as well as on the Ni catalyst), but once a conformal layer was formed more active sites were blocked on the NiPt catalyst than the Ni catalyst. These data support the conjecture that the MLD coating did not coat the NiPt catalyst as easily as the Ni catalyst (which was likely NiO), and that the MLD layers did not form as uniformly as on the Ni catalyst.

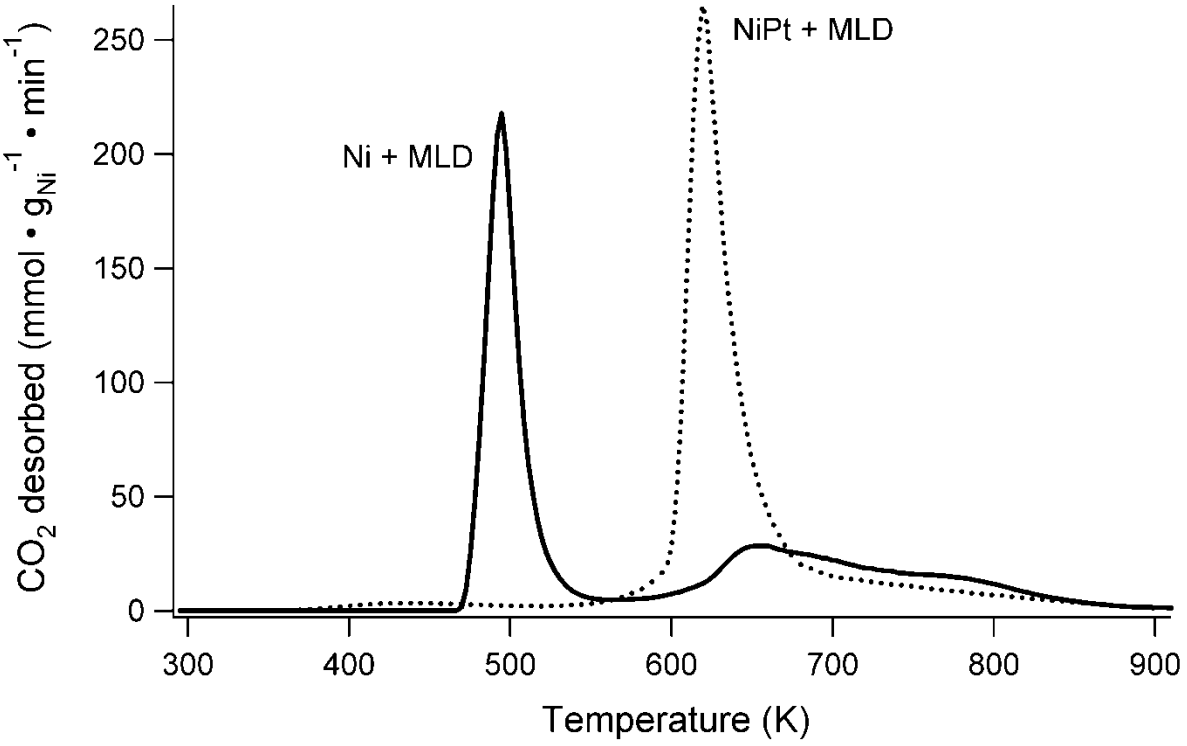

Figure 5.A3. Carbon dioxide form during TPO used to remove the organic components of the NiPt catalyst and the Ni catalyst, each with 10 ABC MLD polymer hybrid layers.

Table 5.A3. Catalyst properties and DRM activity

MLD cycles	H_2 adsorbed ($\mu mol \cdot g_{catalyst}^{-1}$)	Time on stream (h)	Initial DRM activity[a] ($L\ CH_4 \cdot h^{-1} \cdot g_{metal}^{-1}$)	Final DRM activity ($L\ CH_4 \cdot h^{-1} \cdot g_{metal}^{-1}$)	Particle size after reaction (nm)
0	20	220	720	460	6.0 +/- 4.2
10	13	12	710	520	4.8 +/- 1.4
15	2.0	172	540	390	3.4 +/- 1.0

[a] The maximum rate within the first few hours, ignoring the initial data point.

5.8.3 Dry reforming activity and stability

The catalysts were evaluated for dry reforming activity and stability to gauge the effectiveness of the MLD layers at preventing sintering. All of the DRM rates decreased over time (Figure 5.A4), but the percent activity lost decreased when the catalysts were coated by 15 MLD cycles. The initial DRM rate per gram of metal for the 10-cycle MLD catalyst was similar to the uncoated catalyst, and the initial rate for 15-cycle MLD sample was ~25% lower than the uncoated catalyst. The ratio of initial rates for the MLD catalysts to the uncoated catalyst was much larger than the ratio of their active surface areas measured by chemisorption. These discrepancies were likely due to partial uncovering of metal sites at reaction conditions, since the catalysts were reacted at 973 K but only heated to 773 K before chemisorption. The thermal stresses from the high temperature likely caused the small pores in the alumina layer open up more to expose additional sites on the catalysts. Suzuki and Yamauchi also observed similar behavior in their porous alumina structures synthesized by a single-step sol-gel technique.[1]

The median pore diameter of their hierarchal porous alumina network increased from 3.9 nm (calcined at 773 K) to 6.0 nm for calcination at 973 K.

To test this hypothesis of uncovering active surface area, a previously-calcined (1 h 773 K) 15-cycle MLD sample was reduced at 773 K for 1 h, and then held at 773 K for 1 h before running chemisorption. The amount of H_2 chemisorbed was 2.4 $\mu mol \bullet g_{catalyst}^{-1}$. The same catalyst was then reduced again at 773 K, then held at 973 K under a flow of He for 3 more h before running the chemisorption measurement, which yielded the same value (2.4 $\mu mol \bullet g_{catalyst}^{-1}$). Not only were the chemisorption values slightly higher than the original value (1.5 $\mu mol \bullet g_{catalyst}^{-1}$), but these values were obtained after high temperature thermal treatment, which should have sintered the particles partially. This experiment yielded different results from when it was conducted on the Ni-MLD catalysts. Those catalysts had no increase in surface area from high temperature treatment under He. This also supports the conjecture that the MLD layer formed a better bond with NiO on the Ni catalysts than with the NiPt surfaces.

The uncoated catalyst and the 15-MLD cycle catalyst were evaluated for long-term DRM activity because the catalysts activity was still decreasing slightly after 24 h. The DRM activity of the 15-cycle sample was relatively stable at 172 h with most of the loss occurring in the first 24 h, as shown in Figure 5.A4B. The decrease in reaction rate was linear after 48 h, so the change in DRM rate was calculated to be -0.50 L/h for the uncoated NiPt catalyst and -0.12 L/h for the NiPt catalyst coated with 15 MLD layers. The DRM rates were also normalized to the final measured reaction rate to gauge which catalyst deactivated faster, as shown in Figure 5.A4c. When normalized by the final rate, the uncoated catalyst activity clearly decreased faster

and lost much more of its activity compared to the 15-MLD coated catalyst.

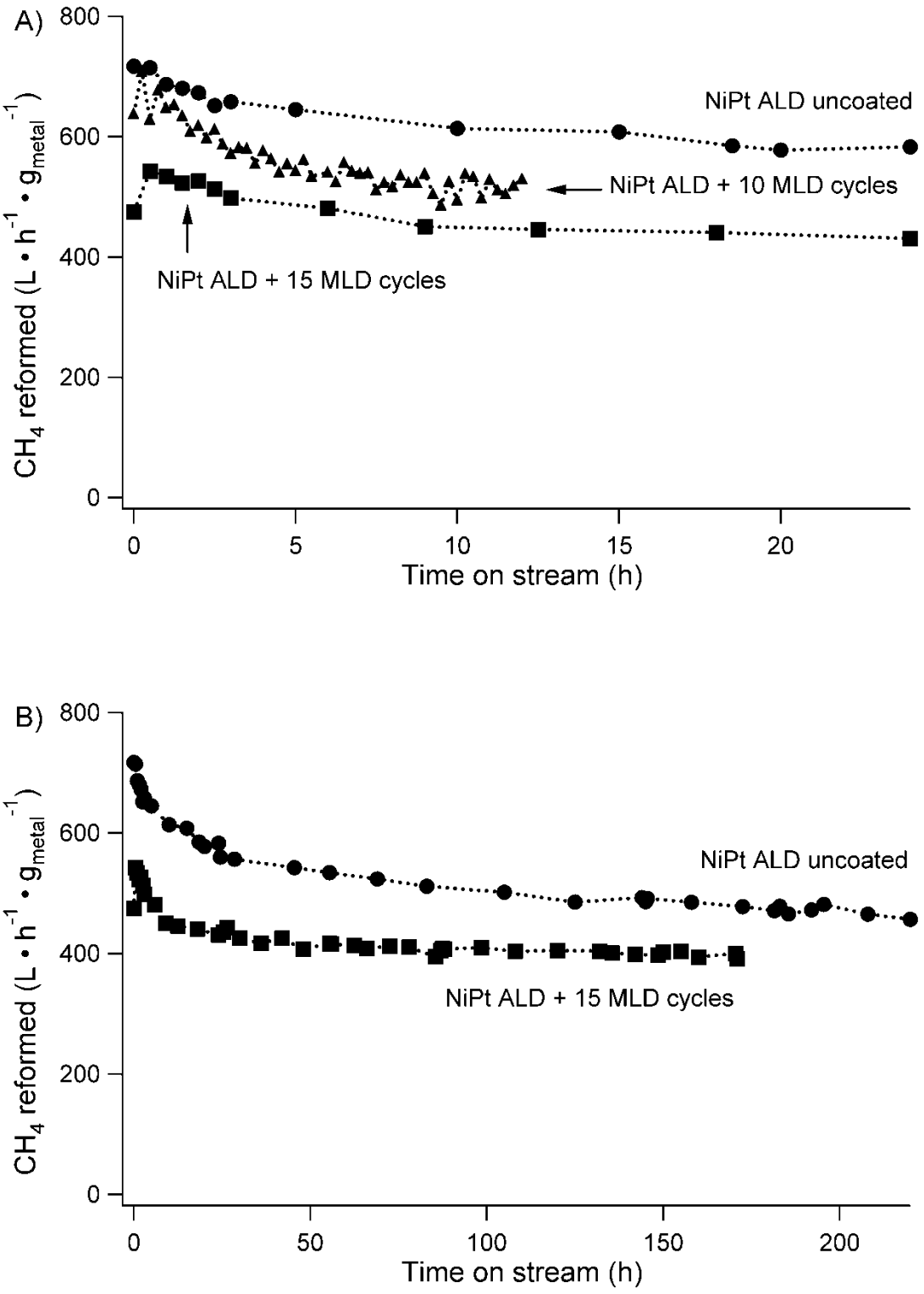

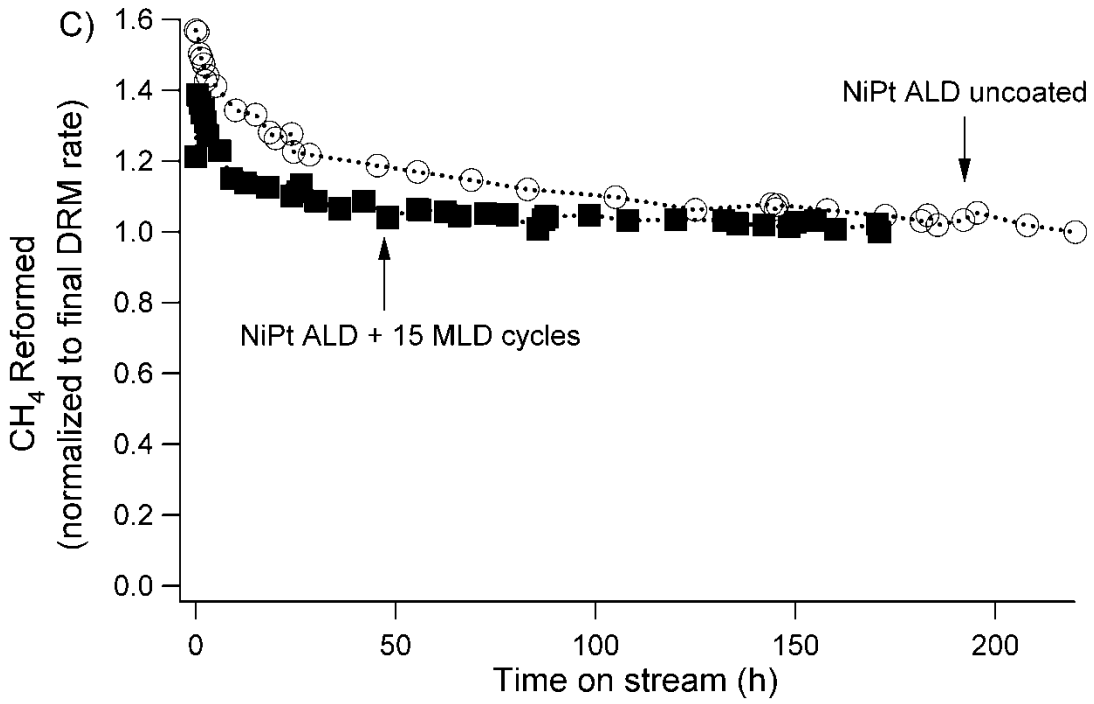

Figure 5.A4. Dry reforming rates at 973 K: A) first 24 h for uncoated NiPt ALD catalyst, and the same catalysts coated with 10 and 15 MLD layers. B) Long term DRM rates for uncoated and 15-MLD catalyst. C) DRM Rates normalized to final observed DRM rate for uncoated NiPt and 15-MLD NiPt catalysts.

The metal particles sintered during DRM, as measured by TEM (Figure 5.A5), but the uncoated catalyst sintered the most; it had a post-reaction particle size of 6.3 +/- 2.4 nm after 24 h and 6.0 +/- 4.4 nm after 220 h. Coating the catalysts with 10-MLD cycles reduced sintering (particle size after 12 hours of reaction was 4.8 +/- 1.4 nm), and the 15-cycle catalyst sintered the least (particle size after 172 h of reaction was 3.4 +/- 1.0 nm). The standard deviation of particle size was also smaller for the 15-cycle catalyst. The wider range of particle sizes in the uncoated sample is likely due to Ostwald ripening, where smaller particles desorb atoms, which then adsorb on larger particles to minimize particle surface energy.

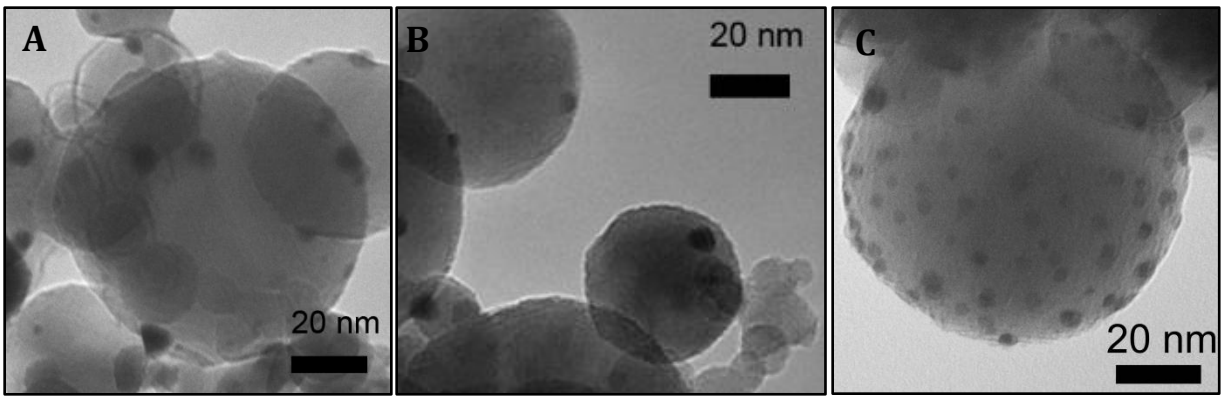

Figure 5.A5. TEM images of post-reaction NiPt catalysts on spherical alumina supports: (A) uncoated sample, after 24 h reaction, (B) coated with 10 MLD layers, after 12 h reaction, (C) coated with 15 MLD cycles, after 172 h reaction

Although sintering prevention was the main focus of this study, another benefit of maintaining small particle size is inhibiting coking. The MLD-treated sample accumulated less carbon in 172 h than uncoated catalyst (after 220 h), as shown in Figure 5.A6. The extra reaction time on the uncoated catalyst likely did not significantly increase the sintering of the particles or the amount of coke. The broadness of the peak for the NiPt catalyst indicates that carbon deposited on that sample had varying degrees of stability. The amount of the carbon removed during the TPO on the NiPt catalysts was 10-20% of that removed from the post-reaction Ni ALD and Ni-MLD catalysts. The lower carbon deposition is not surprising, since the NiPt particles did not sinter as much (which would prevent carbon deposition on its own) and NiPt catalysts are less prone to coking in general.

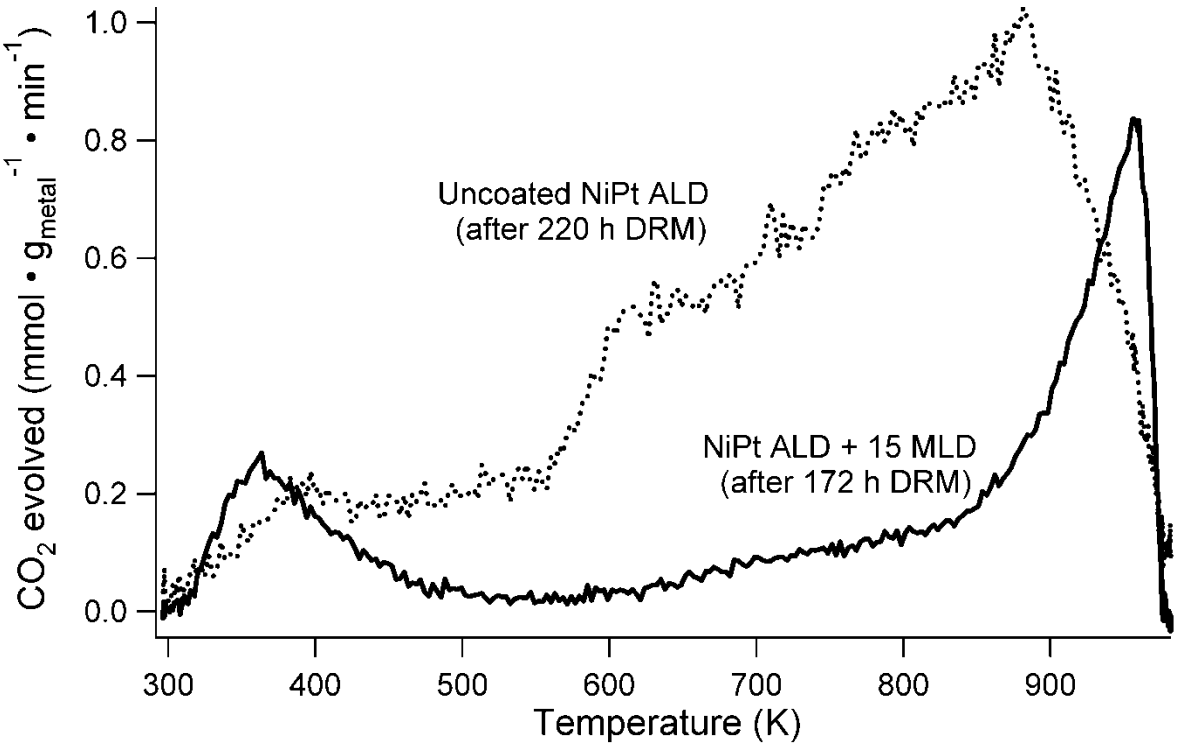

Figure 5.A6. Rate of CO_2 formation during temperature-programmed oxidation, after dry reforming of methane for the times indicated, of an alumina-supported NiPt ALD catalyst and the NiPt ALD catalyst with 15 MLD cycles

5.8.4. Conclusions

Bimetallic NiPt catalysts were synthesized by ALD with small particle sizes, which make them prone to sintering. These catalysts were modified with a porous alumina stabilization layer by MLD, but the DRM rate still decreased over time. Most of the surface area (~90%) was covered by 15-MLD layers, which may have helped limit sintering. The catalyst with 15-MLD cycles was stable up to 172 h during DRM at 973 K, and only sintered to 3.4 nm after 172 h, whereas the uncoated catalyst sintered to 6.4 nm after 24 h. Additionally, the MLD coating reduced the amount of coking on the catalysts because the small particle sizes were maintained or the catalysts sites were covered by the MLD layer. The MLD coatings were an effective method of limiting sintering of the NiPt nanoparticles under DRM conditions, but at the expense

of covering surface area. Using MLD to modify NiPt catalysts was not as effective at maintaining a high (and stable) DRM rate like the Ni-MLD catalysts mentioned earlier.

References

[1] N. Suzuki, Y. Yamauchi, Journal of sol-gel science and technology 53 (2010) 428-433.

[2] S. Helveg, J. Sehested, J.R. Rostrup-Nielsen, Catalysis Today 178 (2011) 42-46.

[3] T.D. Gould, A.M. Lubers, B.T. Neltner, J.V. Carrier, A.W. Weimer, J.L. Falconer, J. Will Medlin, Journal of Catalysis 303 (2013) 9-15.

Chapter 6: Conclusions and Recommendations

6.1 Conclusions

This work demonstrated synthesis of Ni, Pt, and NiPt supported catalysts by ALD in the size range where catalytic behavior becomes particularly interesting and much different than what is observed on larger metal catalyst particles. The four main objectives of this thesis are concluded in detail at the end of their perspective chapters. Here we review the general findings of these studies.

Nickel ALD shows that nanoparticle ALD is possible for more than noble metals. Work over the past 10 years on ALD synthesis of catalysts particles has been dominated almost entirely by Pt and Pd ALD. While these systems are of great interest due to the catalytic properties of these < 2 nm particles, the practicality of using this technology is greatly diminished since Pt and Pd are often cost-prohibitive; especially once the costs of performing ALD are included. This thesis demonstrated the synthesis of the first non-noble metal nanoparticle catalysts by ALD. Depositing Ni particles by ALD allows for variation in particle size and weight loading at a size-scale that is often difficult to achieve with other Ni deposition techniques. These Ni ALD nanoparticles are among the smallest sizes reported, and so they have broad-reaching applications in many reactions that demand small particle size. The lower cost of Ni and the enhanced nanoscale properties of these ALD catalysts suggest that they could be used in place of more expensive metals, or be combined with them (*i.e.*, Ni-bimetallics) to reduce cost, and in some cases improve catalytic performance.

Structure-sensitive reactions benefit from ALD. With the exception of hydrogenolysis of propylene on Ni ALD catalysts, the other example reactions in this thesis benefit from small particle sizes. This benefit depends entirely on the type of reaction though, and what kind of

structure-sensitivity that reaction imparts. Smaller particles in DRM reactions inhibit coking more and have greater activity per gram of metal. In the case of bimetallic catalysts, the amount of bimetallic interaction is maximized when more of each metal is in close contact with each other, which is inherently true when the particle size is small. The Pt ALD catalysts used for ODHP reactions maximized selectivity for propylene when the catalysts were the smallest (and therefore had the least coordinated atoms on the surface). Additionallly, for the case of any metal catalyst, maximizing active metal surface area per g-metal reduces the required mass of catalyst and therefore ultimately reduces the cost of using the catalyst.

Pristine nanoscale catalysts change under reaction conditions. This thesis demonstrated the synthesis of extremely small nanoparticles, with diameters even reaching sub-nm for the Pt catalysts. Once small nanoparticles are introduced to reaction conditions, they often sinter, sometimes considerably. In the case of the DRM reactions, whose conditions are particularly harsh for catalyst sintering, the Ni and NiPt nanoparticles sintered, but not to sizes that cause problems with coking. Starting with a catalyst with larger metal particles (even a pre-sintered version of the Ni ALD catalyst) introduced complications with carbon whisker formation. Chapter 5 showed that MLD layers can be used to mitigate sintering and stabilize catalytic performance, which has broad-reaching implications for a variety of applications if other catalysts (synthesized by ALD or other techniques) can be stabilized to such a degree.

6.2 Future Directions and Recommendations

Atomic layer deposition is still a relatively new technology for applications in catalyst synthesis, and therefore still has much unexplored potential in the field of catalysis. This chapter presents discussion and preliminary data for findings that were not studied in detail but showed interesting preliminary results. Recommendations for future work are also presented to take advantage of the versatility and nanoscale properties of ALD catalytic materials.

6.2.1 Investigating MLD-coated DRM catalysts

Chapter 5 had several interesting results associated with the properties of the MLD layer on Ni that should be explored further. Understanding why the MLD layer was so beneficial could have far-reaching implications for other catalyst stabilization, or could lead to an even better performance for Ni ALD-MLD catalysts than what was reported in this thesis. Aspects that should be studied further include:

1) Determining the effect of pretreatment on the MLD layer structure.
2) Understanding why MLD coatings were different for Ni and Pt
3) Optimizing the number of MLD cycles for the Ni + MLD catalysts

Although the type of pretreatment is known to affect the properties of the porous MLD alumina layer,[1] the work in chapter 5 showed a dramatic effect of calcination temperature on DRM behavior. This thesis showed no difference in "extreme" calcination (by TPO to 973 K) and calcination at 773 K, but these results are still different from calcinations reported in literature for ABC MLD alucone layers on alumina,[1] and AB MLD alucone layers on Pt/SiO_2.[2] In-depth studies on the pore structure of the Ni ALD/MLD catalysts should be carried out to compare with previous studies on the MLD layers reported in literature. However, because the work in chapter 5 used a low number of MLD cycles, low Ni weight loading, and a

low surface area support, gas-phase characterization (such as micropore analysis, or differences in surface area) were not possible. Future studies aimed at specifically measuring properties of the MLD layers on Ni catalysts should synthesize catalysts with more Ni surface area (similar to the 15 cycle Ni ALD sample from Chapter 2) and a higher surface area support (to accommodate more catalyst). Additionally, the deactivation observed in Chapter 5 after calcining at 673 K could be further characterized to determine if the mechanism of deactivation was associated with coking, and whether subsequent calcination at 773 K would improve the catalyst. Temperature-programmed oxidation could be used after the catalyst was oxidized at 673 K (before reaction), and then again after reaction to probe whether this calcination temperature led to more carbon formation than normal.

More in-depth studies are needed to determine the differences between MLD on Ni, NiPt, or Pt. Temperature-programmed oxidation showed that removal of organic components from the MLD polymer hybrid layer was dramatically different for the Ni and NiPt catalysts. In addition, many catalytic properties of the MLD-NiPt system deviated from those of the Ni-MLD system. Nickel may be exhibiting unique properties since it readily forms an oxide, which may be more ideal for MLD coatings. While Pt can also have an oxide layer, this oxide can be easily reduced by dosing TMA. This work suggests that the first few cycles of MLD are crucial, and are most likely different on the two metals. Feng *et al.* showed that TMA preferentially binds to defect sites on Pt, but this may not happen on pure Ni, or especially NiO.[3] The Ni catalyst in Chapter 5 had MLD layers deposited on catalysts that were exposed to the atmosphere (and thus oxidized). Performing MLD immediately following ALD (in the same reactor), or by first reducing the Ni catalyst would likely yield a different result and could highlight the effect of having a metal oxide as the active site for MLD rather than metal.

One method for probing differences in the MLD layer on each of these metals is *in situ* FTIR of the MLD layers. The development of the ABC MLD chemistry by the George group was aided by *in situ* FTIR of the organic components of the MLD layer as it was being grown.[4] If the organic components are assembling differently in each catalyst system, then monitoring the MLD hybrid organic-inorganic layer during the first few cycles of growth should elucidate differences, and could be compared to FTIR data from previous studies by the George group when the ABC MLD chemistry was grown on metal oxides like alumina.[4] Performing FTIR *in situ* can often prove difficult, so even doing DRIFTS on Ni and Pt catalysts coated with MLD could indicate major differences in the organic layer.

Finally, more work should be done to optimize the number of MLD cycles. The work in this thesis only used 5, 10 and 15 cycles to coat the catalysts. Adding more than 15 cycles likely would show no benefit and only decrease catalytic activity by increasing mass-transfer issues. However, doing fewer than 5 could show even higher DRM activity, but potentially less stability. An intermediate number of cycles between 5 and 10 could reach an ideal case that combines the stability observed on the 10-MLD sample with the high activity of the 5-MLD sample. For the lower number of cycles (less than 5), the MLD layer is likely not covering the catalyst entirely, but determining this amount covered would be beneficial. Techniques like chemisorption cannot distinguish between a completely open metal site and one covered by a porous layer. Other surface-sensitive techniques such as XPS should be employed to determine how much of the surface is covered by these MLD layers at varying number of cycles.

6.2.2 Investigating other metal ALD chemistries for nanoparticle deposition with H_2.

The Weimer group had previously demonstrated the synthesis of Fe nanoparticles by ALD, but these were achieved by first depositing Fe_2O_3 ALD (using ferrocene and O_2), then

reducing the catalysts at excessively high temperatures (close to 1173 K) to form the nanoparticles. Instead, avoiding formation of the oxide by depositing metallic Fe would be desirable. The Fe ALD precursor, ferrocene, is almost identical to the Ni ALD precursor nickelocene (which also forms an oxide film when deposited with O_2). We hypothesize that by using H_2 gas as the second half-reaction reagent, metallic Fe nanoparticles should be deposited by ALD, much like the case with Ni ALD.

A test-run of this chemistry was performed in a fluidized bed reactor (specifically the cobalt-ferrite reactor in the Weimer lab). The ALD deposition temperature for Fe (673 K) was higher than the Ni ALD deposition temperature (573 K) since the Fe precursor is slightly more stable than the Ni precursor. Only one cycle was performed to deposit small nanoparticles. The sample was a grey color when pulled out of the FBR, but analysis by TEM remains inconclusive due to minimal contrast from these small Fe (or most likely Fe_2O_3) nanoparticles with the alumina substrate (Figure 6.). The Fe weight loading, determined by ICP-MS, was 0.6 wt% Fe. A sample with more cycles (2-5) should be prepared to confirm that ALD can actually deposit Fe crystallites. After 5 cycles, the catalyst particles should be sufficiently large to have a decent contrast with the substrate, and may also have visible lattice fringes that can be analyzed for the correct d-spacing corresponding to Fe or Fe_2O_3.

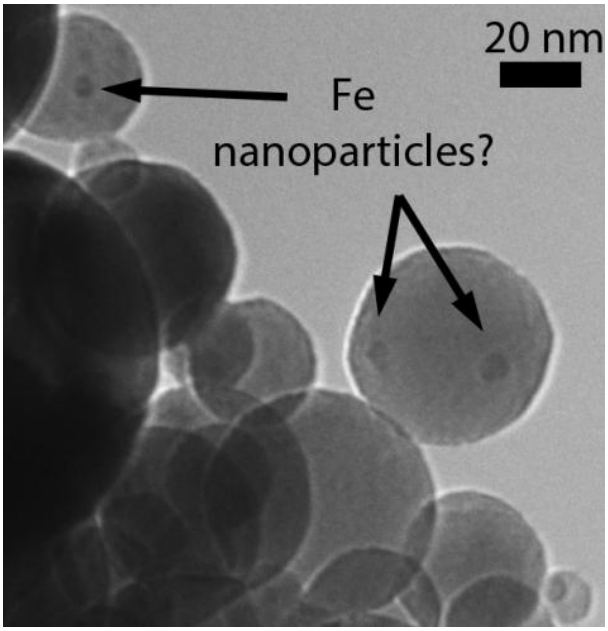

Figure 6.1. Possible Fe nanoparticles deposited by ALD with ferrocene and H_2 at 673 K.

With the success of Ni ALD, and with the likelihood that Fe nanoparticles were also deposited, Co metal nanoparticles might also be deposited by ALD with cobaltocene and H_2. Using H_2 could have far-reaching implications for other metals that have been demonstrated by metal oxide ALD, if these metal oxides could instead be deposited as metals. For example, future work using TiO_2 ALD to coat Ag nanoparticles could potentially benefit from using H_2 instead of the typical second half-reaction precursors O_2, H_2O, or ozone. Reduction of TiO_2 is inherently difficult since Ti is even more oxophillic than Ni or Fe, so eliminating a high temperature reduction step could be crucial in actually forming a bimetallic catalyst with a surface Ti layer.

Bimetallic catalysts created by ALD in this work had superior catalytic performance, but much work is needed to study bimetallic nanoparticle synthesis by ALD. Studies have shown that changing the order when metals are deposited sequentially or doing simultaneous deposition often creates catalysts with different material and catalytic properties.[5, 6] The work in this thesis used one cycle of Ni ALD, followed by one cycle of Pt ALD. If the metals were deposited

in reverse order, the ratio of metals would likely be different, and the size of the particles would likely be different as well. Simultaneous metal deposition should also be employed with ALD, by co-feeding two different precursors to study the effect of catalytic and material properties when they are deposited at the same time instead of sequentially. Co-dosing ALD precursors may be limited to dosing similar molecules, such as nickelocene and ferrocene, to reduce the potential for gas phase reaction between the precursor (which would result in CVD not ALD). Ferrocene and cobaltocene could also be ideal precursors for co-feeding to make bimetallic CoFe catalysts for the Fischer-Tropsch reaction.

6.2.3 Nickel oxide ALD as base-layer for Pt ALD.

The effect of H_2 or O_2 on Pt ALD particle size was originally observed on an alumina nanosphere that was coated with approximately 30 NiO ALD cycles. This substrate was used to take advantage of the surface energy difference between Pt and NiO in order to force the nanoparticles to spread out on the surface more, potentially creating a Pt film with a low number of ALD cycles. Twenty cycles of Pt ALD was performed on these NiO layers in order to exacerbate differences in particle size with the second half-reaction chemistry. As shown in Figure 6., the Pt particles synthesized with O_2 were relatively large (for ALD catalysts) at sizes greater than 5 nm.

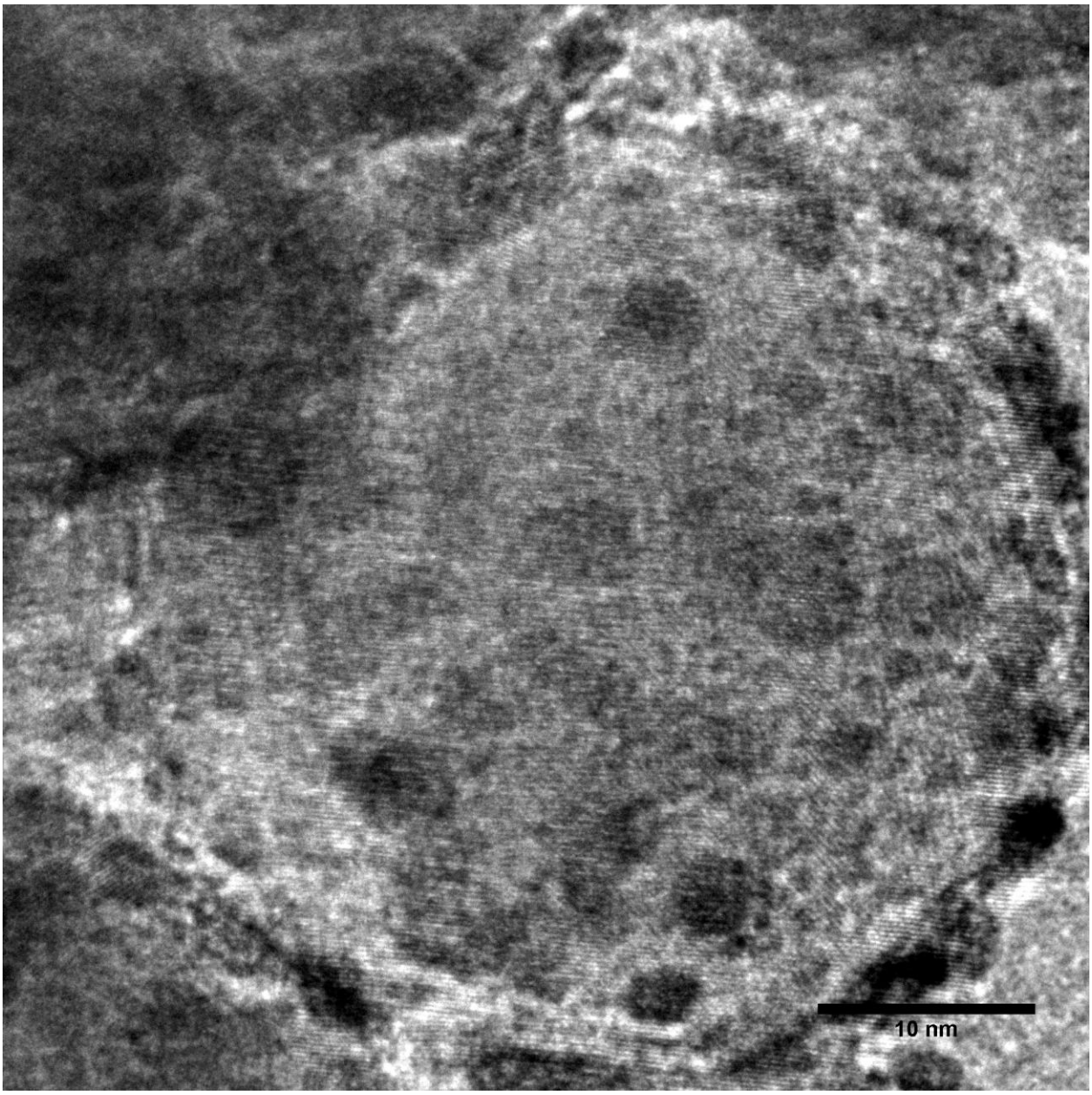

Figure 6.2. HRTEM of 20 cycles Pt ALD (done with O_2) on NiO ALD layer on top of alumina nanosphere support.

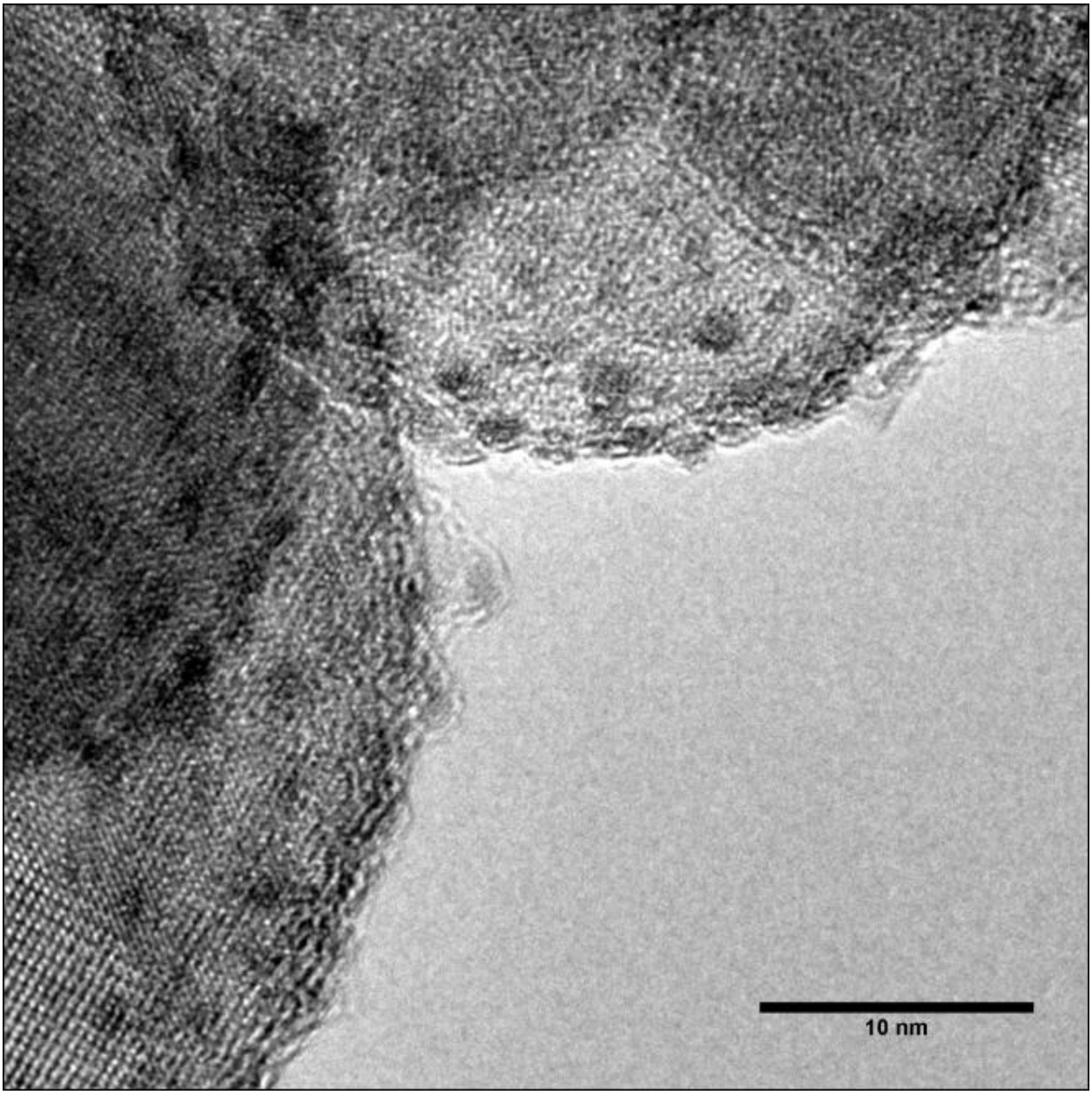

Figure 6.3. HRTEM of 20 cycles Pt ALD (with H_2) on NiO ALD layer on top of Al_2O_3.

Interestingly, the Pt ALD done with H_2 produced extremely small nanoparticles (Figure 6.), some in the sub-nm range even after 20 cycles. Why this happened is unclear, but could be due to 1) substrate effects from the NiO causing the Pt nanoparticles to form smaller particles than normally done on alumina or 2) limiting the amount of nucleation that occurs on the NiO,

therefore shutting down further depositions after all the active sites were depleted (*i.e.*, the 20 cycles of Pt ALD may have only deposited Pt during the first 10 or so cycles). Even if the second hypothesis is true, these particles were still about the same size as those created by 5 cycles of Pt ALD with H_2 on alumina, and those particles were deposited at a much lower temperature. Further investigation into the cause for this phenomenon would need to analyze if this effect occurred on the NiO for a fewer number of cycles (1 and 5 at least), which could lead to even smaller sub-nm particles.

These catalysts should also be evaluated for ODHP activity, especially in the case that one Pt ALD cycle is performed on a NiO ALD layer. Not only could these catalysts be more active than the catalysts in Chapter 2 because of a smaller catalyst size, but NiO has also shown promising yields for ODHP.[7] The NiO/Al_2O_3 catalysts in literature take advantage of forming a Ni-aluminate with a NiO over-layer, which is more favorable for ODHP, especially when doped with certain additives (such as V, Mo, Co, Nb, and Ta).[7]

6.2.4 ALD catalysts for hydrodeoxygenation of furfural

In the second chapter of this thesis, Ni ALD particles were synthesized and tested with a probe reaction of propylene hydrogenolysis. The eventual goal of this catalyst was to do hydrogenolysis on larger molecules commonly found in biorefineries, such fatty acids or compounds such as furfural, but these molecules were not investigated in this thesis. Hydrodeoxygenation (HDO) of furfural to form the higher-value products furfuryl alcohol and methylfuran have used Ni catalysts, but they impart high selectivity towards the unfavorable decarbonylation pathway to form furan. Other metals such as Cu can help direct this reaction pathway towards furfuryl alcohol.[8] Previous efforts in the Medlin research group have utilized organic-thiol self-assembled monolayers to selectively shut down the unfavorable

decarbonylation reaction, thereby increasing selectivity to furfuryl alcohol and methylfuran.[9] While they showed enhancements to selectivity, the reaction rate was rather low. Using Ni ALD catalysts may be a way of enhancing the activity of these catalysts because 1) ALD catalysts have a higher active surface area per gram, and 2) the ALD catalysts have a higher concentration of step edges (which are more favorable for hydrogenolysis, or hydrodeoxygenation). The increased amount of step edges on these catalysts could enhance the HDO rate, or they could potentially cleave bonds unselectively. Also, since decarbonylation seems to require terrace sites, the small Ni particles likely don't have large enough sites for this reaction to occur, and could potentially favor an upright binding of furfural (which would lead to better selectivity for HDO).

6.2.5 References

[1] X. Liang, B. W Evanko, A. Izar, D. M King, Y.-B. Jiang, A.W. Weimer, Microporous and Mesoporous Materials (2012).
[2] X. Liang, J. Li, M. Yu, C.N. McMurray, J.L. Falconer, A.W. Weimer, ACS Catalysis 1 (2011) 1162-1165.
[3] H. Feng, J. Lu, P. Stair, J. Elam, Catalysis Letters 141 (2011) 512-517.
[4] B. Yoon, D. Seghete, A.S. Cavanagh, S.M. George, Chemistry of Materials 21 (2009) 5365-5374.
[5] M. Heemeier, A.F. Carlsson, M. Naschitzki, M. Schmal, M. Bäumer, H.-J. Freund, Angewandte Chemie International Edition 41 (2002) 4073-4076.
[6] B. Coq, F. Figueras, Journal of Molecular Catalysis A: Chemical 173 (2001) 117-134.
[7] F. Cavani, N. Ballarini, A. Cericola, Catalysis Today 127 (2007) 113-131.
[8] S. Sitthisa, D.E. Resasco, Catalysis Letters 141 (2011) 784-791.
[9] S.H. Pang, C.A. Schoenbaum, D.K. Schwartz, J.W. Medlin, Nature communications 4 (2013).

Chapter 7: Bibliography

1. Natural Gas Reforming. http://www1.eere.energy.gov/hydrogenandfuelcells/production/natural_gas.html (accessed 12-12-13).

2. Current Metal Prices. http://www.icmj.com/current-metal-prices.php (accessed 12-14-13).

3. Aaltonen, T.; Ritala, M.; Sajavaara, T.; Keinonen, J.; Leskela¨, M., Chemistry of Materials 2003, 15 (9), 1924-1928.

4. Aaron Deskins, N.; Mei, D.; Dupuis, M., Surface Science 2009, 603 (17), 2793-2807.

5. Abild-Pedersen, F.; Greeley, J.; Nørskov, J., Catalysis Letters 2005, 105 (1), 9-13.

6. Abild-Pedersen, F.; Nørskov, J. K.; Rostrup-Nielsen, J. R.; Sehested, J.; Helveg, S., Physical Review B 2006, 73 (11), 115419.

7. Aiken Iii, J. D.; Finke, R. G., Journal of Molecular Catalysis A: Chemical 1999, 145 (1-2), 1-44.

8. Alayoglu, S.; Nilekar, A. U.; Mavrikakis, M.; Eichhorn, B., Nat Mater 2008, 7 (4), 333-338.

9. Alfons M. Molenbroek, S. H., Henrik Topsoe, Bjerne S. Clausen, Topics in Catalysis 2009, 52, 1303-1311.

10. Aparicio, L. M., Journal of Catalysis 1997, 165 (2), 262-274.

11. Armor, J. N., Catalysis Today 2011, 163 (1), 3-9.

12. Avetisov, A. K.; Rostrup-Nielsen, J. R.; Kuchaev, V. L.; Bak Hansen, J. H.; Zyskin, A. G.; Shapatina, E. N., Journal of Molecular Catalysis A: Chemical 2010, 315 (2), 155-162.

13. Bachmann, J.; Zolotaryov, A.; Albrecht, O.; Goetze, S.; Berger, A.; Hesse, D.; Novikov, D.; Nielsch, K., Chemical Vapor Deposition 2011, 17 (7-9), 177-180.

14. Baker, R. T. K., Carbon 1989, 27 (3), 315-323.

15. Bartholomew, C. H., Applied Catalysis A: General 1993, 107 (1), 1-57.

16. Bartholomew, C. H., Applied Catalysis A: General 2001, 212 (1-2), 17-60.

17. Bartholomew, C. H.; Pannell, R. B., Journal of Catalysis 1980, 65 (2), 390-401.

18. Baudouin, D.; Rodemerck, U.; Krumeich, F.; Mallmann, A. d.; Szeto, K. C.; Ménardd, H.; Veyre, L.; Candy, J.-P.; Webb, P. B.; Thieuleux, C.; Copéreta, C., Journal of Catalysis 2013, 297 (0), 27-34.

19. Baudouin, D.; Szeto, K. C.; Laurent, P.; De Mallmann, A.; Fenet, B.; Veyre, L.; Rodemerck, U.; Copéret, C.; Thieuleux, C., Journal of the American Chemical Society 2012, 134 (51), 20624-20627.

20. Baumgarten, E.; Wagner, R.; Lentes-Wagner, C., Fresenius' Zeitschrift für analytische Chemie 1989, 334 (3), 246-251.

21. Bell, A. T., Science 2003, 299 (5613), 1688-1691.

22. Bengaard, H.; Nørskov, J. K.; Sehested, J.; Clausen, B. S.; Nielsen, L. P.; Molenbroek, A. M.; Rostrup-Nielsen, J. R., Journal of Catalysis 2002, 209 (2), 365-384.

23. Besenbacher, F.; Chorkendorff, I.; Clausen, B.; Hammer, B.; Molenbroek, A.; Nørskov, J. K.; Stensgaard, I., Science 1998, 279 (5358), 1913-1915.

24. Bjørgen, M.; Joensen, F.; Spangsberg Holm, M.; Olsbye, U.; Lillerud, K.-P.; Svelle, S., Applied Catalysis A: General 2008, 345 (1), 43-50.

25. Bjørgen, M.; Svelle, S.; Joensen, F.; Nerlov, J.; Kolboe, S.; Bonino, F.; Palumbo, L.; Bordiga, S.; Olsbye, U., Journal of Catalysis 2007, 249 (2), 195-207.

26. Blöchl, P. E., Physical Review B 1994, 50 (24), 17953.

27. Blyholder, G., The Journal of Physical Chemistry 1964, 68 (10), 2772-2777.

28. Bond, G. C., Surface Science 1985, 156, Part 2 (0), 966-981.

29. Bond, G. C., Chemical Society Reviews 1991, 20 (4), 441-475.

30. Boudjahem, A. G.; Monteverdi, S.; Mercy, M.; Bettahar, M. M., Journal of Catalysis 2004, 221 (2), 325-334.

31. Bozon-Verduraz, F.; Fiévet, F.; Piquemal, J.-Y.; Brayner, R.; El Kabouss, K.; Soumare, Y.; Viau, G.; Shafeev, G., Brazilian Journal of Physics 2009, 39, 134-140.

32. Briquet, L. G. V.; Catlow, C. R. A.; French, S. A., The Journal of Physical Chemistry C 2010, 114 (50), 22155-22158.

33. Carenco, S.; Boissière, C.; Nicole, L.; Sanchez, C.; Le Floch, P.; Mézailles, N., Chemistry of Materials 22 (4), 1340-1349.

34. Cavani, F.; Ballarini, N.; Cericola, A., Catalysis Today 2007, 127 (1), 113-131.

35. Ceresana Market Study: Propylene (UC-1705). http://www.ceresana.com/en/market-studies/chemicals/propylene/propylene-market-share-capacity-demand-supply-forecast-innovation-application-growth-production-size-industry.html (accessed 12-13-13).

36. Chen, Y.; Zhang, L., Catalysis Letters 1992, 12 (1), 51-62.

37. Chorkendorff, I.; Niemantsverdriet, J. W., Wiley. com: 2006.

38. Christensen, S. T.; Elam, J. W.; Rabuffetti, F. A.; Ma, Q.; Weigand, S. J.; Lee, B.; Seifert, S.; Stair, P. C.; Poeppelmeier, K. R.; Hersam, M. C.; Bedzyk, M. J., Small 2009, 5 (6), 750-757.

39. Christensen, S. T.; Feng, H.; Libera, J. L.; Guo, N.; Miller, J. T.; Stair, P. C.; Elam, J. W., Nano Letters 2010, 10 (8), 3047-3051.

40. Coq, B.; Figueras, F., Journal of Molecular Catalysis A: Chemical 2001, 173 (1-2), 117-134.

41. Corma, A.; Melo, F.; Sauvanaud, L.; Ortega, F., Catalysis Today 2005, 107, 699-706.

42. Corral Valero, M.; Raybaud, P.; Sautet, P., The Journal of Physical Chemistry B 2006, 110 (4), 1759-1767.

43. Coulter, K.; Xu, X.; Goodman, D. W., The Journal of Physical Chemistry 1994, 98 (4), 1245-1249.

44. Dameron, A. A.; Seghete, D.; Burton, B. B.; Davidson, S. D.; Cavanagh, A. S.; Bertrand, J. A.; George, S. M., Chemistry of Materials 2008, 20 (10), 3315-3326.

45. Dartigues, J. M.; Chambellan, A.; Gault, F. G., Journal of the American Chemical Society 1976, 98 (3), 856-857.

46. de Miguel, S. R.; Vilella, I. M. J.; Maina, S. P.; José-Alonso, D. S.; Román-Martínez, M. C.; Illán-Gómez, M. J., Applied Catalysis A: General 2012.

47. Duprez, D.; DeMicheli, M. C.; Marecot, P.; Barbier, J.; Ferretti, O. A.; Ponzi, E. N., Journal of Catalysis 1990, 124 (2), 324-335.

48. Edwards, J. H.; Maitra, A. M., Fuel Processing Technology 1995, 42 (2-3), 269-289.

49. Elam, J.; Routkevitch, D.; Mardilovich, P.; George, S., Chemistry of Materials 2003, 15 (18), 3507-3517.

50. Elliott, S. D.; Greer, J. C., Journal of Materials Chemistry 2004, 14 (21), 3246-3250.

51. Erley, W.; Wagner, H., Surface Science 1978, 74 (2), 333-341.

52. Feng, H.; Libera, J. A.; Stair, P. C.; Miller, J. T.; Elam, J. W., ACS Catalysis 2011, 1 (6), 665-673.

53. Feng, H.; Lu, J.; Stair, P.; Elam, J., Catalysis Letters 2011, 141 (4), 512-517.

54. Foger, K.; Anderson, J. R., Applications of Surface Science 1979, 2 (3), 335-351.

55. Gafner, S.; Redel', L.; Gafner, Y., The Physics of Metals and Metallography 2007, 104 (2), 180-186.

56. Gallezot, P.; Richard, D., Catalysis Reviews 1998, 40 (1-2), 81-126.

57. García-Diéguez, M.; Finocchio, E.; Larrubia, M. Á.; Alemany, L. J.; Busca, G., Journal of Catalysis 2010, 274 (1), 11-20.

58. García-Diéguez, M.; Pieta, I. S.; Herrera, M. C.; Larrubia, M. A.; Alemany, L. J., Applied Catalysis A: General 2010, 377 (1-2), 191-199.

59. Gasser, R. P. H.; Ehrlich, G., Physics Today 1987, 40, 128.

60. George, S. M., Polymer 2012, 1550, 125.

61. Gharibi, M.; Zangeneh, F. T.; Yaripour, F.; Sahebdelfar, S., Applied Catalysis A: General 2012, 443-444 (0), 8-26.

62. Goodman, D. W., Surface Science 1982, 123 (1), L679-L685.

63. Gould, T. D.; Lubers, A. M.; Neltner, B. T.; Carrier, J. V.; Weimer, A. W.; Falconer, J. L.; Will Medlin, J., Journal of Catalysis 2013, 303, 9-15.

64. Gould, T. D.; Montemore, M. M.; Lubers, A. M.; Weimer, A.; Falconer, J. L.; Medlin, J. W., Submitted to Journal of Catalysis 2013.

65. Gracia, F.; Bollmann, L.; Wolf, E.; Miller, J.; Kropf, A., Journal of Catalysis 2003, 220 (2), 382-391.

66. Greeley, J.; Mavrikakis, M., Nature materials 2004, 3 (11), 810-815.

67. Ha, L.; Mao, J.; Zhou, J.; Zhang, Z. C.; Zhang, S., Applied Catalysis A: General 2008, In Press, Accepted Manuscript.

68. Hammaker, R. M.; Francis, S. A.; Eischens, R. P., Spectrochimica Acta 1965, 21 (7), 1295-1309.

69. Hammer, B.; Nørskov, J. K.; Bruce C. Gates, H. K., Theoretical surface science and catalysis - calculations and concepts. In Advances in Catalysis, Academic Press: 2000; Vol. Volume 45, pp 71-129.

70. Hardeveld, R. V.; Hartog, F., Advances in Catalysis 1972, 22, 75-110.

71. Haruta, M., Catalysis Today 1997, 36 (1), 153-166.

72. He, Y.; Li, X.; Swihart, M. T., Chemistry of Materials 2005, 17 (5), 1017-1026.

73. Heemeier, M.; Carlsson, A. F.; Naschitzki, M.; Schmal, M.; Bäumer, M.; Freund, H.-J., Angewandte Chemie International Edition 2002, 41 (21), 4073-4076.

74. Helveg, S.; Sehested, J.; Rostrup-Nielsen, J. R., Catalysis Today 2011, 178 (1), 42-46.

75. Hou, Y.; Gao, S., Journal of Materials Chemistry 2003, 13 (7), 1510-1512.

76. Hu, E. L.; Davis, S. M.; Davis, R.; Scher, E., Applications: Catalysis by Nanostructured Materials: Nanotechnology Research Directions for Societal Needs in 2020. Springer Netherlands: 2011; Vol. 1, pp 445-466.

77. Humbert, M. P.; Chen, J. G., Journal of Catalysis 2008, 257 (2), 297-306.

78. İnoğlu, N.; Kitchin, J. R., Journal of Catalysis 2009, 261 (2), 188-194.

79. Jackson, S. D.; Glanville, B. M.; Willis, J.; McLellan, G. D.; Webb, G.; Moyes, R. B.; Simpson, S.; Wells, P. B.; Whyman, R., Journal of Catalysis 1993, 139 (1), 207-220.

80. Jin, Y.; Asaoka, S.; Li, X.; Asami, K.; Fujimoto, K., Fuel Processing Technology 2004, 85 (8-10), 1151-1164.

81. Jones, C. W.; Zones, S. I.; E. Davis, M., Applied Catalysis A: General 1999, 181 (2), 289-303.

82. Jones, G.; Jakobsen, J. G.; Shim, S. S.; Kleis, J.; Andersson, M. P.; Rossmeisl, J.; Abild-Pedersen, F.; Bligaard, T.; Helveg, S.; Hinnemann, B.; Rostrup-Nielsen, J. R.; Chorkendorff, I.; Sehested, J.; Nørskov, J. K., Journal of Catalysis 2008, 259 (1), 147-160.

83. Kahsar, K. R.; Schwartz, D. K.; Medlin, J. W., Journal of the American Chemical Society 2013.

84. Kappers, M. J.; Maas, J. H., Catalysis Letters 1991, 10 (5-6), 365-373.

85. Kessels, W.; Knoops, H.; Dielissen, S.; Mackus, A.; van de Sanden, M., Applied Physics Letters 2009, 95 (1), 013114-013114-3.

86. King, D. M.; Liang, X.; Weimer, A. W., Powder Technology 2012, 221 (0), 13-25.

87. King, D. M.; Spencer Ii, J. A.; Liang, X.; Hakim, L. F.; Weimer, A. W., Surface and Coatings Technology 2007, 201 (22-23), 9163-9171.

88. Kip, B. J.; Duivenvoorden, F. B. M.; Koningsberger, D. C.; Prins, R., Journal of Catalysis 1987, 105 (1), 26-38.

89. Kondratenko, E. V.; Cherian, M.; Baerns, M., Catalysis Today 2005, 99 (1-2), 59-67.

90. Koningsberger, D.; Prins, R., 1987.

91. Kresse, G.; FurthmÃ¼ller, J. r., Computational Materials Science 1996, 6 (1), 15-50.

92. Kresse, G.; Hafner, J. r., Physical Review B 1993, 47 (1), 558.

93. Kresse, G.; Joubert, D., Physical Review B 1999, 59 (3), 1758.

94. Kristyán, S.; Timmons, R. B., Journal of Catalysis 1986, 101 (2), 331-341.

95. Kroll, V. C. H.; Swaan, H. M.; Mirodatos, C., Journal of Catalysis 1996, 161 (1), 409-422.

96. Kukovitsky, E. F.; L'Vov, S. G.; Sainov, N. A.; Shustov, V. A.; Chernozatonskii, L. A., Chemical Physics Letters 2002, 355 (5-6), 497-503.

97. LaGrow, A. P.; Ingham, B.; Cheong, S.; Williams, G. V. M.; Dotzler, C.; Toney, M. F.; Jefferson, D. A.; Corbos, E. C.; Bishop, P. T.; Cookson, J.; Tilley, R. D., Journal of the American Chemical Society 2011, 134 (2), 855-858.

98. Lamber, R.; Wetjen, S.; Jaeger, N. I., Physical Review B 1995, 51 (16), 10968-10971.

99. Lebedeva, N.; Rodes, A.; Feliu, J.; Koper, M.; Van Santen, R., The Journal of Physical Chemistry B 2002, 106 (38), 9863-9872.

100. Lee, P. I.; Schwarz, J. A.; Heydweiller, J. C., Chemical Engineering Science 1985, 40 (3), 509-519.

101. Lei, Y.; Liu, B.; Lu, J.; Lobo-Lapidus, R. J.; Wu, T.; Feng, H.; Xia, X.; Mane, A. U.; Libera, J. A.; Greeley, J. P.; Miller, J. T.; Elam, J. W., Chemistry of Materials 2012, 24 (18), 3525-3533.

102. Li, D.; Nakagawa, Y.; Tomishige, K., Applied Catalysis A: General 2011, 408 (1-2), 1-24.

103. Li, J.; Liang, X.; King, D. M.; Jiang, Y.-B.; Weimer, A. W., Applied Catalysis B: Environmental 2010, 97 (1-2), 220-226.

104. Li, Y.; Somorjai, G. A., Nano Letters 2010, 10 (7), 2289-2295.

105. Liang, X.; Li, J.; Yu, M.; McMurray, C. N.; Falconer, J. L.; Weimer, A. W., ACS Catalysis 2011, 1 (10), 1162-1165.

106. Liang, X.; Lyon, L.; Jiang, Y.-B.; Weimer, A., Journal of Nanoparticle Research 2012, 14 (6), 1-12.

107. Liang, X.; W Evanko, B.; Izar, A.; M King, D.; Jiang, Y.-B.; Weimer, A. W., Microporous and Mesoporous Materials 2012.

108. Lim, B. S.; Rahtu, A.; Gordon, R. G., Nat Mater 2003, 2 (11), 749-754.

109. Loh, A. S.; Davis, S. W.; Medlin, J. W., Journal of the American Chemical Society 2008, 130 (16), 5507-5514.

110. Lu, H. L.; Scarel, G.; Wiemer, C.; Perego, M.; Spiga, S.; Fanciulli, M.; Pavia, G., Journal of The Electrochemical Society 2008, 155 (10), H807-H811.

111. Lu, J.; Elam, J. W.; Stair, P. C., Accounts of Chemical Research 2013.

112. Lu, J.; Fu, B.; Kung, M. C.; Xiao, G.; Elam, J. W.; Kung, H. H.; Stair, P. C., Science 2012, 335 (6073), 1205-1208.

113. Lu, J.; Stair, P. C., Angewandte Chemie International Edition 2010, 49 (14), 2547-2551.

114. Lundwall, M. J.; McClure, S. M.; Goodman, D. W., The Journal of Physical Chemistry C 2010, 114 (17), 7904-7912.

115. Mackus, A. J. M.; Leick, N.; Baker, L.; Kessels, W. M. M., Chemistry of Materials 2012, 24 (10), 1752-1761.

116. Martin, G. A., Journal of Catalysis 1979, 60 (3), 345-355.

117. Mavrikakis, M.; Hammer, B.; Nørskov, J. K., Physical Review Letters 1998, 81 (13), 2819-2822.

118. Mavrikakis, M.; Stoltze, P.; Nørskov, J. K., Catalysis Letters 2000, 64 (2-4), 101-106.

119. Medasani, B.; Park, Y. H.; Vasiliev, I., Physical Review B 2007, 75 (23), 235436.

120. Miller, K. L.; Lee, C. W.; Falconer, J. L.; Medlin, J. W., Journal of Catalysis 2010, 275 (2), 294-299.

121. Moniz, E. J.; Jacoby, H. D.; Meggs, A.; Armtrong, R.; Cohn, D.; Connors, S.; Deutch, J.; Ejaz, Q.; Hezir, J.; Kaufman, G., The future of natural gas. Cambridge, MA: MIT Press: 2011.

122. Montemore, M. M.; Medlin, J. W., The Journal of Physical Chemistry C 2013, 117 (39), 20078-20088.

123. Moon, D. Y.; Kim, W. S.; Kim, T. S.; Kang, B. W.; Park, J. W.; Yeom, S. J.; Kim, J. H. In Atomic Layer Deposition of Copper Seed Layers from a (hfac)Cu(VTMOS) Precursor, Korean Physical Soc: 2009; pp 1330-1333.

124. Moradi, G. R.; Nazari, M.; Yaripour, F., Fuel Processing Technology 2008, 89 (12), 1287-1296.

125. Mustard, D. G.; Bartholomew, C. H., Journal of Catalysis 1981, 67 (1), 186-206.

126. Neurock, M., Journal of Catalysis 2003, 216 (1-2), 73-88.

127. Nikolla, E.; Holewinski, A.; Schwank, J.; Linic, S., Journal of the American Chemical Society 2006, 128 (35), 11354-11355.

128. Nikolla, E.; Schwank, J.; Linic, S., Journal of the American Chemical Society 2009, 131 (7), 2747-2754.

129. Nørskov, J. K.; Bligaard, T.; Logadottir, A.; Bahn, S.; Hansen, L. B.; Bollinger, M.; Bengaard, H.; Hammer, B.; Sljivancanin, Z.; Mavrikakis, M.; Xu, Y.; Dahl, S.; Jacobsen, C. J. H., Journal of Catalysis 2002, 209 (2), 275-278.

130. Olafsen, A.; Daniel, C.; Schuurman, Y.; Råberg, L.; Olsbye, U.; Mirodatos, C., Catalysis Today 2006, 115 (1), 179-185.

131. Olafsen, A.; Slagtern, Ã.; Dahl, I. M.; Olsbye, U.; Schuurman, Y.; Mirodatos, C., Journal of Catalysis 2005, 229 (1), 163-175.

132. Pang, S. H.; Schoenbaum, C. A.; Schwartz, D. K.; Medlin, J. W., Nature communications 2013, 4.

133. Park, J.; Kang, E.; Son, S. U.; Park, H. M.; Lee, M. K.; Kim, J.; Kim, K. W.; Noh, H. J.; Park, J. H.; Bae, C. J.; Park, J. G.; Hyeon, T., Advanced Materials 2005, 17 (4), 429-434.

134. Park, S. K.; Kanjolia, R.; Anthis, J.; Odedra, R.; Boag, N.; Wielunski, L.; Chabal, Y. J., Chemistry of Materials 2010, 22 (17), 4867-4878.

135. Pawelec, B.; Damyanova, S.; Arishtirova, K.; Fierro, J. L. G.; Petrov, L., Applied Catalysis A: General 2007, 323 (0), 188-201.

136. Pérez, O. L.; Romeu, D.; Yacamán, M. J., Applications of Surface Science 1982, 13 (3-4), 402-413.

137. Peri, J. B.; Hannan, R. B., The Journal of Physical Chemistry 1960, 64 (10), 1526-1530.

138. Pompeo, F.; Nichio, N. N.; Souza, M. M.; Cesar, D. V.; Ferretti, O. A.; Schmal, M., Applied Catalysis A: General 2007, 316 (2), 175-183.

139. Puurunen, R. L., Journal of applied physics 2005, 97 (12), 121301-121301-52.

140. Qi, W.; Wang, M.; Liu, Q., Journal of Materials Science 2005, 40 (9), 2737-2739.

141. Qi, W. H.; Wang, M. P., Journal of Nanoparticle Research 2005, 7 (1), 51-57.

142. Reuter, K.; Scheffler, M., Physical Review B 2001, 65 (3), 035406.

143. Rigney, M. P.; Funkenbusch, E. F.; Carr, P. W., Journal of Chromatography A 1990, 499 (0), 291-304.

144. Rostrupnielsen, J.; Hansen, J. B., Journal of Catalysis 1993, 144 (1), 38-49.

145. Rostrup-Nielsen, J.; Nørskov, J., Topics in Catalysis 2006, 40 (1), 45-48.

146. Rostrup-Nielsen, J.; Nørskov, J., Topics in Catalysis 2006, 40 (1), 45-48.

147. Rostrup-Nielsen, J. R.; Sehested, J.; Nørskov, J. K., Hydrogen and synthesis gas by steam- and C02 reforming. In Advances in Catalysis, Academic Press: 2002; Vol. Volume 47, pp 65-139.

148. Satterfield, C. N., McGraw-Hill New York: 1980; Vol. 416.

149. Schaal, M. T.; Hyman, M. P.; Rangan, M.; Ma, S.; Williams, C. T.; Monnier, J. R.; Medlin, J. W., Surface Science 2009, 603 (4), 690-696.

150. Schaal, M. T.; Pickerell, A. C.; Williams, C. T.; Monnier, J. R., Journal of Catalysis 2008, 254 (1), 131-143.

151. Scheffe, J. R.; Allendorf, M. D.; Coker, E. N.; Jacobs, B. W.; McDaniel, A. H.; Weimer, A. W., Chemistry of Materials 2011, 23 (8), 2030-2038.

152. Scheffe, J. R.; Francés, A.; King, D. M.; Liang, X.; Branch, B. A.; Cavanagh, A. S.; George, S. M.; Weimer, A. W., Thin Solid Films 2009, 517 (6), 1874-1879.

153. Schoenbaum, C. A.; Schwartz, D. K.; Medlin, J. W., Journal of Catalysis 2013, 303 (0), 92-99.

154. Sehested, J., Journal of Catalysis 2003, 217 (2), 417-426.

155. Sehested, J., Catalysis Today 2006, 111 (1), 103-110.

156. Setthapun, W.; Williams, W. D.; Kim, S. M.; Feng, H.; Elam, J. W.; Rabuffetti, F. A.; Poeppelmeier, K. R.; Stair, P. C.; Stach, E. A.; Ribeiro, F. H.; Miller, J. T.; Marshall, C. L., The Journal of Physical Chemistry C 2010, 114 (21), 9758-9771.

157. Sheng, J.; Welzel, U.; Mittemeijer, E. J., Applied Physics Letters 2010, 97 (153109), 1-3.

158. Silberova, B.; Fathi, M.; Holmen, A., Applied Catalysis A: General 2004, 276 (1), 17-28.

159. Sitthisa, S.; Resasco, D. E., Catalysis Letters 2011, 141 (6), 784-791.

160. Skoplyak, O.; Barteau, M. A.; Chen, J. G., The Journal of Physical Chemistry B 2006, 110 (4), 1686-1694.

161. Somorjai, G. A.; Borodko, Y. G., Catalysis Letters 2001, 76 (1-2), 1-5.

162. Somorjai, G. A.; Frei, H.; Park, J. Y., Journal of the American Chemical Society 2009, 131 (46), 16589-16605.

163. Somorjai, G. A.; Li, Y., John Wiley & Sons: 2010.

164. Somorjai, G. A.; York, R. L.; Butcher, D.; Park, J. Y., Physical Chemistry Chemical Physics 2007, 9 (27), 3500-3513.

165. Song, H. J.; Jia, X. H.; Yang, X. F.; Tang, H.; Li, Y.; Su, Y. T., CrystEngComm 2011.

166. Stair, P., Topics in Catalysis 2012, 55 (1-2), 93-98.

167. Studt, F.; Abild-Pedersen, F.; Bligaard, T.; Sørensen, R. Z.; Christensen, C. H.; Nørskov, J. K., Science 2008, 320 (5881), 1320-1322.

168. Sun, D.; Zhao, Y.; Su, H.; Li, W., Chinese Journal of Catalysis 2013, 34 (7), 1434-1442.

169. Suzuki, N.; Yamauchi, Y., Journal of sol-gel science and technology 2010, 53 (2), 428-433.

170. Tanksale, A.; Beltramini, J. N.; Dumesic, J. A.; Lu, G. Q., Journal of Catalysis 2008, 258 (2), 366-377.

171. Ten Eyck, G. A.; Pimanpang, S.; Bakhru, H.; Lu, T. M.; Wang, G. C., Chemical Vapor Deposition 2006, 12 (5), 290-294.

172. Teo, B. K., Springer-Verlag Berlin: 1986; Vol. 9.

173. Tupy, S. A.; Karim, A. M.; Bagia, C.; Deng, W.; Huang, Y.; Vlachos, D. G.; Chen, J. G., ACS Catalysis 2012, 2 (11), 2290-2296.

174. Vajda, S.; Pellin, M. J.; Greeley, J. P.; Marshall, C. L.; Curtiss, L. A.; Ballentine, G. A.; Elam, J. W.; Catillon-Mucherie, S.; Redfern, P. C.; Mehmood, F.; Zapol, P., Nat Mater 2009, 8 (3), 213-216.

175. Van Hardeveld, R.; Van Montfoort, A., Surface Science 1966, 4 (4), 396-430.

176. Van Santen, R. A., Accounts of Chemical Research 2008, 42 (1), 57-66.

177. Vang, R. T.; Honkala, K.; Dahl, S.; Vestergaard, E. K.; Schnadt, J.; Lægsgaard, E.; Clausen, B. S.; Nørskov, J. K.; Besenbacher, F., Surface Science 2006, 600 (1), 66-77.

178. Velasco, A.; Mitsuji, H.; Minami, W.; Lee, J. K.; Komiyama, H.; Kim, H.-j., Journal of Crystal Growth 2008, 310 (16), 3837-3842.

179. Velu, S.; Gangwal, S. K., Solid State Ionics 2006, 177 (7â€“8), 803-811.

180. Wang, H.; Kou, X.; Zhang, L.; Li, J., Materials Research Bulletin 2008, 43 (12), 3529-3536.

181. Wang, S.; Lu, G. Q.; Millar, G. J., Energy & Fuels 1996, 10 (4), 896-904.

182. Watts, J. F.; Wolstenholme, J., An Introduction to Surface Analysis by XPS and AES, by John F. Watts, John Wolstenholme, pp. 224. ISBN 0-470-84713-1. Wiley-VCH, May 2003. 2003, 1.

183. Weitkamp, J., Solid State Ionics 2000, 131 (1), 175-188.

184. Werpy, T.; Petersen, G.; Aden, A.; Bozell, J.; Holladay, J.; White, J.; Manheim, A.; Eliot, D.; Lasure, L.; Jones, S. Top Value-Added Chemicals from Biomass. Volume I: Results of Screening for Potential Candidates from Sugars and Synthesis Gas; Department of Energy: Washington, D.C., 2004.

185. Wolfe, D. W., Basic Books: 2001.

186. Wood, D. A.; Nwaoha, C.; Towler, B. F., Journal of Natural Gas Science and Engineering 2012, 9 (0), 196-208.

187. Xiao, L.; Wang, L., The Journal of Physical Chemistry B 2007, 111 (7), 1657-1663.

188. Xu, J.; Yates Jr, J. T., Surface Science 1995, 327 (3), 193-201.

189. Yoon, B.; Seghete, D.; Cavanagh, A. S.; George, S. M., Chemistry of Materials 2009, 21 (22), 5365-5374.

190. Yu, W.; Porosoff, M. D.; Chen, J. G., Chemical Reviews 2012, 112 (11), 5780-5817.

191. Zafiris, G. S.; Gorte, R. J., Journal of Catalysis 1993, 140 (2), 418-423.

192. Zhou, Y.; King, D. M.; Liang, X.; Li, J.; Weimer, A. W., Applied Catalysis B: Environmental 2010, 101 (1-2), 54-60.

193. Zhou, Y.; Muhich, C. L.; Neltner, B. T.; Weimer, A. W.; Musgrave, C. B., The Journal of Physical Chemistry C 2012, 116 (22), 12114-12123.

194. Zieliński, J., Journal of Molecular Catalysis 1993, 79 (1-3), 187-198.